Spring 5-16-2011

First-Principles and Molecular Dynamics Studies of Ferroelectric Oxides: Designing New Materials for Novel Applications

Tingting Qi
University of Pennsylvania, tqi@sas.upenn.edu

First-Principles and Molecular Dynamics Studies of Ferroelectric Oxides: Designing New Materials for Novel Applications

Abstract
In recent years, there has been an increasing demand for materials that can serve for a variety of technological applications, such as nonvolatile ferroelectric random access memory for computers, SONAR sensor device for military vehicles, dielectric materials for telecommunication, and photovoltaic materials for solar energy conversion. In this thesis, we present computational studies of a special class of complex oxides. Specifically, we studied perovskite ferroelectric materials with the general chemical formula ABO_3, where A and B correspond to different chemical species.

Using computational and theoretical tools, we started our search for novel materials by improving our understanding of how the microscopic chemistry and physics determine the macroscopic properties of materials that have been previously synthesized and characterized. Thus, having validated our computational methods, we used those to predict novel materials with superior properties and further developed some general rules and guidelines for the design of novel materials. Depending on the specific problem at hand, we used either *ab initio* density functional theory (DFT) or classical molecular dynamics (MD) modeling.

First, we employed *ab initio* DFT to investigate the material $Bi(Zn_{1/2}Ti_{1/2})O_3$ (BZT), which is considered to be good analogue of the more commonly used $PbTiO_3$. Although $PbTiO_3$ is ubiquitously used, a lead free ceramics, such as $Bi(Zn_{1/2}Ti_{1/2})O_3$, is desirable due to environmental concerns. Our results confirm the material's superior large cation displacement and tetragonal distortion compared to $PbTiO_3$, but also indicate that the conventional electrostatic model (for determining the most favored cation ordering) should be corrected under special lattice geometric circumstances. As the tetragonal distortion increases, the electrostatic contribution to the total energy decreases, rendering other interaction forces relatively more important in determining the ordering of cations. Inspired by our work on BZT, we continued to develop a guideline for designing ferroelectric materials with similar lattice parameters (high tetragonality). Traditionally, Landau-Ginzburg-Devonshire (LGD) theory has been considered a powerful tool for studying ferroelectrics, which relies on the polarization (P) as the order parameter. However, the lack of LGD parameters limits the utility of LGD theory when applied to novel materials with compositional variation, requiring the development of an alternative design rule. To this end, we began by carefully choosing a group of $PbTiO_3$-derived solid solutions. By extracting the essential geometric information (ionic displacement and strain) as well as the polarization of the solutions, we discovered a very good linear correlation between B-cation displacement squared and strain for all 25 solid solutions, suggesting that the B-cation displacement is a more natural order parameter rather than the polarization of the material. Furthermore, we found that the magnitude of the ionic displacement is mostly affected by both the ion covalency and the ion sizes, allowing us to increase the B-cation displacement by substituting the B-site with either a small-size cation or the small fraction of a large-size cation surrounded by rigid TiO_6 neighbors. The advances we made in this work contribute a significant piece to the big picture of understanding the relationships between different microscopic and macroscopic properties for perovskite ferroelectrics.

Next, we turned our attention to the electronic structures for those highly tetragonal ferroelectric materials that we studied so far only the structural properties. We chose three target materials, namely $Bi(Zn_{1/2}Ti_{1/2})O_3$, $Bi(Zn_{3/4}W_{1/4})O_3$ and $Bi(Zn_{3/4}Mo_{1/4})O_3$. All of these materials have two types of B-cations.

Different local chemistries, including *B*-cation ordering, lattice strain, cation identity and oxygen cage O_6 tilt, affect the electronic band gap structure. We found that the cation ordering effect most profoundly affects electronic band gaps in these materials, which also changes the carrier mobility accordingly. More importantly, we discovered that by reorienting the polarization direction by 90°, the band gap can be altered by as much as 0.6 eV. This result highlights the possibility of using a single chemical composition compound for multi-junction solar energy conversion. By arranging cations differently at different layers, different layers would absorb different frequencies of photons of the solar spectrum.

Finally, we utilized a classical bond-valence model (BVMD) to trace the ferroelectric material's fast dynamics under external perturbations, such as electric field or strain field.

One of our studies is about the polarization switching dynamics of the prototypical perovskite ferroelectric $PbTiO_3$, by coherently controlling the collective structural change. A specially shaped terahertz electric field pulse train is pumped to resonate with a particular IR-active phonon mode. We proved that the atoms in the crystal could move collectively from the initial domain orientation to the opposite one during a very short time period (15 ps), suggesting a new time scale for ultrafast ``read'' and ``write'' speed in computers equipped with ferroelectric non-volatile random access memory.

Also, we employed MD simulations to study the domain wall nucleation dynamics under an external strain field. The 90° domain wall width is observed to be around one or two lattice constants thick, consistent with other DFT studies, high-resolution transmission electron microscopy (HRTEM), and atomic force microscopy (AFM) experiments. A very interesting antisymmetry at the wall was revealed with atomic scale details. Our preliminary data for the domain wall nucleation process shows a good match with Merz's law. Additional 90° domain wall nucleation under strain dynamics studies are currently under investigation.

Degree Type
Dissertation

Degree Name
Doctor of Philosophy (PhD)

Graduate Group
Chemistry

First Advisor
Andrew M. Rappe

Keywords
perovskite, density functional theory, molecular dynamics, piezoelectric, photovoltaic

FIRST-PRINCIPLES AND MOLECULAR DYNAMICS STUDIES OF FERROELECTRIC OXIDES: DESIGNING NEW MATERIALS FOR NOVEL APPLICATIONS

Tingting Qi

A DISSERTATION

in

CHEMISTRY

Presented to the Faculties of the University of Pennsylvania in Partial Fulfillment of the Requirements for the Degree of Doctor of Philosophy

2011

Dissertation Committee

Supervisor of Dissertation
Andrew M. Rappe,
Professor,
Chemistry

Jeffery G. Saven,
Associate Professor,
Chemistry

Ju Li,
Associate Professor,
Materials Science and Engineering

Graduate Group Chairperson
Gary A. Molander,
Professor,
Chemistry

DEDICATION

To my parents Maochun and Yamin,
and my husband Matthias

ACKNOWLEDGMENTS

Six and a half years have been an amazing journey for me, a great many people have contributed selflessly to my academic progress and finally this dissertation. I want to express my gratitude to all that have advised, encouraged and helped me.

I am especially grateful to my advisor, Professor Andrew M. Rappe. He has been running the most challenging and useful quantum mechanics class, and opened the fascinating door of computational chemistry to me. Andrew taught me how to think independently and express ideas wisely. His patience supports me to overcome many research obstacles and accomplish scientific publications. I wish one day I can become an as good lecturer and advisor as Andrew has been to me.

I would like to thank my thesis committee members: Professor Jeffery G. Saven, Professor Michael L. Klein, Professor I-Wei Chen, and professor Ju Li for the high standards, insightful comments and hard questions.

My sincere thanks also go to Dr. Ilya Grinberg, Dr. Joseph W. Bennett, Dr. Young-Han Shin, Dr. Sergey Levchenko, Dr. Alexie M. Kolpak, Dr. Sara E. Mason, Dr. Myung Won Lee and Jacob Colbert for sharing with me their valuable knowledge, collaborating with me and giving me warm encouragement.

I thank many other Rappe group members: Miguel Angel Mndez Polanco, Dr. Hiroyuki Takenaka, Dr. Gaoyang Gou, Dr. Seung-Chul Kim, Steve Young, John Mark Martirez, Dr. Sriraj Srinivasan, Lai Jiang, Doyle Yuan, Matthew Curnan, Shi

Liu and Dr. Sugata Chowdhury for being my friends and collaborators. I cherish all the fun during and off work we had.

Most importantly, none of this would have been possible without my dear parents at home in China, and my dear husband. Thank you for providing me spiritual guidance and support constantly.

ABSTRACT

FIRST-PRINCIPLES AND MOLECULAR DYNAMICS STUDIES OF FERROELECTRIC OXIDES:

DESIGNING NEW MATERIALS FOR NOVEL APPLICATIONS

Tingting Qi

In recent years, there has been an increasing demand for materials that can serve for a variety of technological applications, such as nonvolatile ferroelectric random access memory for computers, SONAR sensor device for military vehicles, dielectric materials for telecommunication, and photovoltaic materials for solar energy conversion. In this thesis, we present computational studies of a special class of complex oxides. Specifically, we studied perovskite ferroelectric materials with the general chemical formula ABO_3, where A and B correspond to different chemical species.

Using computational and theoretical tools, we started our search for novel materials by improving our understanding of how the microscopic chemistry and physics determine the macroscopic properties of materials that have been previously synthesized and characterized. Thus, having validated our computational methods, we used those to predict novel materials with superior properties and further developed some general rules and guidelines for the design of novel materials. Depending on the specific problem at hand, we used either *ab initio* density functional theory (DFT) or classical molecular dynamics (MD) modeling.

First, we employed *ab initio* DFT to investigate the material $Bi(Zn_{1/2}Ti_{1/2})O_3$ (BZT), which is considered to be good analogue of the more commonly used $PbTiO_3$. Although $PbTiO_3$ is ubiquitously used, a lead free ceramics, such as $Bi(Zn_{1/2}Ti_{1/2})O_3$, is desirable due to environmental concerns. Our results confirm the material's superior large cation displacement and tetragonal distortion compared to $PbTiO_3$, but also indicate that the conventional electrostatic model (for determining the most favored cation ordering) should be corrected under special lattice geometric circumstances. As the tetragonal distortion increases, the electrostatic contribution to the total energy decreases, rendering other interaction forces relatively more important in determining the ordering of cations. Inspired by our work on BZT, we continued to develop a guideline for designing ferroelectric materials with similar lattice parameters (high tetragonality). Traditionally, Landau-Ginzburg-Devonshire (LGD) theory has been considered a powerful tool for studying ferroelectrics, which relies on the polarization (P) as the order parameter. However, the lack of LGD parameters limits the utility of LGD theory when applied to novel materials with compositional variation, requiring the development of an alternative design rule. To this end, we began by carefully choosing a group of $PbTiO_3$-derived solid solutions. By extracting the essential geometric information (ionic displacement and strain) as well as the polarization of the solutions, we discovered a very good linear correlation between B-cation displacement squared and strain for all 25 solid solutions, suggesting that

the B-cation displacement is a more natural order parameter rather than the polarization of the material. Furthermore, we found that the magnitude of the ionic displacement is mostly affected by both the ion covalency and the ion sizes, allowing us to increase the B-cation displacement by substituting the B-site with either a small-size cation or the small fraction of a large-size cation surrounded by rigid TiO_6 neighbors. The advances we made in this work contribute a significant piece to the big picture of understanding the relationships between different microscopic and macroscopic properties for perovskite ferroelectrics.

Next, we turned our attention to the electronic structures for those highly tetragonal ferroelectric materials that we studied so far only the structural properties. We chose three target materials, namely $Bi(Zn_{1/2}Ti_{1/2})O_3$, $Bi(Zn_{3/4}W_{1/4})O_3$ and $Bi(Zn_{3/4}Mo_{1/4})O_3$. All of these materials have two types of B-cations. Different local chemistries, including B-cation ordering, lattice strain, cation identity and oxygen cage O_6 tilt, affect the electronic band gap structure. We found that the cation ordering effect most profoundly affects electronic band gaps in these materials, which also changes the carrier mobility accordingly. More importantly, we discovered that by reorienting the polarization direction by 90°, the band gap can be altered by as much as 0.6 eV. This result highlights the possibility of using a single chemical composition compound for multi-junction solar energy conversion. By arranging cations differently at different layers, different layers would absorb different frequencies of

photons of the solar spectrum.

Finally, we utilized a classical bond-valence model (BVMD) to trace the ferroelectric material's fast dynamics under external perturbations, such as electric field or strain field.

One of our studies is about the polarization switching dynamics of the prototypical perovskite ferroelectric $PbTiO_3$, by coherently controlling the collective structural change. A specially shaped terahertz electric field pulse train is pumped to resonate with a particular IR-active phonon mode. We proved that the atoms in the crystal could move collectively from the initial domain orientation to the opposite one during a very short time period (15 ps), suggesting a new time scale for ultrafast "read" and "write" speed in computers equipped with ferroelectric non-volatile random access memory.

Also, we employed MD simulations to study the domain wall nucleation dynamics under an external strain field. The 90° domain wall width is observed to be around one or two lattice constants thick, consistent with other DFT studies, high-resolution transmission electron microscopy (HRTEM), and atomic force microscopy (AFM) experiments. A very interesting antisymmetry at the wall was revealed with atomic scale details. Our preliminary data for the domain wall nucleation process shows a good match with Merz's law. Additional 90° domain wall nucleation under strain dynamics studies are currently under investigation.

Contents

List of Tables

List of Figures

Chapter 1

Introduction

1.1 Materials Science

Due to the rapid scientific and technological development in the last century, the rational design of materials has become possible. That is, rather than improving existing or developing novel materials by trial and error, the properties of a novel material can be fine-tuned for a particular application by taking advantage of the understanding how its microscopic properties affect its macroscopic ones. Our current microscopic understanding of materials is based on the tremendous scientific knowledge, which has been accumulated in various areas, such as solid-state physics, inorganic chemistry, organic chemistry and physical chemistry. Besides its scientific component, materials science presents also challenges to engineering, such as the synthesis of materials and their characterization.

This thesis focuses on the scientific part of materials science, by investigating and characterizing fundamental properties of materials. Specifically, computational tools are employed, providing insights into the microscopic structure of the materials of interest and their response to external perturbations at a level of detail that is not possible to achieve experimentally. Thus, computer simulations of materials further our understanding of how certain material structures give rise to certain properties, enabling the design of new materials with the desired properties. For example, recent collaborative work between the research groups of Rappe and Bonnell on barium titanate (001) surface reconstruction not only confirmed the experimental

findings of several surface reconstruction patterns, but also suggested surface reconstruction patterns that are not easily accessible via experiment, enabling prediction of surface structures and properties under entire range of accessible environmental conditions [74].

The materials that we will discuss in this thesis are one group of ceramic oxides, namely perovskite materials (formula ABO_3). The perovskite oxides are a class of materials of fundamental scientific interest as well as varied technological applications [11, 106, 16], since they display a variety of properties including piezoelectricity, pyroelectricity, ferroelectricity, and many others. There is a strong demand for perovskite oxides with higher performance and better functionality for use in many different types of devices.

1.2 Perovskite Ferroelectrics

The name "perovskite" is used to refer to materials that share a similar lattice structure with $CaTiO_3$, which is the first perovskite mineral that was discovered. In 1945, the first perovskite crystal structure of the common perovskite barium titanate ($BaTiO_3$) was determined by Helen Dick McGaw via X-ray diffraction [85]. Perovskites can adopt various crystal structures of different symmetry, the simplest of which exhibits cubic symmetry. It consists of 12-coordinated A cations on the corners of a cube unit cell, oxygen anions on the faces, and B cations in the center Fig. 1.1. It

is important to note that most perovskite structures do not have such high symmetry as the cubic case. Usually, the cation displacements away from oxygen cage center and the O_6 octahedra rotations occur. Such deviation of the perovskite structures from cubic symmetry relates to the properties of the A and B substituted atoms. Factors that contribute to distortion include mainly the radius size effect [101] and the Jahn-Teller effect [31]. The breaking of cubic symmetry, as explained later, is crucial to polarization.

Figure 1.1: The perovskite (ABO_3) lattice structure is shown, where grey, blue and red represent A, B and O atoms.

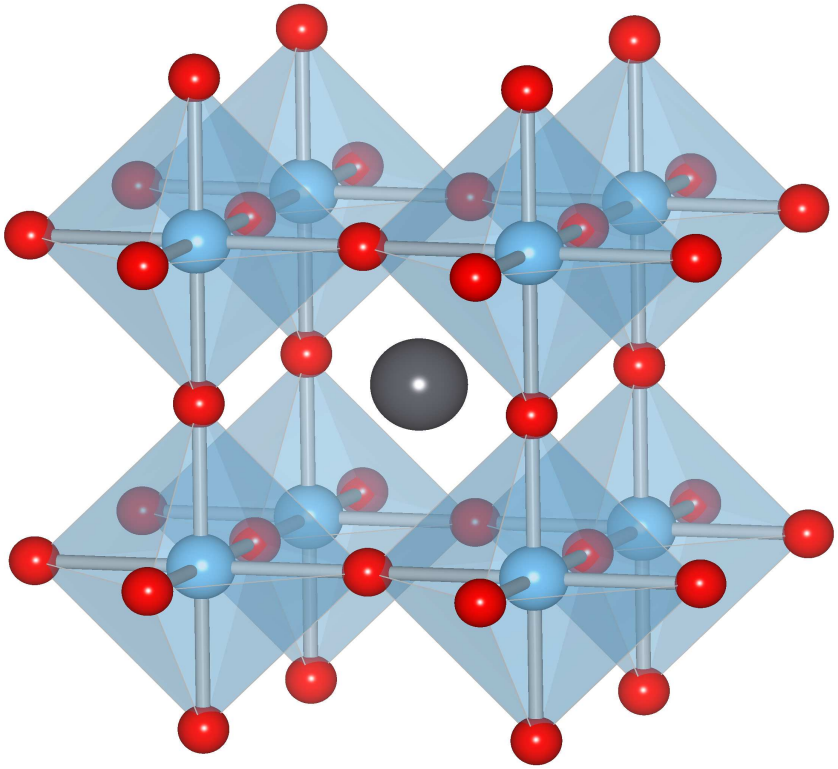

In perovskite ABO_3, the A site is usually occupied by a rare earth or alkali-earth metal cation, while the B site is usually occupied by a transition metal cation. Sometimes, the A-site and the B-site can each be occupied by two or more than two chemical species. Depending upon the choice of A- and B-site atoms, the perovskites structures and properties can vary dramatically. In rare occasions, even the oxygen anions in ABO_3 can be substituted by other types of anions, such as the sulfur anion S^{-2} [13].

Ferroelectric oxides are a subgroup of perovskite oxides that possess a permanent electric dipole, and were named in analogy to the ferromagnetic material (e.g. Fe) that has a permanent magnetic dipole. At low temperature, a spontaneous polarization exists, which can be reversed by an applied external electric field. The relation between polarization and electric field obeys a hysteresis loop with significant nonlinearities. The polarization is prohibited in the presence of centrosymmetry. Otherwise, the crystal would be polar. When the temperature is raised above the Curie temperature (T_c), a phase transition (from the ferroelectric phase to the paraelectric phase) occurs accompanied by a sudden disappearance of the spontaneous polarization. The ferroelectric phase transition can often be characterized as displacive (barium titanate), order-disorder, or both (lead titanate) [111].

1.3 Empirical Models

Although, the quantitative determination of the physical properties of perovskites is a difficult undertaking, some simple, but powerful empirical models were developed that can help us gain important physical insights without the need of elaborate experiments or computations. These models are the tolerance factor argument [45], Brown's rule [22] and the Landau theory of phase transition [33].

We are going to discuss the tolerance factor argument first. Goldschmidt was the first one to examine the octahedral tilting distortions that are present in many perovskites. He found that the degree of distortion in ABO_3 perovskites can be generally determined using the following equation:

$$t = \frac{R_{\mathrm{A-O}}}{R_{\mathrm{B-O}}\sqrt{2}} \tag{1.1}$$

where t is the tolerance factor, $R_{\mathrm{A-O}}$ is the sum of A and O ionic radii and $R_{\mathrm{B-O}}$ is the sum of B and O ionic radii. A t value for stable perovskite structures is approximately between 0.78 and 1.05. If $t < 1$, it usually leads to the rotation or expansion of the B-O_6 octahedra. Such octahedral rotations often generate a low-temperature antiferroelectric phase (e. g. $PbZrO_3$). If $t > 1$, the B-O_6 octahedra are stretched from their preferred B-O bond lengths, promoting B-cation distortions by creating space for the B-cations to move off-center. Therefore, simple perovskites with $t > 1$ are usually ferroelectric.

We can use this tolerance factor argument to obtain a general idea about the

preferred ground state of an unknown perovskite material. The relationship between the sizes of the A-O and the B-O_2 sublattices contributes to the material properties. However, we need to keep in mind that it is only a rough estimate. The tolerance factor provides exceptions. Careful calculations still need to be performed to determine the fine features of the lattice geometry [6].

In the following, we are discussing Brown's rule, which states that the bond length is well correlated to the bond valence through an inverse power relation. The powerful description in terms of traditional chemical concepts of atoms and bonds provides insights and inherent simplicity. Knowledge of such correlation allows experimental bond valences to be calculated from observed bond lengths. Unfortunately, determining this correlation is not an easy task, because the expected bond valence can only be reliably predicted in a limited number of cases. A fitting procedure is usually carried out to obtain the correlation. Typically, a simple two parameter algebraic equation is sufficient to relate bond valence and bond length.

$$V = (R/R_0)^{-N} \tag{1.2}$$

or

$$V = e^{(R_0 - R)/b} \tag{1.3}$$

where V is the calculated bond valence, R the observed bond length, R_0, b or N are fitted bond valence parameters. R_0 can be thought of as the nominal length of a bond

of unit valence, depending on the sizes of the atoms (that participating in forming the bond). N or b represents the bond stiffness. In this thesis, we chose $V = (R/R_0)^{-N}$ for treating A-O and B-O chemical bonding within the perovskite structure, and the total atomic valence of each atom equal to the sum of its bond valences. In our bond-valence (BV) molecular dynamics model, the constituent energy terms are defined as following for $PbTiO_3$:

$$E_b = \sum_{\beta=1}^{3} S_\beta \sum_{i=1}^{N_\beta} |V_{i\beta} - V_\beta|^{\alpha_\beta} \tag{1.4}$$

$$V_{i\beta} = \sum_{\beta'=1}^{3} \sum_{i'(NN)} \left(\frac{r_0^{\beta\beta'}}{r_{ii'}^{\beta\beta'}} \right)^{C_{\beta\beta'}} \tag{1.5}$$

where E_b is the bond-valence contribution to the potential energy. $V_{i\beta}$ is the bond valence of the ith atom of type β, calculated according to Brown's formulation. β is the index for Pb, Ti and O ions, NN means the nearest-neighbor atoms, and N_β is the number of the β ions. V_β is the desired atomic valence of the β ion, and $r_{ii'}^{\beta\beta'}$ is the distance between the ith β ion and the i'th β'ion. Our group developed a robust BV model parameter set for $PbTiO_3$ by fitting the model containing unknown parameters to a database containing structures calculated from first-principles calculations (the details of which will be discussed in a later chapter). With the BV model, we are able to run MD simulations for systems of sizes far beyond the scope of the DFT method.

The last empirical model discussed here is the Landau theory. The original work of Landau was developed to describe a second order phase transition. The key in Landau

theory is an order parameter whose non-zero value indicates the ferroelectric phase, while the order parameter remains zero in the high temperature phase (paraelectric phase). In 1949, Devonshire independently derived a phenomenological theory that has the same nature as the Landau theory and successfully describes ferroelectric phase transitions and the temperature dependence of dielectric properties for barium titanate [33]. Moreover, Devonshire generalized Landau's approach to first order transitions as well. Since then, Landau-Ginzburg-Devonshire (LGD) theory has been applied widely for studying ferroelectric materials, especially in the aspects of phase transition and domain pattern formation [139, 27, 57].

In LGD theory, the free energy G is expanded as a power series, depending on temperature T and on an order parameter (usually polarization P). We can specify a thermodynamic equilibrium state for any ferroelectric crystal by using several variables, such as temperature T, electric field E, polarization P, stress σ and strain s.

$$G = \frac{1}{2}\alpha(T - T_0)P^2 + \frac{1}{4}\beta P^4 + \frac{1}{6}\gamma P^6 + ... \tag{1.6}$$

The above is a simple case when polarization is along one of the lattice axis, in the absence of an electric field and stress field. The unknown coefficients (α, γ and β) can be fit to experiments, and are generally temperature dependent. Commonly, a sixth order of Taylor expansion provides a good estimate for G. However, depending on the questions asked, higher order expansions could be necessary.

The free energy G is a double well potential with two energy minima at $P = +P_s$ and $P = -P_s$, where the derivative of G with respect to polarization P is zero. The signs of the LGD coefficients α, β and γ determine the type of phase transition (first order or second order). In most cases, perovskite ferroelectric materials show first order phase transitions (discontinuous phase transition), where the order parameter P drops suddenly at T_c to zero. We can also determine the type of phase transition by reading the plot of dielectric susceptibility with temperature, as the two types of phase transition have distinctly different features. Under the influence of an electric field or stress field, additional terms $-PE$ and $\frac{1}{2}Ks^2 - \sigma s$ need to be taken into account respectively, in the total free energy G expression.

1.4 Ferroelectric Domains

A domain is defined as a collection of unit cells that share the same or a similar polarization direction. A domain pattern in a bulk ferroelectric material, which contains more than one domain, is inevitable. A ferroelectric domain pattern can be caused or influenced by strain, defects, depolarization field and thermal history. Even in an ideal crystal, domains are expected because of the energetic preference: minimizing the energy by abolishing the surface charges, domains are introduced so that the polarization is oriented parallel to the surface. For example, in lead titanate, the two neighboring domains could be either antiparallel to each other, or bisects the 90°

angle between two domain walls pointing head to tail. Compared with 90° domain wall, 180° domain wall is more widely studied. Understanding the microscopic picture of domain is crucial for better engineering macroscopic piezoelectric, dielectric, and pyroelectric properties.

The formation of domain walls involves several key energetic contributions: the elastic energy of the material, the temperature, the location of the domain relative to the sample boundary (edge), the polarization switching energy barrier, electrostatic interactions and many more [5]. Therefore, the domain formation is a complex problem.

In Chapter 4, we performed first-principles calculations to study the extremely tetragonal ferroelectric material $Bi(Zn_{1/2}Ti_{1/2})O_3$ (BZT) [100]. In agreement with experiment, we find that BZT displays extremely large cation displacements and tetragonality. Despite its high tetragonality and polarization, the local structure of the material exhibits a high degree of local disorder that is more typical of solid solutions close to the morphotropic phase boundary. For the tetragonal phase of BZT, we show that a planar ordered (010) B-cation arrangement with the Zn and Ti stacking direction perpendicular to direction of P is the lowest in energy, in contrast with the (111) B-cation ordering usually found in perovskites. We attribute this unusual preference to the large cation displacements found in BZT, which raises the importance of A-B cation repulsive interactions, favoring separation of Zn and Ti

cations.

In Chapter 5, we continued using first-principles calculations investigating the dependence of tetragonality on local structure in a variety of ferroelectric solid solutions [101]. We demonstrate that tetragonality is strongly coupled to the B-cation displacement and weakly coupled to the A-cation displacement. Examination of various BiM^{3+}O$_3$ additives to PbTiO$_3$ for different M^{3+} ionic sizes reveals that substitution of either small B-cations or low doping of large B-cations gives rise to large spontaneous polarization and tetragonality. Understanding how the phase transition temperature (T_c) and tetragonality are affected by Pb-based and Bi-based perovskite additives provides a rational path for designing new high-temperature piezoelectric materials.

In Chapter 6, we examine band structure engineering in extremely tetragonal ferroelectric perovskites (ABO$_3$) to make these materials suitable for photovoltaic applications. Using first-principles generalized-gradient approximation (gga) and local-density approximation+U calculations, we study how B-site ordering, lattice strain, cation identity, and oxygen octahedral cage tilts affect the energies and the compositions of the valence and conduction bands. We find that extreme tetragonality makes the band gap highly sensitive to the B-cation arrangement, with a specially layered B-site arrangement exhibiting a small band gap. It also leads to a strong sensitivity of the band gap to the oxygen octahedral tilting. These effects only occur for cations

with filled d states located near the valence band maximum or empty d states at the conduction band minimum; this criterion is explained by crystal field theory. In addition to a smaller band gap, the layered B-site arrangement has a strong impact on the carrier mobility. We find that excited electron effective mass is similar to that found in Si and other classic semiconductors, an order of magnitude smaller than what is usually found in perovskites. Moreover, the hole effective mass is strongly anisotropic, indicating a 2D hole gas in the layered B-cation arrangement.

In Chapter 7, we show that properly shaped terahertz fields, resonant with selected lattice vibrational frequencies, could be used to move ions in ferroelectric crystals from their positions in an initial domain orientation along well defined collective microscopic paths into the positions they occupy in a new domain orientation [102]. Collective coherent control will enable direct observation of fast highly nonlinear material responses and far-from-equilibrium structures that can be harnessed in electro-optic devices and non-volatile computer memory.

Finally, in Chapter 8, we investigated the atomistic structure of the 90° domain boundaries in the bulk ferroelectric perovskite compound $PbTiO_3$ using a first-principles based classical potential model. Strain induced domain wall dynamics has been studied in detail focusing on the nucleation-forming step. We found 90° domain wall width asymmetric and very narrow with an order of several lattice constants. The domain nucleation follows the Merz's law.

Chapter 2

Theory and Methodology—Density Functional Theory

2.1 Introduction

Inspired by a number of very interesting observations and experiments (the discovery of cathode rays by Michael Faraday in 1838, the statement of the black body radiation problem by Gustav Kirchhoff in 1859, and the suggestions of the discrete energy states by Ludwig Boltzmann in 1877), it was realized that classical physics exhibits certain limitations in explaining the physical world. Building on the revolutionary discoveries and theories of quantum mechanics, the first theoretical calculations in chemistry were those of Walter Heitler and Fritz London in 1927. In the following, we present a brief introduction on the concepts of quantum chemistry.

For a single particle moving in the presence of a potential the time-independent Schrödinger equation can be written as:

$$\left[-\frac{1}{2}\nabla^2 + V(\vec{r})\right]\psi(\vec{r}) = E\psi(\vec{r}) \tag{2.1}$$

The first term in the equation represents the kinetic energy of the particle while the second term represents the potential energy of the particle as a function of position. Materials of interest, such as molecules and solids, consist of numerous electrons and nuclei interacting with each other. In this case, each particle moves in a potential field generated by the other particles. For a system of N electrons and K nuclei with

charges, Z_k the Hamiltonian of the system can be written as follows:

$$H = -\sum_{i=1}^{N} \frac{1}{2}\nabla_i^2 + -\sum_{k=1}^{K} \frac{1}{2M_k}\nabla_k^2 + \frac{1}{2}\sum_{i,j=1,i\neq j}^{N} \frac{1}{|\vec{r}_i - \vec{r}_j|} + \frac{1}{2}\sum_{k,k'=1,k\neq k'}^{K} \frac{Z_k Z_{k'}}{|\vec{R}_k - \vec{R}_{k'}|} - \sum_{i=1}^{N}\sum_{k=1}^{K} \frac{Z_k}{|\vec{r}_i - \vec{R}_k|} \tag{2.2}$$

The first two terms in the Hamiltonian account for the kinetic energy of the electrons and the nuclei, respectively. The third and fourth terms carry the electron-electron and nucleus-nucleus Coulomb repulsions, while the final term represents an electron-nucleus attractive potential. For a many-body system the wave function is dependent on the positions of both the electrons and the nuclei.

2.2 The Born-Oppenheimer Approximation

As we can see from above, it is a formidable task to compute the energies and the wave functions for systems that are more complicated than a hydrogen atom, since those systems contain two or more nuclei and electrons. In order to accurately calculate the system, we will need to consider the nucleus-electron interaction, nucleus-nucleus interaction, electron-electron interaction and the coupling between all these interactions. In some special cases for hyperfine details, even spin-spin coupling between nuclear spin and electron spin should be necessary to be included. The Hamiltonian becomes very complicated for us to study explicitly. Therefore, it is desirable to wisely simplify the total Hamiltonian. One of the most important simplifications is Born-Oppenheimer (BO) approximation [18].

It is well known that the static electron mass is much smaller than nucleus mass by three order of magnitude. As a result, the electron moves much more rapidly than the nucleus does. The Born-Oppenheimer approximation assumes that: at any instant in time, the nuclei are located at some relative positions, and the electronic states for the electrons are the same as those in the case when the nuclei have remained at the same relative locations at all time. Alternatively, we can draw the equivalent of this approximation: the nuclei and the electrons move independently from each other. The electronic wave functions depend only upon the nuclei's relative positions, but not upon nuclei's velocities. The nuclei *see* a smeared-out potential from all the speedy electrons. The BO Hamiltonian can be written as:

$$H_{\mathrm{BO}} = -\sum_{i=1}^{N} \frac{1}{2}\nabla_i^2 + \frac{1}{2}\sum_{i,j=1;i\neq j}^{N} \frac{1}{|\vec{r}_i - \vec{r}_j|} + \sum_{i=1}^{N}\sum_{k=1}^{K} \frac{Z_k}{|\vec{r}_i - \vec{R}_k|}, \tag{2.3}$$

For instance, if we apply this BO approximation for a molecular system, we would then be able to separate translational, rotational and vibrational motions of the nuclei from the electronic states. The interaction between nuclei and electrons can be treated as a perturbation on motions of nuclei, if necessary. Thus, the total wave function of the system can be simply approximated as the product of the nuclear state wave function and the electronic state wave function.

2.3 The Hartree-Fock equations and the Self-consistent Field Approximation

When more than one electron present, even after employing BO approximation, it is still almost impossible to solve the Schrödinger equation analytically because of the complication of the Hamiltonian that we discussed earlier. In order to seek approximate solutions to the electronic Schrödinger equation, we can further simplify the equation to a set of one-electron equations (Hartree equations), with a potential for one electron approximated by an average electronic interactions.

For a system with N-electrons, if the single-particle wave function of ith electron is $\psi_i(\vec{r}_i)$, its electron charge distribution would be $-|\psi_i(\vec{r}_i)|^2$. The electrostatic potential generated by ith electron at $\vec{r}_j$ (jth electron location) is:

$$V^i(\vec{r}_j) = -\int \frac{1}{r_{ij}} |\psi_i(\vec{r}_i)|^2 d\tau_i \tag{2.4}$$

$$r_{ij} = |\vec{r}_i - \vec{r}_j| \tag{2.5}$$

The total electrostatic potential generated by all electrons besides jth electron itself at $\vec{r}_j$ is:

$$V(\vec{r}_j) = -\sum_{i \neq j}^{N} \int \frac{1}{r_{ij}} |\psi_i(\vec{r}_i)|^2 d\tau_i \tag{2.6}$$

Therefore, the overall potentail for jth electron at any location $\vec{r}$ is:

$$V_j(\vec{r}) = -\frac{Z}{r} + \sum_{i \neq j}^{N} \int \frac{1}{|\vec{r}_i - \vec{r}|} |\psi_i(\vec{r}_i)|^2 d\tau_i \tag{2.7}$$

The Hamiltonian is:

$$\vec{H}_j = -\frac{1}{2}\nabla^2 - \frac{Z}{r} + \sum_{i\neq j}^{N} \int \frac{1}{|\vec{r}_i - \vec{r}|}|\psi_i(\vec{r}_i)|^2 d\tau_i \tag{2.8}$$

Finally, the Schrödinger equation is:

$$\vec{H}_j \psi_j(\vec{r}) = \epsilon_j \psi_j(\vec{r}) \tag{2.9}$$

where j=1,2,...,N. These equations are called Hartree equations, where ψ_j is the single-particle wave function for jth electron. In order to solve the Schrödinger equation, Hartree approximated the potentail to be local, which means that $V_j(\vec{r})$ is only a function of $\vec{r}$. Then the solution to the equation would have the form like:

$$\psi_j(\vec{r}_j) = R_{n_j l_j}(r_j) Y_{l_j m_{l_j}}(\theta_{j,j}) \tag{2.10}$$

If the one-electron wave functions are known, the total electronic charge density distribution is also known. By deducing backwards, we can compute the average potential for each electron, and solve for the one-electron wave functions. As the one-electron wave function and its average potential determine each other, the answers have to be self-consistent. We call the average potential that meets the above criterion a self-consistent field (SCF). The Hartree equations are approximately solved by means of iterative algorithm, and the solution is usually one of the many possible solutions. Hartree was the first one to propose this idea.

Clearly, the wave function form $R_{n_j l_j}(r_j) Y_{l_j m_{l_j}}(\theta_{j,j})$ does not subject to the Pauli exclusion principle. In terms of fermions (in our case, electrons), the total wave

function must be antisymmetric upon electron exchange. Slater and Fock introduced Slater determinant as the total wave function form into Hartree equations. This type of Hartree equations are called Hartree-Fock equations. The Slater determinant was specially designed, so that each element contained in the determinant is a single-electron spin-orbital wave function. For the next step, the total energy can be derived iteratively by inserting the Slater determinant into Hartree-Fock equation, via the variational principle. Compared with other trial wave function forms, the Slater determinant always gives lower total energy for solving Hartree-Fock equations.

2.4 Correlation Energy

The Hartree-Fock SCF approximation assumes that the electron moves independently within an average potential, neglecting any momentary correlation within an electron pair. Any two non-interacting electrons with antiparallel spins would be allowed to appear at the same position at the same time based on the previous approximation. But obviously, due to the Coulomb repulsion between electrons, this is impossible. The approximation that assumes electrons move independently, has to be modified. When an electron is at a certain position in space, its close neighboring space around this point forbids or lowers the probabilities for other electrons to enter because of the Coulomb interaction. Such neighboring space is also called *Coulomb hole* and such type of interaction is known as electron correlation, which directly affects the average

potential.

In Hartree-Fock equations with the Slater determinant, because of the inclusion of Pauli exclusion principle, the two electrons with parallel spin are not allowed to appear at the same position at the same time. Thus, it correctly describes the so-called *Fermi hole* around the electrons. The difference between the real energy of a many-body electronic system and the energy calculated from the Hartree-Fock approximation comes from the failure of properly treating antiparallel-spin electrons. We call this the *correlation energy*. Unfortunately, it remains extremely difficult to accurately count for the correlation energy for a complex system.

2.5 Density Functional Theory and Kohn-Sham Equation

In 1927, shortly after the introduction of Schrödinger equation, the Thomas-Fermi (TF) model was developed independently by Thomas and Fermi. This model was the first attempt to describe a many-electron system on the basis of electron charge density instead of wave functions. In spite of the TF model's poor quantitative predictions, it is still viewed as a grand precursor to modern density functional theory (DFT). DFT was developed by Hohenberg and Kohn [59, 73], resolving the many-electron problem by assuming a universal functional of the electron density. The many-electron Schrödinger equation is replaced by the problem of finding sufficiently accurate approximations to the change density and then solving appropriate

single-electron equations (here, we call these Kohn-Sham equations). Unlike the wave function, which becomes significantly more complicated as the number of electrons increases, the determination of the electron density is fairly independent of the total number of electrons. The minimum value of the total-energy functional is the ground-state electron charge density. The Kohn-Sham total-energy functional for a set of doubly occupied electronic states can be written as:

$$\left[-\frac{1}{2}\nabla^2 + V_{\text{ext}}(\vec{r}) + V_{\text{H}}[\rho](\vec{r}) + V_{\text{xc}}(\vec{r})\right]\psi_i(\vec{r}) = \varepsilon_i\psi_i(\vec{r}). \tag{2.11}$$

Here ε_i is the Kohn-Sham eigenenergy of the state $\psi_i(\vec{r})$ and the terms $V_{\text{H}}[\rho](\vec{r})$ and $V_{\text{xc}}[\rho](\vec{r})$ are defined as:

$$V_{\text{H}}[\rho](\vec{r}) = \frac{\delta E_{\text{H}}[\rho]}{\delta\rho(\vec{r}\,')} = \int \frac{\rho(\vec{r})}{|\vec{r}\,' - \vec{r}|} d^3\vec{r}\,' \tag{2.12}$$

$$V_{\text{xc}}[\rho](r) = \frac{\delta E_{\text{xc}}[\rho]}{\delta\rho(\vec{r})} \tag{2.13}$$

The antisymmetry of the wave function produces a spatial separation between parallel-spin electrons and thus reduces the Coulomb energy of the electronic system by representing orbitals by using the Slater determinant. The reduction in the energy of the electronic system due to the antisymmetry of the wave function is called *exchange energy*. DFT would have been of very little interest if there had not been a simple and very practical approximation for the electron exchange-correlation energy. One approximation that is widely used is the local density approximation (LDA) [93, 25]. LDA assumes that the exchange correlation energy is only a function

of electron density, which yields surprisingly accurate results despite of the crude approximation.

$$E_{\mathrm{xc}}[\rho] = \int \varepsilon_{\mathrm{xc}}[\rho](\vec{r})\rho(\vec{r})d^3\vec{r}. \tag{2.14}$$

$$E_{\mathrm{xc}}^{\mathrm{LDA}}[\rho] = \int \varepsilon_{\mathrm{xc}}^{\mathrm{LDA}}(\rho(\vec{r}))\rho(\vec{r})d^3\vec{r}. \tag{2.15}$$

where $\epsilon_{xc}(n)$ is known as exchange-correlation energy per particle of a uniform electron gas of density n. With the single input of $\epsilon_{xc}(n)$, a function of one variable, the ground state energies and density distributions $\rho(\vec{r})$, of any system can be easily calculated in the LDA with accuracy levels, which depends on the system and on the question asked. There are also other approximations for exchange-correlation energy, such as Generalized Gradient Approximations (GGA), where the gradient of the non-uniformity of the electron density is accounted as extra [94, 95, 96].

2.6 Plane Wave Basis Sets

The choice of the basis sets is very important for the SCF iteration. If the basis set is not appropriate, the poorly represented wave functions would lead to the inaccurate results and increasingly large computational effort. Although, theoretically any complete basis set of mathematical functions can be applied to express any wave function, we usually want as few basis set functions as possible. In fact, the requirement of using fewer basis set functions and the requirement of achieving more accurate results often cannot be satisfied simultaneously. It is up to us to choose a compromise

between the two.

The earliest basis set is called LCAO (linear combination of atomic orbitals)-MO (molecular orbital). Nowadays, the more commonly used basis sets are the Slater basis sets, the Gauss basis sets, and the plane-wave basis sets. For systems with periodic boundary condition (as in this thesis), it is more advantageous to apply the plain-wave basis sets, as opposed to others.

$$f_{\vec{G}}(\vec{r}) = e^{i\vec{G}\cdot\vec{r}}, \tag{2.16}$$

where $\vec{G}$ are the reciprocal space lattice vectors. A periodic function can then be expanded in a plane wave basis:

$$\phi(\vec{r}) = \phi(\vec{r} + \vec{L}) = \sum_{\vec{G}} \phi(\vec{G}) e^{i\vec{G}\cdot\vec{r}}. \tag{2.17}$$

Hence, Bloch functions [17] can be used to represent the one-electron wave functions for electrons moving freely throughout the static potential of the ions. Since the Kohn-Sham potential is periodic, Bloch's theorem states that the eigenfunctions of the wave equation can be rewritten as the product of a plane wave $e^{(i\vec{k}\cdot\vec{r})}$ times a cell-periodic function $u_{\mathrm{n}\vec{\mathrm{k}}}(\vec{r})$:

$$\psi_{\mathrm{n}\vec{\mathrm{k}}}(\vec{r}) = u_{\mathrm{n}\vec{\mathrm{k}}}(\vec{r}) e^{i\vec{k}\cdot\vec{r}}, \tag{2.18}$$

where n is the band index and $\vec{k}$ is a wave vector. Applying equation 2.17, the cell-periodic function $u_{\mathrm{n}\vec{\mathrm{k}}}(\vec{r})$ can be expanded in a discrete set of plane waves:

$$u_{n\vec{k}}(\vec{r}) = \sum_{\vec{G}} c_{n\vec{k}}(\vec{G}) e^{i\vec{k}\cdot\vec{r}}. \tag{2.19}$$

Therefore the wave functions of the system are simply a sum over plane-waves:

$$\psi_{n\vec{k}}(\vec{r}) = \sum_{\vec{G}} c_{n\vec{k}}(\vec{G}) e^{i(\vec{k}+\vec{G})\cdot\vec{r}}. \tag{2.20}$$

Although this is a simple method, it requires a large number of plane waves to represent the electronic wave functions in the core region. Therefore, Orthogonalized Plane Wave (OPW) method was proposed. It contains basis functions that are orthogonalized with respect to all core states, which ensures a better convergence in the eigenvalues. Alternatively, people applied the Augmented Plane Wave method (APW) which assumes a muffin-tin crystal potential. The effective crystal potential was found approximately constant beyond certain cutoff core radius (R_c), so that the electronic wave function inside of R_c is atomic function like and the part outside of R_c is represented as plane waves. Note that the wave function at R_c has to remain continuous. However, both OPW and APW methods are computationally very demanding. As a result, Linearized Augmented Plane Wave method was developed on the basis of APW method. The wave function at R_c is designed not only continuous but also differentiable.

2.7 The Pseudopotential Method

As only the valence electrons participate in forming a chemical bond, the tightly bound core electrons can be neglected, since they are chemically very stable. The valence wave function oscillates rapidly as it approaches the core region, which requires

a very large plane-wave basis set to express. Hence, we replace the strong potential in the core region by a much weaker pseudopotential, while keeping the pseudopotential outside of the cutoff radius (r_c) identical with the all-electron potential. The resulting pseudo wave function in the core region would display no radial nodes, while the pseudo wave function outside of r_c is identical with the all-electron wave function 2.1. Basically, by using pseudopotentials, the core states no longer exist, and the valence pseudo wave functions are smooth close to the nuclei. The smoother pesudo wave function for the valence electrons means a much smaller plane-wave basis set.

In many atoms (especially transition metal elements, such as Ti and Cu), the valence and near-valence core states (also called semicore states) interact strongly. These semicore states cannot be simply treated as core states, since these play important roles in chemical bonding. It is very necessary to include semicore electrons into valence, which helps to increase the accuracy and transferability.

In order to guarantee a good match between the results generated from pseudopotential calculation and from all-electron calculation, it is important to make the pseudopotential norm conserving and non-local [55, 72, 105]. The norm-conserving pseudopotential means that the integrals from 0 to r_c of the all-electron and pseudo charge densities agree for each valence state. It guarantees the electrostatic potential outside of r_c is identical for all-electron and pseudo charge distributions, and is very important for optimal pseudopotential transferability [55]. Since different angular

momentum states are scattered differently, we need different pseudopotentials for accurate representation of different angular momentum s, p, d, f ...electronic states. The HSC (Hamann, Schlüter and Chiang) procedure generates non-local and norm conserving pseudopotentials [55].

For all-electron calculations (in Rydberg energy units), we have

$$\left[-\frac{d^2}{dr^2} - \frac{2Z}{r} + V_{\rm hxc}(r) + \frac{l(l+1)}{r^2}\right]\phi_l(r) = \varepsilon_l \phi_l(r) \tag{2.21}$$

We are able to convert the Kohn-Sham equation to find the screened semi-local pseudopotential V_l^{scr},

$$V_l^{scr} = \epsilon_l - \frac{l(l+1)}{r^2} + \frac{1}{\phi_l(r)}\frac{d^2\left[\phi_l(r)\right]}{dr^2} \tag{2.22}$$

By descreening the screened pseudopotential, we obtain the ionic pseudopotential:

$$V_l^{ps}(r) = V_l^{scr}(r) - V_{hxc}\left[\rho^{val}(r)\right] \tag{2.23}$$

Unfortunately, HSC is not very efficient pseudopotential form. Instead, there is another very efficient method to evaluate the angular momentum dependent pseudopotential contribution to the energy is by Kleinman and Bylander (KB) [55, 72, 105]. Within the KB representation, we can express the semi-local pseudopotential in non-local separable form.

$$\hat{V}_{NL} = \hat{V}_{loc}(r) + \sum_l \frac{|\delta\hat{V}_l(r)\psi_l >< \psi_l \delta\hat{V}_l(r)|}{< \psi_l|\delta\hat{V}_l(r)|\psi_l >} \tag{2.24}$$

where, $\delta V_l(r) = \hat{V}_l^{ps}(r) - \hat{V}_{loc}(r)$, $\hat{V}_{loc}(r)$ is arbitrary and ψ_l are the pseudo-atom wave functions. It is important to note that upon the use of KB pseudopotentials,

unphysical electronic states (ghost states) sometimes present and should be examined. The ghost states can be eigenstates with nodes with energies even below the zero-node state. We could avoid the ghost states by switching the local potential or changing the cutoff radii.

Figure 2.1: The pseudo wave functions for Ti are displayed.

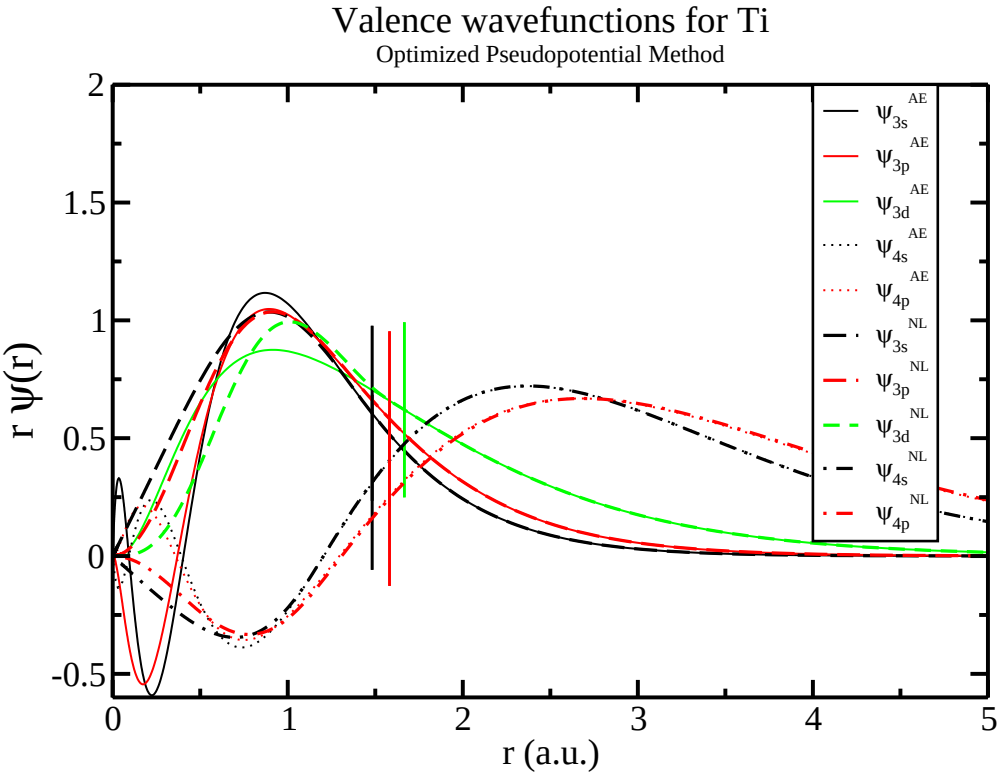
Valence wavefunctions for Ti
Optimized Pseudopotential Method
r ψ(r)
r (a.u.)
2
1.5
1
0.5
0
-0.5
0
1
2
3
4
5
ψ3s AE
ψ3p AE
ψ3d AE
ψ4s AE
ψ4p AE
ψ3s NL
ψ3p NL
ψ3d NL
ψ4s NL
ψ4p NL

By exploiting the flexibility of separating local and non-local components in the Kleinman-Bylander form, Ramer and Rappe presented a new method of generating pseudopotentials with enhanced transferability [103]. A local augmentation operator is added to the local potential $\hat{V}_l^{ps}(r) = (\hat{V}_{loc}(r) + \hat{A}) + \delta\hat{V}_l^{DNL}(r)$, we have

$$\delta\hat{V}_l^{DNL}(r) = \sum_l \frac{|(\delta\hat{V}_l(r) - \hat{A})\psi_l >< \psi_l(\delta\hat{V}_l(r) - \hat{A})|}{< \psi_l|(\delta\hat{V}_l(r) - \hat{A})|\psi_l >} \tag{2.25}$$

By adjusting $\hat{A}$, we are able to obtain better agreement between all-electron and pseudo eigenvalues.

2.8 Post-DFT Method

Although DFT has provided insights into various materials, it suffers from a notable number of shortcomings. One significant shortcoming is DFT's failure in terms of predicting proper band gap values for insulators and semiconductors. DFT seems to systematically underestimate the band gap by about 30-50% [63]. The failure is especially obvious for strongly correlated materials containing transition metal or rare earth ions. Since strongly localized d or f electrons are not well characterized in DFT. The strong electron-electron correlation needs to be taken into account. Also, although DFT is an exact theory to describe ground state properties, addressing excited state properties is beyond its scope. There are many ways to properly estimate the electronic band gap and other excited state properties, such as LDA+U and GW approximation.

GW approximation is for calculating self-energy in many-electron systems. It has emerged as a particularly successful method for accurate quantitative band structure calculations. Similar to Hartree-Fock approximation, single-particle approximation is applied, where exchange and correlation effect is rigorously contained in the self-energy operator. The electrons are treated as quasiparticles that closely mirror the real situation [23, 4, 79].

In LDA+U formalism (used in this thesis), a Hubbard U correction is taken to shift the LDA d/f orbitals. The delocalized s and p electrons could still be described by using LDA. The results depend strongly on the definition of the localized orbitals and the value of the interaction parameters used in the calculation. If one assumes that the total number of d electrons $N = \sum_i n_i$, we use the on-site d-d Coulomb interaction $\frac{1}{2}U\sum_{i\neq j} n_i n_j$ instead of the averaged Coulomb energy $\frac{1}{2}UN(N-1)$. We have the following functional:

$$E = E_{\mathrm{LDA}} - \frac{1}{2}UN(N-1) + \frac{1}{2}U\sum_{i\neq j} n_i n_j \tag{2.26}$$

The resulting LDA+U potential $V_i(\vec{r}$ by taking a variation on the charge density of a particular i-th orbital $n_i(\vec{r})$:

$$V_i(\vec{r}) = \frac{\partial E}{\partial n_i(\vec{r})} = V_{\mathrm{LDA}}(\vec{r}) + U(\frac{1}{2} - n_i) \tag{2.27}$$

The LDA+U eigenvalues (orbital energies) ϵ_i are derivatives of E with respect to the

orbital occupations n_i:

$$\epsilon_i = \frac{\partial E}{\partial n_i} = \epsilon_{i(\mathrm{LDA})} + U(\frac{1}{2} - n_i) \tag{2.28}$$

For occupied states, we have the occupied orbital energies $\epsilon_i = \epsilon_{i(\mathrm{LDA})} - \frac{U}{2}$, and the unoccupied orbital energies $\epsilon_i = \epsilon_{i(\mathrm{LDA})} + \frac{U}{2}$. These simple formulars shift the orbital energies and increase the electronic band gap.

Having this type of highly accurate DFT modeling is necessary for understanding the origin of the various properties exhibited by perovskites used in the current state-of-the-art technology, in order to improve the design of new materials with enhanced performances. Over the last decade, first-principles calculations emerge as a vital tool for studying complex solid bulk systems due to a combination of methodological improvements and faster computer speeds. DFT is an extremely successful approach for description of ground state properties of metals, semiconductors, and insulators [59, 73] because of a combination of accuracy and computational efficiency.

Chapter 3

Theory and Methodology—Molecular Dynamics

3.1 Introduction

The history of molecular dynamics (MD) dates back to the mid 1950's, when the first computer simulations on simple systems were performed. Initially, MD simulations were time consuming and computationally expensive. As the computing speed is getting faster and faster, even simulations of solvated proteins can be routinely calculated up to the nanosecond and microsecond time scales.

Molecular dynamics is one of the most important techniques for modeling a many-body system at atomic scale. MD simulations are in many aspects very similar to real experiments. We can investigate the equilibrium and transport properties, and model detailed microscopic dynamical behavior of many different types of systems as found in chemistry, physics or biology.

All the atoms, or ions are modeled classically. The dynamics is propagated by using Newton's equation of motion. Newton's second law $F = ma$ is the basic equation of motion for MD simulations, where F is the force exerted on the particle, m is the mass and a is the acceleration. With the interatomic potential known, the force on each atom can be derived, allowing the determination of a for each atom by integrating the equations of motion. It allows us to trace the trajectories that describes the positions x, velocities v and accelerations a for every particle as it moves in time t. From the trajectories, the average values of the properties of interest can be determined as a function of atoms' positions and momenta. The procedure is de-

terministic, i.e. once the starting positions and velocities of each particle are known, the state of the system can be predicted at any time in the future or the past [41].

All MD simulations should be performed under a certain ensemble condition, such as microcanonical NVE ensemble and canonical NVT ensemble. The system that we are interested needs to be evaluated first, and then we can choose a proper ensemble condition for representing the particular thermodynamic system of interest on a thermodynamic level. In this thesis, both NVE and NVT ensembles are picked under different circumstances [84].

3.2 Velocity Initialization

For a particularly assigned system (containing information such as the total number of atoms, temperature, pressure, and time duration), the MD simulation starts with initialization: the initial positions and velocities need to be set for all particles in the system. In most cases, the position information is given from the input file, while the velocities are not specified. As we know, the average thermal kinetic energy is related to the average temperature as following:

$$\langle \frac{1}{2} m v_\alpha^2 \rangle = \frac{1}{2} k_B T \tag{3.1}$$

where v_α is the α component of the velocity of a given particle. In thermal equilibrium, the above equation should hold. However, the initial velocities do not necessarily have to obey the Maxwell distribution, as the temperature deviates from the desired

anyway before equilibration. There are many ways to adjust velocities for the purpose of achieving constant temperature at equilibrium. Most commonly, velocity rescaling and Nosé-Hoover thermostat are applied to control velocities so that the average temperature match the desired T.

3.3 Integration Equations

After the velocities initialization, we need to perform the force calculation, which is the most time-consuming part of the simulation. In the simplest case only two-body interaction exists. It implies that, for a system of N particles, we need to evaluate $N(N-1)/2$ pair distances. Unfortunately, in most cases, taking into account only two-body interaction is insufficient, and the presence of many-body interaction would make the force evaluation even more expensive. If two atoms are close enough to interact, the forces need to be computed, so does the contribution to the potential energy $u(r)$:

$$f_x(r) = -\frac{\partial u(r)}{\partial x} \tag{3.2}$$

With the computed forces for all atoms, we can now integrate Newton's equation of motion. Different algorithms are designed for the best efficiency, among which Verlet algorithm is usually one of the simplest and the most efficient, a good balance point for both good speed and high accuracy.

$$r(t+\delta t) \approx 2r(t) - r(t-\delta t) + \frac{f(t)}{m}\delta t^2 \tag{3.3}$$

The estimation for the new position $r(t+\delta t)$ has an error of order δt^4, where δt is the time step. Other Verlet-like algorithms should be applied, if higher accuracy is wanted. In this thesis, we used the modified Beeman's equation to propagate our trajectories. The superscript p and c represent predicted and corrected respectively. The procedures are as following:

$$x(t+\delta t) = x(t) + \delta t\dot{x}(t) + \frac{\delta t^2}{6}[4\ddot{x}(t) - \ddot{x}(t-\delta t)] \tag{3.4}$$

$$\dot{x}(p)(t+\delta t) = \dot{x}(t) + \frac{\delta t}{2}[3\ddot{x}(t) - \ddot{x}(t-\delta t)] \tag{3.5}$$

$$\ddot{x}(t+\delta t) = f\left(x_i(t+\delta t), \dot{x}_i^{(p)}(t+\delta t), i = 1...n\right) \tag{3.6}$$

$$\dot{x}^{(c)}(t+\delta t) = \dot{x}(t) + \frac{\delta t}{6}[2\ddot{x}(t+\delta t) + 5\ddot{x}(t) - \ddot{x}(t-\delta t)] \tag{3.7}$$

Finally replace $\dot{x}^{(p)}$ with $\dot{x}^{(c)}$ and go to step 3.6, iterate until the predicted and corrected velocities have converged to a relative precision of better than 1 part in 10^{-7}. Any integration error, no matter how small, would always cause the deviation of a simulated trajectory from the true trajectory increases exponentially with time. However, the trajectory deviation is not considered to be crucial, as a MD simulation does NOT have to precisely predict what happens to the system starting from a known initial condition. We are only interested in the average behavior of the system, or we say statistical predictions.

3.4 Nosé-Hoover Thermostat

Here, we will introduce how we maintain a constant temperature for our simulation system by using Nosé-Hoover thermostat. A large enough heat bath is coupled with our system, and the heat reservoir controls the temperature of the given system, making the temperature fluctuate around target value. The thermal interaction between the heat reservoir and the system results in the exchange of the kinetic energy between them. The general idea is to use extended Lagrangian method. Assume that the system contains N atoms, with coordinates $q_i^{'}$, masses m_i, potential $U(q^{'})$, and momenta $p_i^{'}$. We introduce an additional artificial variable s, so that the virtual variables (coordinates q_i, momenta p_i and time t) are related to the real variables ($q_i^{'}$, $p_i^{'}$, $t^{'}$) as following:

$$q_i^{'} = q_i \tag{3.8}$$

$$p_i^{'} = p_i/s \tag{3.9}$$

$$dt^{'} = dt/s \tag{3.10}$$

We can derive the real velocity:

$$\frac{dq_i^{'}}{dt^{'}} = s\frac{dq_i^{'}}{dt} = s\frac{dq_i}{dt} \tag{3.11}$$

The artificial variable s plays the role of a time-scaling parameter. It stretches the timescale in the extended system by the factor s. The Lagrangian of the extended

system of the N-atom system combining variable s in terms of the virtual variables is

$$L_{Nose} = \sum_{i=1}^{N} \frac{m_i}{2} s^2 \dot{q}_i^2 - U(q) + \frac{Q}{2}\dot{s}^2 gkT \ln(s) \tag{3.12}$$

where, Q is an effective mass associated with s. The magnitude of Q determines the coupling between the reservoir and the real system, and it also influences the temperature fluctuations. g equals to the total number of degrees of freedom of the system. Please note that the logarithmic dependence of the potential on the variable s is very important for producing the canonical ensemble for the system. The momenta conjugate to q_i and s are:

$$p_i = \frac{\partial L_{Nose}}{\partial \dot{q}_i} = m_i s^2 \dot{q}_i \tag{3.13}$$

$$p_s = \frac{\partial L_{Nose}}{\partial \dot{s}} = Q\dot{s} \tag{3.14}$$

This gives the total Hamiltonian for the extended system:

$$H_{Nose} = \sum_{i=1}^{N} \frac{p_i^2}{2m_i s^2} + U(q) + \frac{p_s^2}{2Q} + gkT \ln(s) \tag{3.15}$$

Now, we could define the equations of motion:

$$\frac{dq_i}{dt} = \frac{\partial H_{Nose}}{\partial p_i} = \frac{p_i}{m_i s^2} \tag{3.16}$$

$$\frac{dp_i}{dt} = \frac{\partial H_{Nose}}{\partial q_i} = -\frac{\partial U}{\partial q_i} \tag{3.17}$$

$$\frac{ds}{dt} = \frac{\partial H_{Nose}}{\partial p_s} = \frac{p_s}{Q} \tag{3.18}$$

$$\frac{dp_s}{dt} = \frac{\partial H_{Nose}}{\partial s} = \frac{\sum \frac{p_i^2}{m_i s^2} - gkt}{s} \tag{3.19}$$

Chapter 4

First-Principles Investigation of A Highly Tetragonal Ferroelectric Material: $\mathbf{Bi(Zn_{1/2}Ti_{1/2})O_3}$

4.1 Introduction

Lead-free piezoelectric materials are attracting increased attention recently due to environmental concerns. Bi-based materials are considered as promising alternatives to Pb because of the similar $6s^2$ "stereochemically active lone pair" electron configuration. Bi^{3+} is likewise easily polarized, which promotes ferroelectric and piezoelectric properties. However, Bi-based materials are less stable than their Pb-based equivalents, and they are much less well studied. While numerous perovskite compounds based on Bi have been reported [65, 10, 9, 8], few form the perovskite structure under ambient conditions [76, 61]. In order to find better alternatives to the widely used ceramic solid solution $PbZr_{1-x}Ti_xO_3$ (PZT), many lead titanate ($PbTiO_3$, PT) solid solutions with morphotropic phase boundary (MPB) forming Bi-based additives have been studied [35, 138, 28, 88, 118, 50, 117]. Alloying with almost all Bi-based perovskites reduces the tetragonality of PT, but an unexpected enhancement of c/a was recently discovered in the $PbTiO_3$-$Bi(Zn_{1/2}Ti_{1/2})O_3$ (PT-BZT) solution. The c/a ratio of the system systematically increases with the addition of BZT, reaching a value of 1.11 at the limit of substitution ($\approx$ 50% BZT) under ambient pressure [118].

The preparation of BZT in perovskite form at high pressure was also reported recently. It has an extremely high c/a ratio (1.211), and the refinement of x-ray diffraction data found large Bi (0.88 Å) and Zn/Ti (0.60 Å) displacements. This was ascribed to the pronounced influence of the $6s^2$ stereochemically active electron

pair [120, 119]. The refinement of x-ray diffraction data also found large thermal factors even at room temperature. This is likely due to structural disorder in the system, which cannot be fit exactly with a five-atom unit cell used in a standard Rietveld refinement. Because BZT is such a strongly polar material, its polarization could not be easily measured. Instead, using the refined coordinates and formal ionic charges, the polarization magnitude was estimated to be 1.03 C/m^2. Despite the large differences in both charge and size between the Zn and Ti cations, the electron diffraction did not give any evidence for long-range or short-range order of the B sites. This is in contrast to $Pb(Sc_{1/2}Nb_{1/2})O_3$ and other perovskites with similar charge and size differences that exhibit rocksalt (111) type B-cation ordering [24]. The high tetragonality of BZT is also interesting in light of its low tolerance factor (t=0.95). Typically, such a low tolerance factor leads to the appearance of large octahedral tilts and therefore an antiferroelectric phase, as seen in $PbZrO_3$ (PZ) [114] and $Bi(Mg_{1/2}Ti_{1/2})O_3$ (BMT), the Mg analog of BZT [70].

In this work, we use first-principles density functional theory (DFT) methodology to study properties of BZT that are not available from any current experiments. We evaluate the polarization of the material and study the local environment, resolving displacements of individual ions as well as tilts of the O_6 octahedra. We investigate the energetics of B-site cation ordering in BZT and find that they are qualitatively different from the previously studied ferroelectric perovskites. Due to its extreme

tetragonality, the lowest-energy B-cation ordering is not rocksalt, but rather a (010) ordering with the planar stacking direction orthogonal to the direction of polarization.

4.2 Methodology

The local B site arrangements are studied using 40-atom supercells, which can be thought of as snapshots of small regions of the real disordered solution. The ABINIT software package was used to relax the ionic positions and lattice constants [46]. All atoms are represented by norm-conserving optimized [105] designed nonlocal [103] pseudopotentials generated using the OPIUM code [1] with a plane-wave cutoff of 60 Ry. A generalized gradient approximation (GGA) [94] and a $2 \times 2 \times 2$ Monkhorst-Pack sampling of the Brillouin zone [87] are used. Our calculations find both tetragonal and rhombohedral phase stable structures. GGA calculations find the experimentally observed tetragonal phase to be preferred, in contrast to the LDA calculations which find the opposite. Although GGA is known to generally overestimate lattice parameters of ferroelectric perovskites [131, 15], the slight overestimation of tetragonality compared with experiment (5%-6%) still makes the predictions reliable. For cubic lattice parameters, there are six possible arrangements of the Zn and Ti B cations in the 2×2×2 supercell. For the tetragonal lattice parameters, four of these arrangements have two different orientations relative to the (001) polar axis leading to a total of ten unique B-cation arrangements studied in this work (Fig. 4.1).

Figure 4.1: Ten B-cation arrangements for 40-atom tetragonal BZT supercells used in this work.

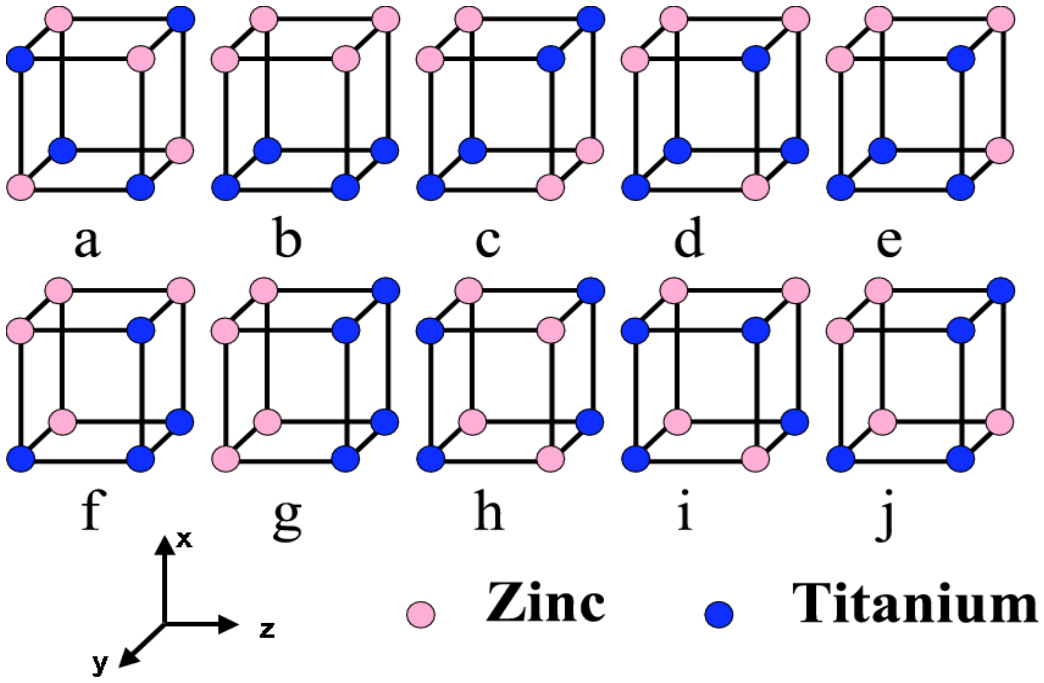
a
b
c
d
e
f
g
h
i
j
x
z
y
Zinc
Titanium

4.3 Results

4.3.1 Local structure

Since BZT is experimentally found to be tetragonal, we focus our analysis on the tetragonal ground states. First we analyze the size and the tilt angle of the O_6 cages from relaxed structures to characterize the distortions of the oxygen anions away from the perfect perovskite positions. For all relaxed supercells, the Zn-O_6 octahedra are larger than Ti-O_6 octahedra by ≈16%. As shown in Fig. 4.2, there is almost no overlap in the size distribution of the two types of octahedra. The difference in volumes is consistent with the ionic size difference of Zn and Ti cations (ionic radius of 0.740 Å for Zn and 0.605 Å for Ti). The peak at small volumes of the Ti-O_6 octahedra comes from structure (c) which differs from other structures in terms of c/a ratio and volume (as presented in Table 4.1).

Examination of the octahedral tilt angles reveals a broad distribution (from 0° -15°) (Fig. 4.2). A small tolerance factor means that the A-O sublattice prefers a smaller lattice constant than the B-O sublattice. Octahedral tilting preserves the large B-O cages, while decreasing the A-O distances, allowing both sublattices to achieve their preferences. While the majority of tilt angles are small and are comparable to the tilt angles found in tetragonal ferroelectric PZT [49], a significant fraction of tilt angles are larger, similar to the ones found in antiferroelectric materials such as BMT and PZ. The large octahedral tilts mostly come from structure

(c) and are expected from the tolerance factor analysis. The fact that most of the tilts are small shows that the tolerance factor argument is too simplistic to make correct ground-state crystal structure predictions [6]. In highly tetragonal materials, the large A-cation off centering creates short A-O distances. Thus, the octahedral tiliting is no longer the only possibility to achieve the preferences of both sublattices.

Table 4.1: DFT energetics (eV/five-atom cell), tetragonality, spontaneous polarization (C/m^2), electrostatic ordering energy (eV/five-atom cell), and the relative distances of Bi to Zn(Ti) cations (Å) are listed. The electrostatic energy is calculated using vacuum permittivity.

	DFT Energy	c/a	P	electrostatic	$R_{\mathrm{Bi-Zn}}$	$R_{\mathrm{Bi-Ti}}$
supercell c	0.0827	1.077	0.815	-3.911	3.36	3.47
supercell d	0.0759	1.266	1.368	-2.976	3.44	3.34
supercell j	0.0463	1.275	1.375	-2.626	3.41	3.36
supercell e	0.0442	1.276	1.381	-2.295	3.35	3.33
supercell i	0.0439	1.284	1.386	-3.683	3.37	3.32
supercell h	0.0408	1.280	1.354	-4.651	3.35	3.31
supercell b	0.0398	1.274	1.405	0.644	3.39	3.34
supercell a	0.0364	1.271	1.362	-5.100	3.43	3.28
supercell f	0.0211	1.280	1.398	-1.942	3.35	3.45
supercell g	0.0000	1.286	1.428	-1.611	3.42	3.48

Figure 4.2: Above: octahedral volume of Zn and Ti octahedra in BZT. The Zn cations always have larger octahedral cages than the Ti cations. Below: distribution of octahedral tilts away from the Cartesian axes. The majority of BZT structures have widely distributed tilt angles.

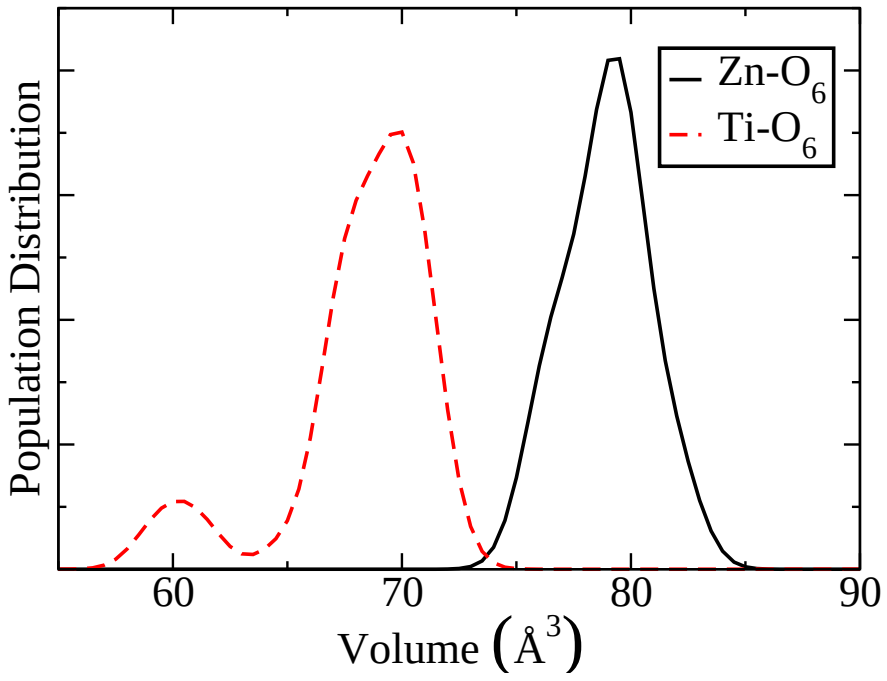
Population Distribution
Zn-O6
Ti-O6
60
70
80
90
Volume (Å3)

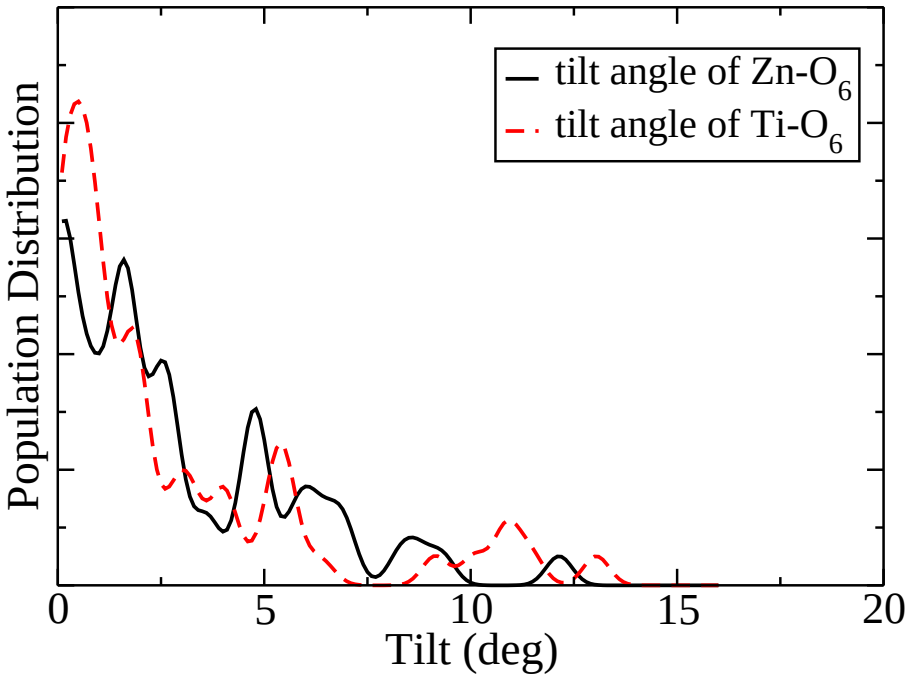
Population Distribution
tilt angle of Zn-O6
tilt angle of Ti-O6
0
5
10
15
20
Tilt (deg)

Relaxation of all ions yields large cation distortions. At the A site, Bi cations move by 1.0±0.1 Å, creating three or four short Bi-O bonds and transforming the Bi-O_{12} cages into a Bi-O_4 square pyramid. The creation of shorter Bi-O bonds is necessary to satisfy the Bi valence of 3, since the Bi valence is only 2.84 in the ideal cubic perovskite structure. Off-center displacements are also favored by the long-range electrostatic interactions. At the B site, both Zn and Ti cations move off center by 0.6-0.7±0.1 Å, creating short Zn-O and Ti-O bonds and making an important contribution to the overall polarization (Fig. 4.3).

We find that the directions of individual cation displacement are distributed in a cone of about 25° around the (001) overall polarization direction (Fig. 4.3). In agreement with previous results for the PZT solid solution [49], the A-site displacement directions vary more than the B-site displacement directions. This is due to the influence of the B-cation arrangement on cation displacements which is stronger for the A site [50]. To avoid oxygen underbonding and overbonding, Bi cations tend to avoid the high-valence Ti and move toward the low-valence Zn. A simple illustration is provided by considering the Bi off-center distortions of structure (b). The Bi cations moving toward Zn cations move off center by about 1.21 Å along the (001) direction, while the Bi cations facing Ti cations move off center by about 0.79 Å along the (001) direction. The displacements of Bi cations facing the Zn cations are purely along (001), while the Bi cations facing Ti cations exhibit a significant (0.41 Å)

displacement component in the xy plane.

Figure 4.3: Above: distribution of cation displacements (Å) away from the oxygen cage centers. Below: angle distribution of cations away from the tetragonal direction.

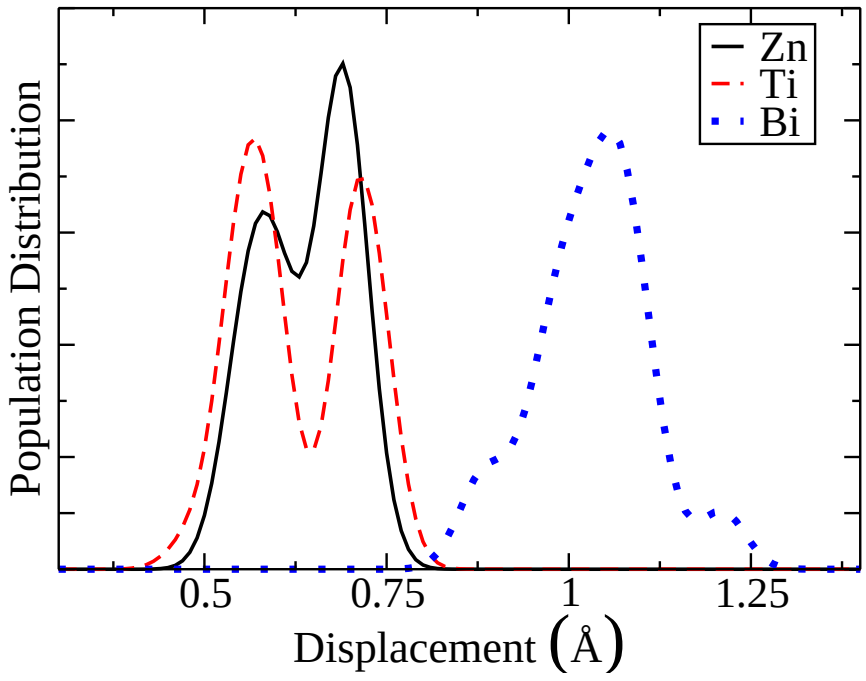
Zn
Ti
Bi
Population Distribution
0.5
0.75
1
1.25
Displacement (Å)

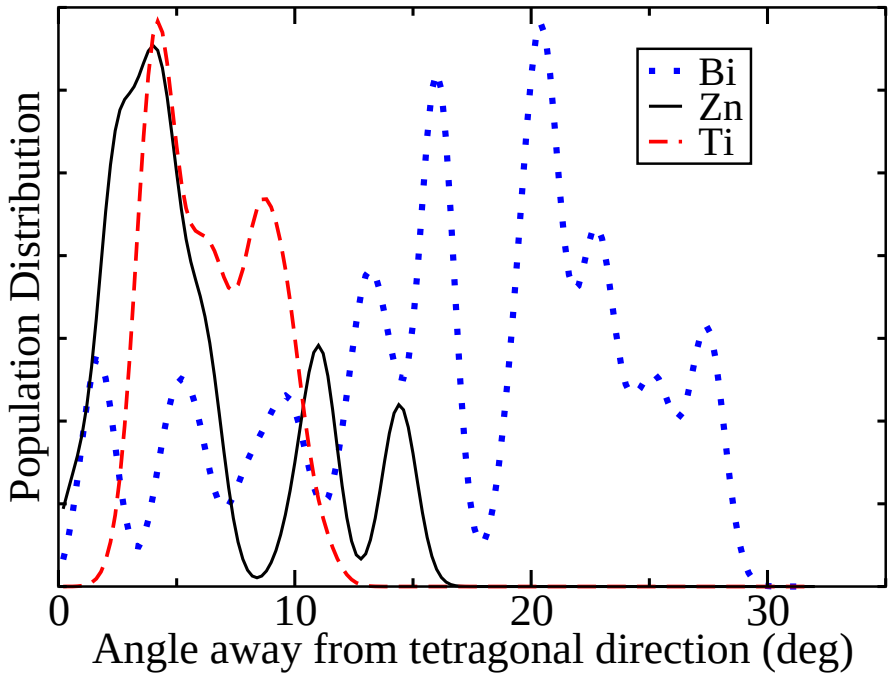
Bi
Zn
Ti
Population Distribution
0
10
20
30
Angle away from tetragonal direction (deg)

The broad distributions found for cation displacement magnitude and direction account for the large thermal factors found by experimental Rietveld refinement. A thermal factor of 0.05 Å^2 found by Suchomel *et al.* for the Bi cations is equivalent to a thermal vibration amplitude of about 0.1-0.22 Å. Such a large vibration is not reasonable at low temperature [68] and is better explained by the variation in displacement magnitudes and directions of Bi cations found by our 0 K calculations. Experimental thermal factors for the Zn and Ti cations are about half those of the Bi cations, corresponding to the narrower distribution for Zn and Ti displacements in Fig. 4.3. Thus, while the c/a of BZT is much greater than that of PT, local structure shows a resemblance to the $Pb(Mg_{1/3}Nb_{2/3})$-$PbTiO_3$ and PZT solid solutions of smaller c/a.

4.3.2 Strain and polarization

The total occupation of the B site by highly ferroelectrically active Zn and Ti cations and the coupling of A-site and B-site distortions allows extremely large cation displacements, stabilizing large polarization and strain. With the exception of supercell (c), we find that polarization of all supercells are in the 1.35-1.43 C/m^2 range; c/a is in the 1.27-1.29 range (Table 4.1). Thus, for the most part, the variation in B-cation ordering has only a minor impact on the polarization of the material. We found that our calculated polarization is significantly larger than the one estimated by Suchomel

et al. (1.03 C/m^2). The reason for this is that they used formal ionic charges which are smaller than the Born effective changes (Z^*). The 1.38 C/m^2 average polarization found for BZT is to our knowledge the largest known polarization for a stable ground state of a material.

The large polarization indicates that the Curie temperature (T_c) of BZT is also high, as T_c was found to be proportional to the square of the polarization for a variety of ferroelectrics. Using the proportionality constant between T_c and P^2 obtained from previous work (870 Km^4/C^2) [51], we can estimate the T_c of BZT as 1656 K, well above its decomposition temperature and higher than the 1400 K T_c of $LiNbO_3$, the highest known T_c in a perovskite-related ferroelectric to date.

4.3.3 Energetics of B-cation ordering

First-principles examination of the energetics of Zn/Ti ordering in BZT reveals unique features not found in other perovskites. Analysis of x-ray diffraction data carried out by Suchomel *et al.* did not find any B-cation rocksalt ordering peaks for BZT. It is possible that in BZT the energy differences between the rocksalt ordering and other B-cation arrangements are small; thus, no ordering will be observed except for a very careful annealing protocol. This is to be expected as previous work showed that large off centering due to the stereochemically active lone pair reduces the preference for rocksalt in Pb-based perovskites as compared to Ba-based perovskites [24]. Alterna-

tively, it is possible that unlike the case of Ba- and Pb-based perovskites, B-cation ordering other than rocksalt is preferred for BZT. Our DFT calculations show that the latter is true, with two of the ten possible $2\times2\times2$ supercell B-cation arrangements lower in energy than the rocksalt ordering.

The energetics of the different B-cation arrangements are presented in Table 4.1 and Fig. 4.4. The lowest energy 40-atom supercell exhibits a (010) ordering, with Zn and Ti planes alternating perpendicular to the tetragonal direction. This is in contrast with Ba- and Pb-based perovskites where such an ordering is the highest in energy. We attribute the unusual preference for (010) ordering to the extreme tetragonality of BZT. Our finding implies that with a slow enough annealing schedule it should be possible to synthesize the (010) ordered BZT in the bulk. This is quite unusual, as until now planar (001) or (010) B-cation ordering has only been achieved in the bulk for the $La(Cu_{1/2}Sn_{1/2})O_3$ material [2].

Figure 4.4: DFT energy differences from the lowest energy B-cation arrangement shown for the relaxed tetragonal (black) and rhombohedral (red) structures. Also shown are the electrostatic energy differences for the relaxed cubic structures computed using formal ionic charges (blue). To facilitate comparison, the energy differences for the cubic structures are scaled down by factors of 100.

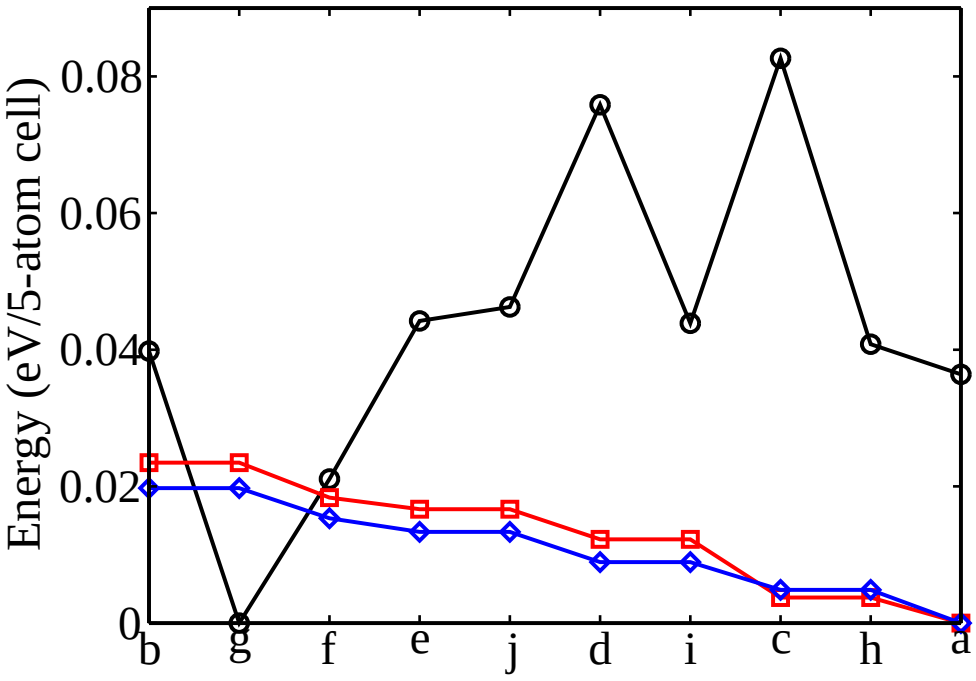
Energy (eV/5-atom cell)
0.08
0.06
0.04
0.02
0
b
g
f
e
j
d
i
c
h
a

To verify that it is the extreme tetragonality of BZT that is causing the anomalous preference for the (010) ordering, we determine the energetics of rhombohedral BZT supercells (Fig. 4.4). Here, due to the tetragonal symmetry breaking, only six B-cation arrangements are possible in a $2\times2\times2$ supercell. We find that for rhombohedral BZT, the rocksalt B-cation ordering is the lowest in energy and the planar (010) ordering is the highest in energy, following the B-cation arrangement energy ranking seen previously in Ba-based and Pb-based perovskites. The energy ranking follows exactly the electrostatic energy differences for the cubic, undistorted BZT structures, as can be seen from Fig. 4.4. The energy difference between electrostatically favored (111) B-cation ordering and the less favored (010) ordering in Pb-based systems such as $Pb(Sc_{1/2}Nb_{1/2})O_3$ (PSN) [24] is about four times larger than the energy difference in BZT. This is most likely due to the high covalency and the large off centering of the Bi cations. Burton and Cockayne [24] argued that the Pb $6s$-O $2p$ hybridization enables bonding of Pb cations to the underbonded oxygen atoms, which reduces the energy cost of deviation from the (111) B-cation arrangement. Bi exhibits even greater covalency and hybridization than Pb, so it is not surprising that the large Bi off-center distortions reduce the B-cation ordering energy differences more. Thus, in the rhombohedral phase, the cation distortions set the scale of the energy differences between the different B-cation orderings, while the electrostatics determines the energy ranking.

Electrostatic interactions are also important in tetragonal BZT, as shown by the comparison of the energies of the B-cation arrangements that are only different due to breaking of cubic symmetry by the tetragonal distortion. For example, for the case of (001) or (010) ordering where Zn and Ti cations are arranged in alternating planes [structure (b) and (g)], the DFT energy is higher for structure (b) with the tetragonal distortion parallel to the Zn/Ti sheet stacking direction and is lower for structure (g) with the tetragonal distortion perpendicular to the stacking direction. We consider the Zn cation as negative point charge and the Ti as positive charge (relative to the average formal charge of the B sites). On one hand, there are attractive electrostatic interactions between the Zn and Ti sheets. On the other hand, the electrostatic interactions within each sheet are repulsive. A tetragonal distortion parallel to the stacking direction leaves the repulsion unchanged and weakens the attractions. Conversely, a tetragonal distortion perpendicular to the stacking direction weakens repulsions and leaves the attractions unchanged. This leads to a higher energy for structure (b) as compared to structure (g). Similar arguments are applicable for explaining the other energy splittings between structures (d) and (i), (e) and (j), and (c) and (h).

The inadequacy of the electrostatic model [12] to explain BZT B-cation ordering energetics suggests that there are important contributions other than electrostatics. Repulsion between the A-site and B-site cations, both of a direct and of through-

oxygen kind, have been found to be important for compositional phase transitions in ferroelectrics [48, 52]. These interactions are particularly important for materials where the large A-site displacements from high symmetry decrease the A-B cation distances, as is the case of BZT. We expect Bi-Ti repulsion to be more important due to the greater charge of the Ti cation, and we use the position of the first peak in the Bi-B cation partial pair-distribution function (PDF) as a rough measure of the strength of the Bi-B cation repulsion (Table 4.1)).

To reduce the Bi-Ti repulsion, Bi cations favor avoiding Ti and moving toward Zn. Such a preference can be best satisfied by the B-cation arrangements where Zn and Ti cations are grouped separately. This is opposite to the effect of the electrostatic interactions, which are favorable when Zn and Ti cations are interspersed. The (010) planar ordering of Zn and Ti easily allows the Bi cations to avoid Ti cations, raising the minimum Bi-Ti distance (3.48 Å) and lowering repulsive energy. Similarly, the highly grouped Zn and Ti cations in arrangement (f) lead to large Bi-Ti distances and low repulsion. For the rocksalt structure (a), the alternation of Zn and Ti cations makes it impossible to avoid Ti, giving rise to the shortest observed Bi-Ti distances (3.28 Å) and a high repulsive energy. For the (001) planar Zn and Ti ordering, the need to avoid Ti conflicts with the strong displacement along (001) that are required by the strain-polarization coupling. This makes the Bi-Ti distances shorter than in the (010) structure.

4.4 Conclusion

We report a first-principles study of BZT. We demonstrate that this material has a number of unique properties, generated by its large c/a. Despite its macroscopic similarity with PT, BZT exhibits a disordered local structure similar to that of PZT. To the best of our knowledge, the polarization of 1.38 C/m^2 is the largest one reported for a bulk material (57% larger than P of PT). The relationship among c/a, P and T_c allows us to predict a T_c of about 1600 K for BZT, larger than the 1460 K of the current highest T_c ferroelectric $LiNbO_3$. Finally, examination of the B-cation ordering energetics shows that the planar (010) stacking of Zn and Ti is the favored B-cation arrangment, unlike the rocksalt ordering typically favored in perovskite materials. We ascribe this anomalous effect to the greater importance of Bi-B cation repulsive interactions in BZT, driven by the large cation displacements in the material. A more general electrostatic model by Wu and Krakauer [132] included the effective charge on the A sites, depending on the local B-site configuration. In this approach, fitting to first-principles calculations is required, which might give interesting insights into the extent of Bi covalent bonding with O in different B-cation arrangements.

Chapter 5

Correlations between tetragonality, polarization, and ionic displacement in $PbTiO_3$-derived ferroelectric perovskite solid solutions

5.1 Introduction

In Chapter 4, we discussed highly tetragonal ferroelectric material BZT. And now in Chapter 5, equipped with better understanding of this type of perovskite oxides, we proceed to systematically look into solid solutions that resemble BZT.

Perovskite ferroelectrics are a class of materials of fundamental scientific interest as well as varied technological applications [11, 106, 16]. Tetragonal distortion of the lattice is particularly important. It has long been known that a tetragonal end member is crucial for promoting high piezoelectric performance at the solid solution's morphotropic phase boundary (MPB) [117]. Recently, novel Bi-based ferroelectrics possessing extreme tetragonality (c/a = 1.1-1.25) have been discovered [118, 120, 115, 53], far surpassing $PbTiO_3$ ($c/a = 1.06$). The large spontaneous polarization and structural anisotropy of highly tetragonal ferroelectric materials make them promising for areas such as negative thermal expansion, multiferroics, birefringent optics [26, 60, 67].

A fundamental goal of materials science is to understand how a material's composition gives rise to its properties. Since the landmark paper of Devonshire [33], Landau-Ginzburg-Devonshire (LGD) theory has been proved to be a powerful tool for studying ferroelectrics. As a phenomenological model, LGD theory treats the macroscopic observable polarization (P) as the order parameter. If the LGD parameters are known, predictions can be made relating properties to each other within a

given material. However, the property changes due to compositional variation cannot be determined by standard LGD theory. The lack of an effective and quantitatively accurate theoretical tool for understanding how compositional changes affect tetragonality hinders the search for new materials with enhanced properties. Previously, we were the first to show that a simple universal proportionality relates the ferroelectric-paraelectric transition temperatures in $PbTiO_3$-based solid solutions to the square of their ground state polarization (P^2) [50, 51].

In this work, using first-principles calculations, we show that the use of a microscopic property, the average cation off-center displacement, as the order parameter in the LGD framework enables prediction of tetragonality by a simple expression. The displacement-strain coupling parameter is general for a large number of $PbTiO_3$-derived ferroelectric perovskite solid solutions. We also elucidate the crystal chemical properties that control the average atomic displacement in perovskites. Together, these two advances provide a roadmap for the design of new ferroelectric materials.

5.2 Methodology

We study 25 different tetragonal ferroelectric materials using density functional theory (DFT) [59, 96]. The details of the computational approach are the same as in previous work [50, 51]. Four different cation arrangements with minimal oxygen over- and under-bonding [49, 50] are used to study 0.25 Bi$M^{3+}$$O_3$-0.75 $PbTiO_3$. Only one

cation arrangement was used for 0.125 Bi$M^{3+}$$O_3$-0.875 $PbTiO_3$. Berry's phase calculations [126] were carried out to obtain the polarization. All data are presented in Table 5.1.

Table 5.1: DFT and experimental data for tetragonal $PbTiO_3$-derived ferroelectric perovskite solid solutions. A- and B-cation averaged displacements (D_A, D_B) and polarization (P), averaged over several different cation arrangements, are DFT predictions. All the displacement data listed here are for the (001) components of the total displacement vectors. Data marked by † and $*$ are taken from our previous works, Ref. [50, 51]. The c/a-1 and Curie temperature (T_c) data are from experimental literature [117, 118]. The T_c datum for $Bi(Zn_{1/2}Ti_{1/2})O_3$ is omitted, since this compound decomposed before undergoing phase transition [120].

	c/a-1	P	T_c	D_B	D_A
PT †	0.065	0.87	765	0.280	0.450
0.75 $PbZn_{1/3}Nb_{2/3}O_3$-0.25 PT †	0.033	0.66	547	0.218	0.461
0.5 $PbZrO_3$-0.5 PT	0.023	0.76	659	0.165	0.440
0.5 $PbSc_{1/2}Nb_{1/2}O_3$-0.5 PT	0.020	0.50	560	0.142	0.296
0.5 $PbIn_{1/2}Nb_{1/2}O_3$-0.5 PT	0.028	0.45	623	0.129	0.255
0.375 $PbSc_{2/3}W_{1/3}O_3$-0.625 PT	0.020	0.61	517	0.176	0.350
0.375 $PbMg_{1/3}Nb_{2/3}O_3$-0.625 PT †	0.044	0.66	583	0.201	0.387
0.375 $PbZn_{1/3}Nb_{2/3}O_3$-0.625 PT †	0.048	0.74	643	0.241	0.424
0.33 $PbZrO_3$-0.67 PT	0.046	0.84	700	0.210	0.450
0.25 $PbSc_{1/2}Nb_{1/2}O_3$-0.75 PT	0.041	0.74	640	0.220	0.412
0.25 $PbIn_{1/2}Nb_{1/2}O_3$-0.75 PT	0.046	0.65	695	0.208	0.387

	c/a-1	P	T_c	D_B	D_A
$Bi(Zn_{1/2}Ti_{1/2})O_3$	0.220	1.34		0.489	0.903
0.5 $Bi(Mg_{1/2}Ti_{1/2})O_3$-0.5 PT $*$	0.047	0.88	733	0.200	0.515
0.5 $Bi(Zn_{1/2}Ti_{1/2})O_3$-0.5 PT $*$	0.120	1.17	1100	0.365	0.675
0.25 $Bi(Mg_{1/2}Zr_{1/2})O_3$-0.75 PT $*$	0.041	0.86	721	0.216	0.478
0.25 $Bi(Mg_{1/2}Ti_{1/2})O_3$-0.75 PT $*$	0.061	0.93	803	0.258	0.505
0.25 $Bi(Zn_{1/2}Zr_{1/2})O_3$-0.75 PT $*$	0.064	0.93	740	0.263	0.508
0.25 $Bi(Zn_{1/2}Ti_{1/2})O_3$-0.75 PT $*$	0.088	1.04	875	0.319	0.550
0.25 $BiScO_3$-0.75 PT	0.040	0.84	768	0.220	0.488
0.25 $BiGaO_3$-0.75 PT	0.057	0.84	768	0.226	0.447
0.25 $BiInO_3$-0.75 PT	0.080	0.90	856	0.257	0.539
0.125 $BiAlO_3$-0.875 PT	0.050	0.84	758	0.243	0.473
0.125 $BiScO_3$-0.875 PT	0.053	0.85	780	0.257	0.442
0.125 $BiGaO_3$-0.875 PT	0.057	0.83	757	0.241	0.427
0.125 $BiInO_3$-0.875 PT	0.077	0.94	847	0.295	0.535

5.3 Results

Figure 5.1: Linear correlations for the average cation displacement (D_A^2 in blue squares and D_B^2 in black circles) vs experimentally observed c/a-1 and theoretical P^2 (P^2 in red triangles) and experimentally observed c/a-1 are shown. Unlike D_A^2 and P^2, D_B^2 is closely correlated with c/a-1. All of the fits shown are forced to cross the origin.

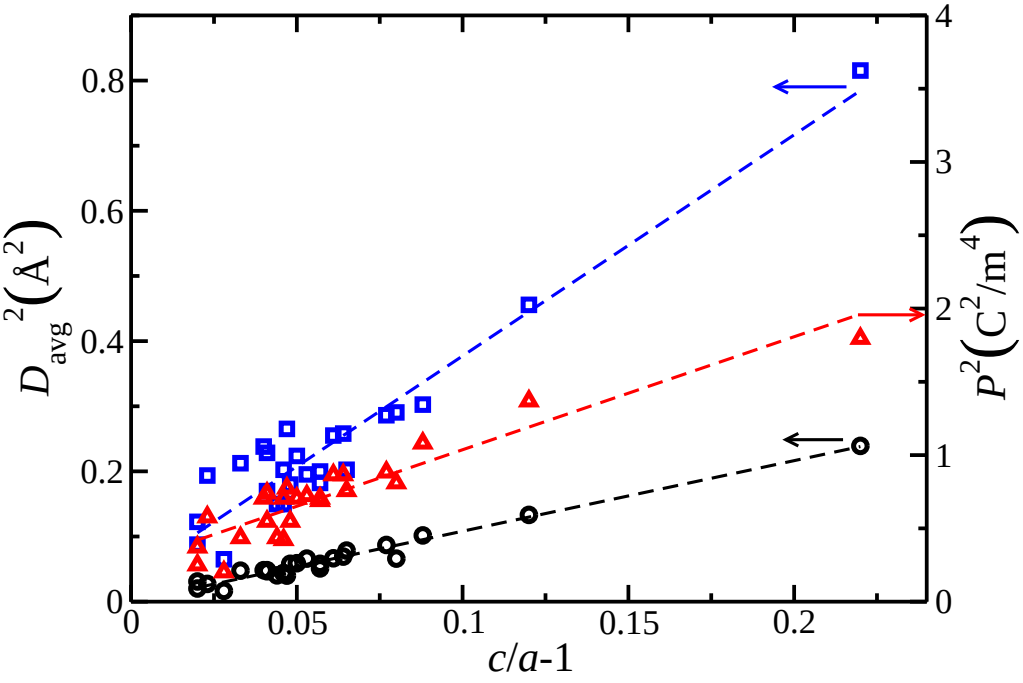
0.8
0.6
0.4
0.2
0
0
0.05
0.1
0.15
0.2
c/a-1
D_avg^2(Å^2)
4
3
2
1
0
P^2(C^2/m^4)

Table 5.2: Fitting functions set I is simple linear regression. R is the notation for correlation coefficient. Fitting parameters a, b and d are in the unit of Å^{-2}, e is in the unit of m^4C^{-2}, and c is unitless. Fitting functions set II is forced to cross the x-axis at the origin. By using different fitting variables to fit strain (s), we conclude that D_B^2 is the most universal parameter with the best linear correlation with s.

Fitting functions set I	R
$aD_A^2 + c$	0.958
a = 0.2703, c = -0.0054	
$bD_B^2 + c$	0.984
b = 0.8938, c = 0.0020	
$aD_A^2 + bD_B^2 + c$	0.985
a = 0.0553, b = 0.7236, c = -0.0003	
$dD_A D_B + c$	0.983
d = 0.5016, c = -0.0025	
$aD_A^2 + bD_B^2 + dD_A D_B + c$	0.986
a = -0.2646, b = -0.5987, d = 1.2928, c = 0.002	
$eP^2 + c$	0.924
e = 0.1108, c = -0.0208	

Fitting functions set II	R
aD_A^2	0.946
$a = 0.2466$	
bD_B^2	0.984
$b = 0.9058$	
$aD_A^2 + bD_B^2$	0.985
$a = 0.0530$, $b = 0.7201$	
dD_AD_B	0.981
$d = 0.4820$	
$aD_A^2 + bD_B^2 + dD_AD_B$	0.986
a = -0.2664, b = -0.6019, d = 1.3082	
eP^2	0.807
$e = 0.0816$	

Comparison of the correlations between the experimental c/a-1 values and the *ab initio* data P^2, average A-site off-center displacement squared (D_A^2) and average B-site off-center displacement squared (D_B^2) shows that D_B is the parameter that controls tetragonality. Figure 5.1 presents a general trend of higher P corresponding to higher c/a-1; however, the correlation weakens at high P values. In Fig. 5.1, similarly poor linear correlation is found for $c/a - 1$ and D_A^2. On the other hand, we find that $c/a - 1$ and D_B^2 are strongly correlated, with all of the data points falling close to a straight line through the origin. Including D_A^2, D_B^2 and the $D_A D_B$ cross terms for fitting the c/a-1 data does not significantly improve the correlation coefficient, proving that tetragonality is only weakly dependent on A-site displacement, and that the correlation between c/a-1 and D_A^2 comes from the coupling between the A- and B-site displacements.

It is important to note that a simple linear regression yields nonzero intercepts for $c/a - 1$ vs D_A^2, and $c/a - 1$ vs P^2. However, the same linear regression finds that the fit for $c/a - 1$ versus D_B^2 goes naturally through the origin. The nonzero intercepts for the linear regression fits of $c/a - 1$ vs D_A^2, and c/a-1 vs and P^2 come from the large scatter in the data. If additional solid solutions were included, the values of the x-axis intercept for these fits should also be zero.

Our results suggest the following interpretation. First, tetragonality has a universal scaling with average B-cation displacement in ferroelectric $PbTiO_3$ derived solid

solutions for a variety of A- and B-site compositions. Second, the modified LGD theory with B-site displacement replacing P as order parameter can be used to predict tetragonality of the different compositions. This model can be understood intuitively, by emphasizing that the mechanical property of tetragonality should be more strongly correlated with another mechanical property, atomic displacement, rather than an electrical property such as polarization. We describe the strain-displacement coupling contribution to the free energy in terms of D_A and D_B by:

$$G = -\gamma_A s D_A^2 - \gamma_B s D_B^2 - \gamma_{AB} s D_A D_B + \frac{1}{2} K s^2 \tag{5.1}$$

where strain s is the tetragonality c/a-1, and γ and K are the strain-displacement coupling and the elastic constants, respectively. Minimizing the free energy with respect to s, we get

$$s = (\gamma_A D_A^2 + \gamma_B D_B^2 + \gamma_{AB} D_A D_B)/K. \tag{5.2}$$

The high quality of the fit to D_B^2 data in Fig. 5.1 means that γ_A and γ_{AB} are small compared to γ_B, and can be neglected.

On the other hand, if the free energy G is written in a standard form with the overall polarization P_{tot} as the order parameter, the minimum-energy s is given by

$$s = \gamma (Z_A^* D_A + Z_B^* D_B)^2 / K \tag{5.3}$$

where we express P_{tot} as the sum of the A- and B-site contributions given by the average product of cation displacement and its Born effective charge Z^*. This forces the coupling constants between s and A- and B-site off-center displacements squared to scale as the their respective Z^* squared. In Table 5.2, fit $aD_A^2 + bD_B^2 + c$ shows that the γ_B/γ_A ratio is ≈ 13, much larger than the $(Z_B^*/Z_A^*)^2$=3.4 ratio for $PbTiO_3$. The disagreement is even worse for $Bi(Zn_{1/2}Ti_{1/2})O_3$, where $(Z_B^*/Z_A^*)^2$=1.4. The overestimation of the A-site contribution in the fit of s data to P^2 weakens the correlation and leads to the unphysical result that $P_{\text{tot}} \neq 0$ when s=0, fit $eP^2 + c$ in Table 5.2, making P_{tot} a less accurate predictor of c/a.

The interplay between bonding and geometry in a perovskite structure explains the differences in the strain dependence on the cation displacements of the A- and B-sites. We consider a strain along the (100) direction. For the B-cations, a (100) off-center displacement is along the O-B-O axis and strongly affects the B-O bond orders along that direction. Increased strain elongates the (100) lattice constant allowing more space for the B-cation distortion and making B-cation off-centering displacement more favorable [31]. For the A-site, there is a $\approx 45^\circ$ angle between the (100) direction of the A-cation off-center displacements and the (110) direction of the A-O bonds. In this case, a tetragonal strain leads to relatively small changes in the A-O bond length and its bond order. Hence, displacement-strain coupling for the A-cations is not as strong as for the B-cations.

At first glance, the weak correlation between c/a-1 and P found in our work contradicts the well-known scaling of the tetragonality with the square of polarization as temperature is varied. However, since D_A and D_B are coupled, for a single material, temperature variation changes P_A and P_B and therefore P_{tot} in a similar way, so that P_{tot} has a strong correlation with c/a-1 as T is varied. However, changing the composition affects one cation site more strongly than the other. For example, P_A is more affected by A-site substitution, while P_B is more affected by the B-site substitution. As a result, the proportionality between c/a-1 and P_{tot}^2 no longer holds tight for compositional variation.

Figure 5.2: The average B-cation ionic size effect R^B_{avg} on average cation displacement D_A and D_B in solid solution x BiM^{3+}O$_3$ - (1-x) PbTiO$_3$ is shown. Compositions x = 0.125 and x = 0.25 are noted as unfilled and filled symbols respectively. Ionic displacements are increased by substitution of either very large (In^{3+}, R_{In} = 0.80 Å) or very small (Al^{3+}, R_{Al} = 0.53 Å) R_M. 0.25 BiAlO$_3$ - 0.75 PT lattice constants are estimated from extrapolation.

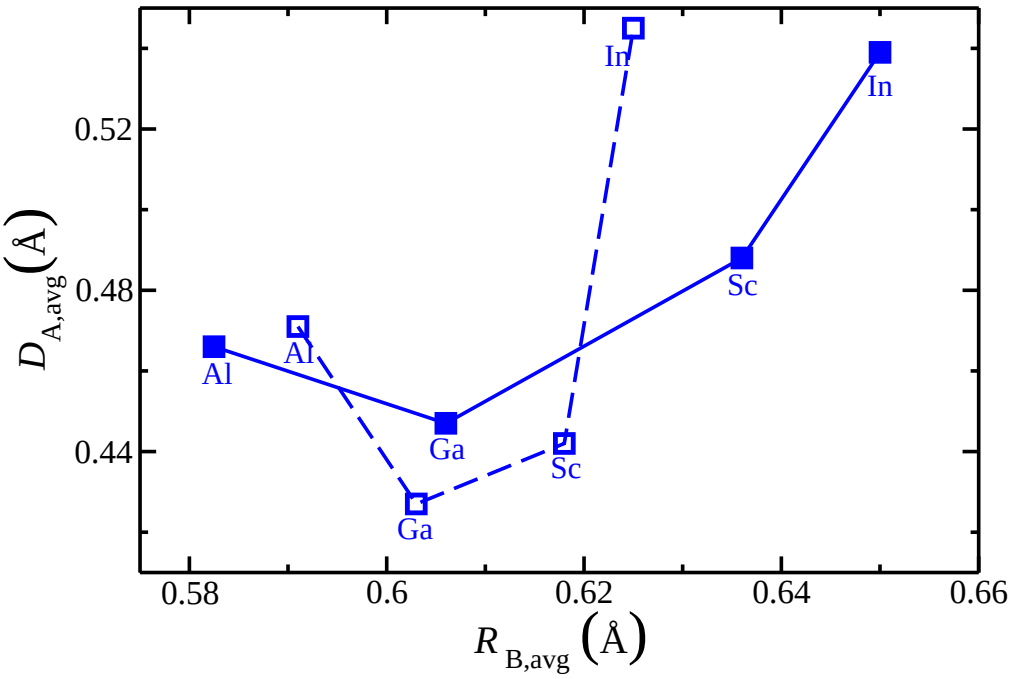
0.52
0.48
0.44
$D_{A,avg}$ (Å)
0.58
0.6
0.62
0.64
0.66
$R_{B,avg}$ (Å)
Al
Al
Ga
Ga
Sc
Sc
In
In

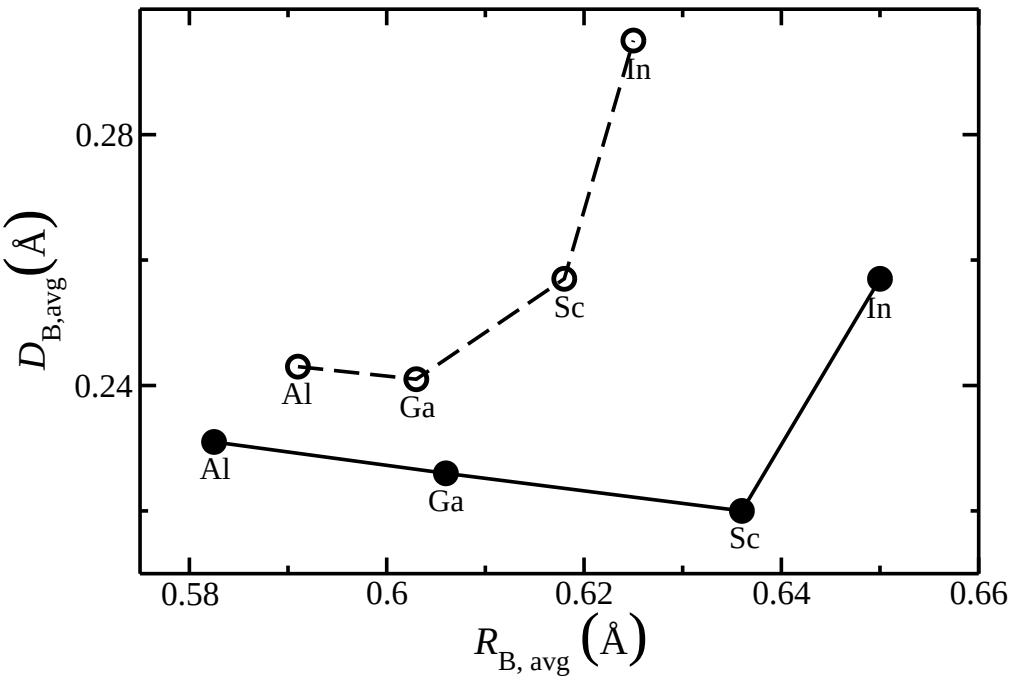
0.28
0.24
$D_{B,avg}$ (Å)
0.58
0.6
0.62
0.64
0.66
$R_{B,avg}$ (Å)
Al
Ga
Sc
In
Al
Ga
Sc
In

The relationship between D_B and c/a elucidated here, as well as the previously-obtained correlation between P and T_c reduce the problem of new ferroelectric material design to that of enhancing D_A and D_B values. In previous work, we found that DFT-obtained cation displacements D_M in ferroelectric $PbTiO_3$-based solid solutions are remarkably transferable from one material to another. [51] The displacement tendency of each cation can therefore be characterized by parameter D_M^0, the displacement that cation M would make in almost pure $PbTiO_3$ at a very low doping fraction. The D_M^0 value variation cannot be explained by ionic size argument alone, since it is also closely related to the covalency of the M-O bond, with higher covalency leading to enhanced ionic displacement. This can be illustrated by a comparison of the more covalent Zn^{2+} (D_{Zn}^0=0.25 Å, R_{Zn}=0.74 Å) and more ionic Mg^{2+} (D_{Mg}^0=0.08 Å, R_{Mg}=0.72 Å) cations [50, 51].

Here, we examine the ionic size R impact on D_B, by holding D_B^0 nearly constant. We performed *ab initio* calculations on x BiMO$_3$ - (1-x) $PbTiO_3$ (M^{3+} = Al^{3+}, Ga^{3+}, Sc^{3+}, In^{3+}). Fig. 5.2 shows that both $D_{A,\mathrm{avg}}$ and $D_{B,\mathrm{avg}}$ average displacement magnitudes depend non-monotonically on the average B-cation ionic size $R_{B,\mathrm{avg}}$, implying two competing effects exist and they switch dominant role depending on $R_{B,\mathrm{avg}}$. Also we can see that the two effects are influenced by the doping fraction of BiMO$_3$. The B-site displacements are more sensitive to the change in x as seen for a larger shift of the minimum cation displacement values. Next, we discuss the two effects for small

and large ionic size substituents.

When R_M is small, the increase in the ionic displacement for smaller B-site can be explained by the well-known rattling cation effect. The mismatch between the short cation-oxygen bonds preferred by the dopant ion and the larger lattice constant preferred by the A-O sublattice favors off-centering of the dopant and an increase in the average A-site and B-site displacements.

When R_M is large, the increased ionic displacements D_B for large substituent B-site ions (*e.g.* In^{3+}) are due to the expansion of the crystal volume. Introducing very large cations on the B-site creates a conflict between the preference of the subsitutent for a larger unit cell volume and the preference of the A-cations for a smaller A-O sublattice. Usually, such a conflict is resolved by the rotation of the B-O_6 octahedra; however, for a low concentration of large B-cations, the stiffness of the TiO_6 octahedra in $PbTiO_3$ and their resistance to tilting make these large rotations energetically unfavorable. [54] Instead, the A-site off-centering increases, bringing the A-cations closer to the O anions to achieve the desired short A-O bonds. Thus, in a solid solution, alloying a larger-volume perovskite into a smaller-volume one expands the A-site for the smaller A-cations, equivalent to applying negative pressure [122] to the smaller-volume perovskite.

The understanding of the relationships between cation characteristics and the technologically important T_c and c/a properties of perovskite ferroelectrics provides

guidance for the design of new materials with enhanced performance. For example, the finding that tetragonality scales with the B-site displacement means that compositions with a small charge on the A-site (*e.g.* Ag^+-based ABO_3) can be extremely tetragonal. For enhancement of c/a and P at small dopant fraction, large cation size and displacement are favorable. At higher substituent fraction, smaller ionic size is favorable, suggesting that cations such as Al^{3+} ($R_{Al} = 0.53$ Å) and V^{4+} ($R_V = 0.58$ Å) and V^{5+} ($R_V = 0.54$ Å) are promising for enhancing polarization and c/a.

For $PbTiO_3$-derived piezoelectric materials, the highest performance occurs at the MPB. For operation at high temperatures, the T_c at the MPB must be high. To create an MPB, a rhombohedral or antiferroelectric perovskite is mixed with $PbTiO_3$, to destabilize the tetragonal phase and reduce c/a (typically, MPB compositions exhbit $c/a \approx 1.025$). From the demonstrated correlations above, reduction in c/a means that the B-site displacement must be diminished. However, high T_c is favored by large polarization, with contributions from both A- and B-cation displacements. Hence, the optimal strategy is to mix in a perovskite with $D_B^0 < D_{Ti}^0$ and $D_A^0 > D_{Pb}^0$; this decreases c/a while the increased A-site polarization compensates for the smaller B-site P contribution. Another strategy is to substitute large cations on the B-site. As shown above in Fig. 5.2 at higher x, a large substituent increases D_A while decreasing D_B, driving c/a down while maintaining a high P and T_c. This type of combination is in fact observed for the x $BiScO_3$ - (1-x) $PbTiO_3$ [36] and x $BiMg_{1/2}Ti_{1/2}O_3$ - (1-x)

$PbTiO_3$ [117, 104] solid solutions. These exhibit an immediate decrease in c/a but an initial rise in T_c which leads to enhanced T_c^{MPB} compared to the classic $Pb(Zr,Ti)O_3$.

5.4 Conclusion

In conclusion, using DFT calculations we have revealed a universal scaling of c/a in ferroelectric perovskites with the displacement of the cation B-site. The developed composition-structure-property relations provide guidance for systematic exploration of new materials. Of course, we are aware of the fact that providing guidance for structural geometry is not enough for all perovskite oxides' applications, road maps for how to design materials with electronic structure serving versatile purposes are also important. We will continue to discuss the electronic structure engineering in the next chapter, Chapter 6.

Chapter 6

First-Principles Investigation of Electronic Band Gap Coupling to Local Environment in Complex Oxides

6.1 Introduction

In Chapter 6, we study some specially chosen perovskite oxides to study the electronic band structure coupling with structural geometries.

Ferroelectric (FE) photovoltaic materials have recently attracted increasing attention for use in solar cell applications. The strong inversion symmetry breaking and spontaneous polarization P of ferroelectrics separate charge carriers well [64, 42], making them a promising class of photovoltaic materials [135, 29, 125]. However, the poor matching of the band gap E_g of most perovskite ABO_3 FE materials (3-4 eV) with the solar spectrum greatly reduces their solar energy conversion efficiency. In the last decades, great efforts have been made to understand electronic band structures [34, 121, 130, 128, 37, 66, 97] and to engineer a lower electronic band gap in oxide materials [44, 14] using first-principles calculations. In this work, we use first-principles DFT calculations to explore how B-site ordering, lattice strain, cation identity and oxygen octahedral cage tilts affect the electronic band gap in highly tetragonal ferroelectric perovskites. We find that local chemistry can be used to reduce the band gap by 1-2 eV and achieve the desired combination of low band gap, high polarization and high electron mobility in FE perovskites.

We first focus our study on the newly synthesized $Bi(Zn_{1/2}Ti_{1/2})O_3$ (BZT), as well as proposed materials $Bi(Zn_{3/4}W_{1/4})O_3$ (BZW) and $Bi(Zn_{3/4}Mo_{1/4})O_3$ (BZM). BZT experimentally exhibits tetragonal symmetry [120], while BZW and BZM relax into

orthorhombic symmetry. These are environmentally friendly, exhibit extremely large tetragonality c/a and P, either in the pure state [120] or in an alloy with $PbTiO_3$ (PTO) [117, 115], fulfilling the high polarization requirement.

Figure 6.1: Five B-cation arrangements for 40-atom tetragonal BZW and BZM supercells used in this work. Bi and O ions are omitted in the sketch.

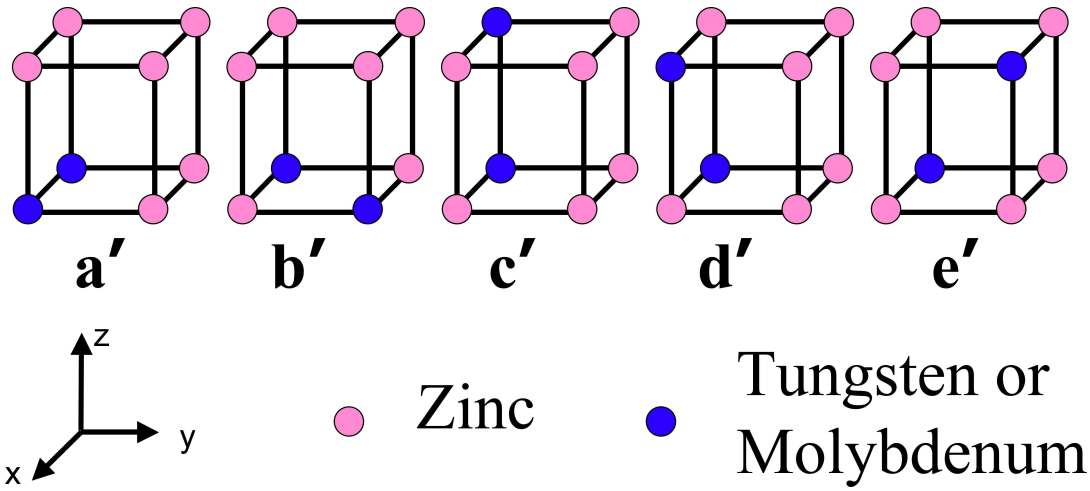
a′
b′
c′
d′
e′
z
y
x
Zinc
Tungsten or
Molybdenum

6.2 Methodology

We studied the local environment and electronic structure of each oxide with density functional theory (DFT). We used the ABINIT program [46] to investigate 2×2×2 40-atom supercells, relaxing the internal ionic coordinates and lattice parameters. All atoms are represented by norm-conserving optimized [105] nonlocal [103] pseudopotentials generated using the OPIUM code [1] with a 60 Ry plane-wave cutoff. We used the GGA [94] and a $2 \times 2 \times 2$ Monkhorst-Pack k-point sampling of the Brillouin zone [87]. Orbital-projected densities of states (PDOS) are calculated with 8×8×8 k-point meshes and Gaussian smearing. The plain DFT underestimates E_g of semiconductors and insulators by 30-50% [63]. For instance, PTO E_g is underestimated by $\approx$ 1.5 eV. To address some of the shortcoming of DFT (concerning localized orbitals), the LDA+Hubbard U (LDA+U) method was developed by using the on-site Coulomb interaction instead of the averaged Coulomb energy for localized d and f electrons [3, 30]. Appropriate Hubbard U values for Ti, Zn, W and Mo are estimated from the binary oxides (TiO_2, ZnO, WO_3 and MoO_3) and ABO_3 (PTO and $BaTiO_3$) whose experimental E_g are well-known. It should be noted that the presented results do not qualitatively change for reasonable variations of U. However, since LDA+U has the shortcoming of predicting densities of states inaccurately, we only apply LDA+U for correcting E_g values. DFT is used for local structure relaxation and band dispersion analysis.

In cubic phase BZT, there are in total six possible B-cation arrangements in a 40-atom supercell. When the lattice symmetry becomes tetragonal, four of these arrangements have two different orientations relative to the (100) polar axis leading to a total of ten unique B-cation arrangements as in Fig. 4.1. The 3:1 Zn-B' cation ratio leads to five possible arrangements for tetragonal phase 40-atom supercells of BZW and BZM, as shown in Fig. 6.1.

6.3 Results and Discussion

All three oxides show significant cation displacement and spontaneous polarization. Since A-site Bi^{3+} is small and very covalent, it usually moves off-center by a large amount (≈ 1 Å). B-site Zn is known as a ferroelectrically active cation [52], showing large displacement. Because of the B-site and A-site displacement coupling [101], we observe large cation off-centering and large polarization for all three materials. The local geometries and energetics of the relaxed BZW and BZM structures resemble BZT, as found in our previous study [100]. The general cation displacement trend is $D_{\mathrm{Bi}} > D_{\mathrm{Zn,Ti}} > D_{\mathrm{W,Mo}}$. With smaller D_{Bi} and smaller averaged B-site Born effective charges in BZW and BZM, their polarization magnitude is about 20% smaller than that of BZT. BZW and BZM also show larger O_6 octahedral rotations and non-(001) cation displacement components, due to their smaller tolerance factors of 0.934, compared with 0.949 for BZT.

Figure 6.2: Cation displacement (top) and oxygen octahedral tilt angle (bottom) population distributions averaged over all supercells for BZT (left), BZW (center) and BZM (right). Bi, Zn, Ti, W and Mo data are plotted in black, red, green, blue and purple.

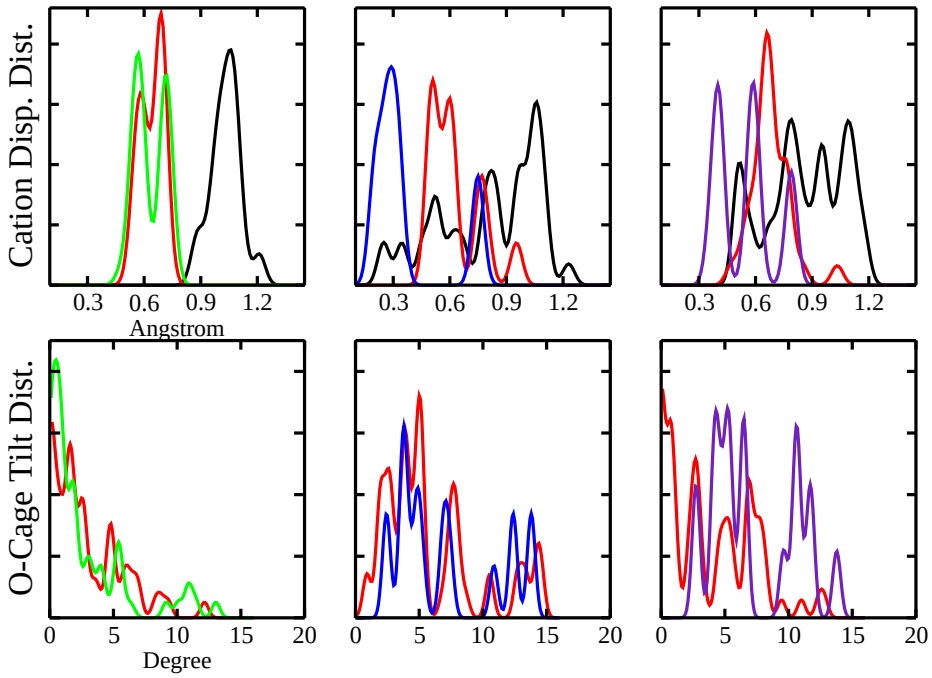
Cation Disp. Dist.
0.3
0.6
0.9
1.2
Angstrom
O-Cage Tilt Dist.
0
5
10
15
20
Degree

Table 6.1: BZT is experimentally determined to show tetragonal symmetry [120]. Some B-cation orderings lead to uneven two short lattice constants, within 5% difference in magnitude. We take the average of the two for caculating approximate tetragonality c/a. DFT energies (eV/5-atom cell), tetragonality, polarization (C/m^2) $\hat{z}$ component and total magnitude, E_g (eV, LDA+U), and averaged O_6 tilting angles ($^\circ$) are presented for relaxed structures. The subscripts i and d indicate indirect and direct E_g. Γ/Z means a k-point that is in between Γ and Z.

	E_{DFT}	c/a	P_z	P_{tot}	E_g	transition	O_6 tilt
BZT							
a	0.036	1.271	1.36	1.39	2.24_d	$\Gamma \rightarrow \Gamma$	1.5
b	0.040	1.274	1.41	1.42	1.48_i	Γ/Z$\rightarrow \Gamma$	2.4
c	0.083	1.077	0.82	1.05	2.77_i	R$\rightarrow \Gamma$	9.7
d	0.076	1.266	1.37	1.38	1.93_i	X$\rightarrow \Gamma$	2.5
e	0.044	1.276	1.38	1.40	2.13_i	A$\rightarrow \Gamma$	2.4
f	0.021	1.280	1.40	1.40	2.13_i	Z$\rightarrow \Gamma$	2.6
g	0.000	1.286	1.43	1.43	2.09_d	$\Gamma \rightarrow \Gamma$	2.4
h	0.041	1.280	1.35	1.39	2.37_d	$\Gamma \rightarrow \Gamma$	0.6
i	0.044	1.284	1.39	1.42	2.24_d	$\Gamma \rightarrow \Gamma$	1.0
j	0.046	1.275	1.38	1.39	2.17_i	X$\rightarrow \Gamma$	2.9

Figure 6.3: Band structures for BZT arrangements a (top) and b (bottom) near the fermi level. The high-symmetry points in the Brillouin zone are Γ (0, 0, 0), X(0.5, 0, 0), M (0.5, 0.5, 0), A(0.5, 0.5, 0.5), Z(0, 0, 0.5) and R(0.5, 0, 0.5).

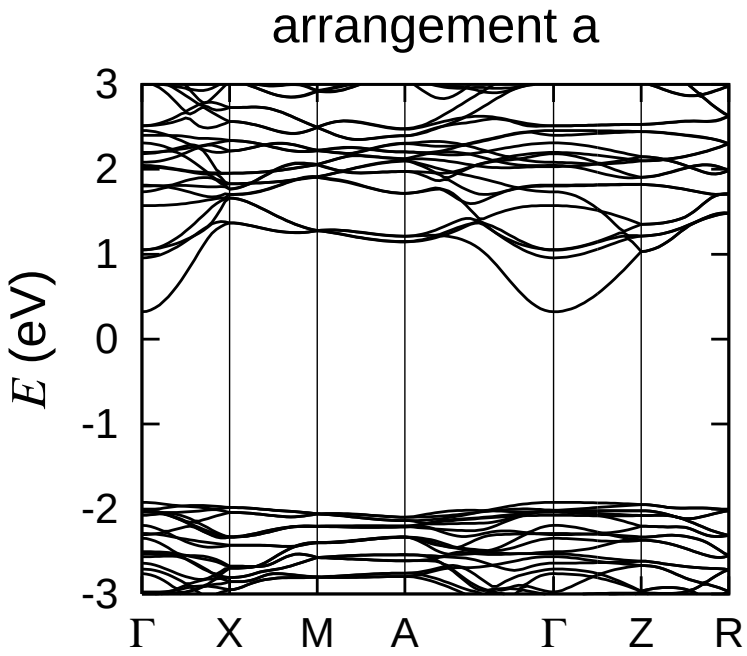
arrangement a
3
2
1
0
-1
-2
-3
E (eV)
Γ
X
M
A
Γ
Z
R

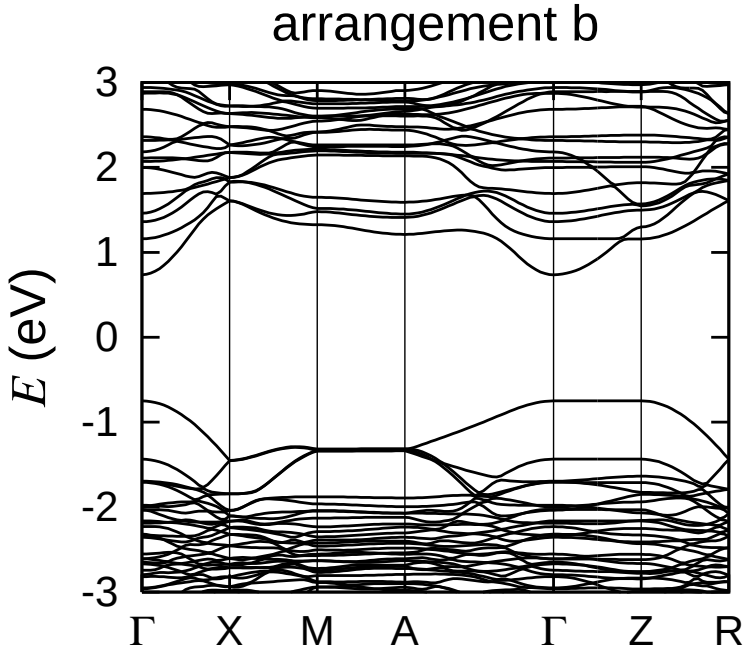
arrangement b
3
2
1
0
-1
-2
-3
E (eV)
Γ
X
M
A
Γ
Z
R

Figure 6.4: Projected density of states for BZT *B*-cation arrangements b. Bi, O, Ti and Zn data are plotted in black, red, green and blue.

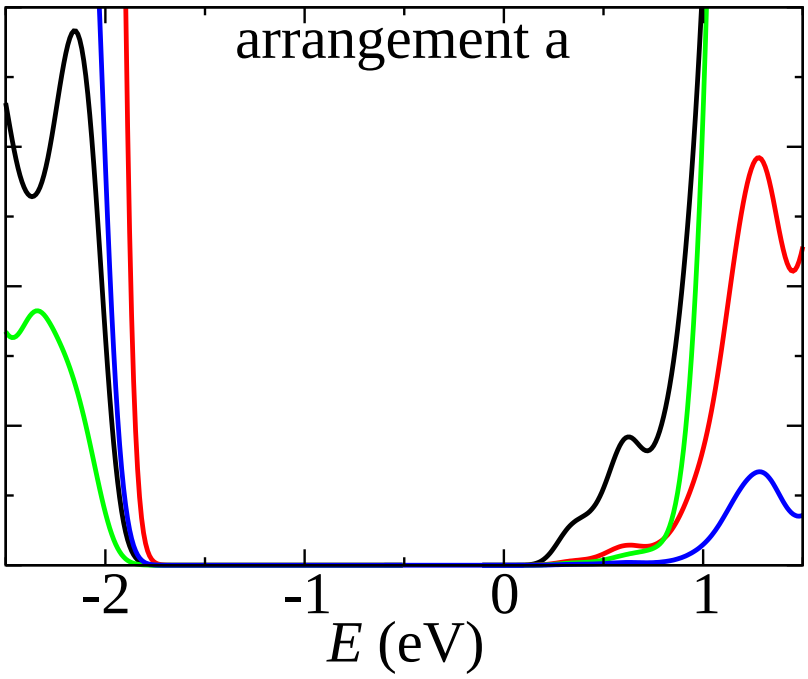
arrangement a
-2
-1
0
1
E (eV)

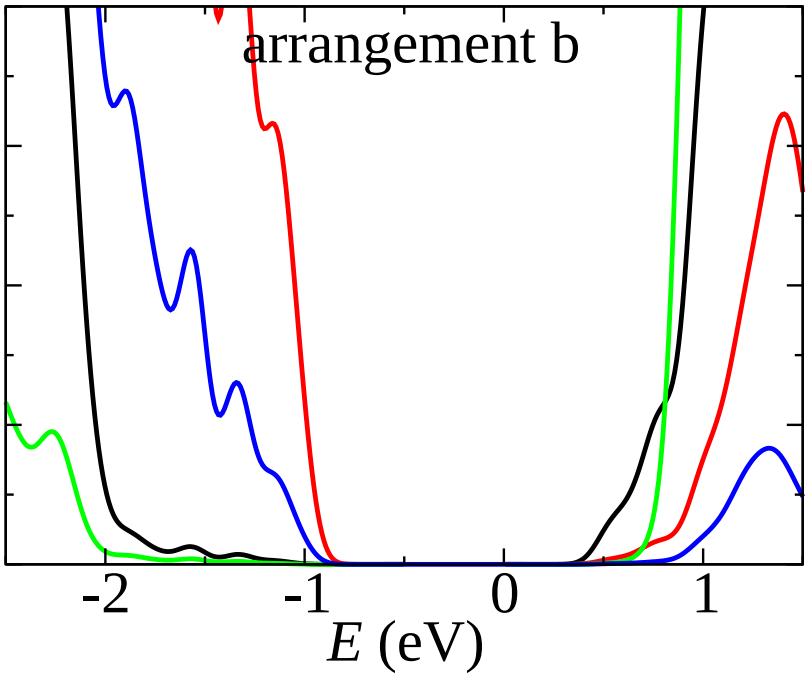
arrangement b
-2
-1
0
1
E (eV)

For the three Bi-based materials, analysis of the ground state wavefunctions shows that the valence band is mostly O $2p$ with some Zn $3d$. The conduction band is chiefly Bi $6p$ with some transition metal d and O $2p$. This is different from many previously studied ferroelectrics, where the valence band maximum and conduction band minimum usually consist of O $2p$ and the B-site transition metal d states (*e.g.* Ti $3d$ in PTO), respectively. In addition to the unusual presence of the A-site cation states at the conduction band minimum, we find that the Zn $3d$ states are located at or just below the valence band maximum.

6.3.1 The effect of B-cation ordering

The proximity and connectivity of Zn cations have a strong impact on the electronic structure (Figure 4.1 and Table 6.1). For all ten B-cation arrangements we study here, the E_g values are approximately 2.2 eV, except for supercell b. This structure exhibits a significantly lower band gap of 1.48 eV and has alternating Zn and Ti B-cation layers stacked along the polar axis. Ju *et al.* [67] reported E_g lowering in this specific B-cation arrangement using a 20-atom supercell, but did not discuss or explain the origin of this effect. An even stronger difference ($\approx$ 1 eV) between the arrangements containing all-Zn xy planes, and the other arrangements is obtained for the BZM and BZW structures relaxed under the constraints of uniaxial polarization and suppressed O_6 rotations (Table 6.3). We will refer to these as constrained structures in further

discussion.

What is the reason for such strong E_g sensitivity to B-cation arrangement? Figure 6.3 shows that while the conduction bands of arrangements a and b have similar energy and dispersion, the top valence bands of arrangement b rise by ≈ 1 eV relative to arrangement a. The major atomic orbital components of the valence band maximum are O $2p_x$ and O $2p_y$ for arrangement a; Zn $3d_{x^2-y^2}$, O $2p_x$ and O $2p_y$ for arrangement b. Additionally, in arrangement b, the O orbitals at the valence band maximum come only from the O atoms in the all-Zn plane, and the higher energies of the Zn $3d_{x^2-y^2}$ orbitals lead to a decreased band gap (1.48 eV).

The significant Zn $3d_{x^2-y^2}$ character at the valence band maximum can be explained in a crystal field theory framework. The filled Zn $3d$ states have a repulsive interaction with the O $2p$ states. The differences in shape and orientation of the five Zn $3d$ orbitals lead to a difference in the strength of repulsion, breaking the Zn $3d$ degeneracy. In cubic perovskites, the transition metal B-sites are surrounded by six closest oxygen atoms in an octahedral environment, in which d_{z^2} and $d_{x^2-y^2}$ are degenerate. By contrast, because of the high c/a ratio in BZT and significant B-cation off-centering displacement, every Zn atom is in a square pyramidal coordination with five nearest-neighbor oxygen atoms. The Zn $3d$ orbitals split, with $3d_{x^2-y^2}$ highest in energy, since it has the largest overlap with the O $2p_x$ and O $2p_y$. Thus, the change from octahedral to square pyramidal geometry due to extreme tetragonality destabi-

lizes the Zn $3d_{x^2-y^2}$ orbitals in BZT, which rise toward the valence band maximum. This effect is present for both arrangements a and b. However, in arrangement b an additional crystal field effect due to the presence of an all-Zn plane leads to a further destabilization of the Zn $3d_{x^2-y^2}$ orbital, as we discuss next.

Figure 6.5: Schematic picture shows the bond order variation caused by B-cation arrangement. The bold and dashed lines indicate stronger and weaker bonds respectively.


Bi
Zn
O
Ti
Bi
Zn
O
Zn

Figure 6.6: The charge density contour plots for constrained BZT structures a and b. The top and bottom rows are B-O and A-O bonding plane respectively. In structure a, the Zn-O bond is weaker than Ti-O bond. We observe stronger Bi-O bond (close to the all-Zn plane) in structure b than in structure a. In structure b, the strongly underbonded O atoms between two Zn atoms are compensated by a stronger bond from their nearest Bi neighbors. The charge density is in the unit of $e^-/bohr^3$.

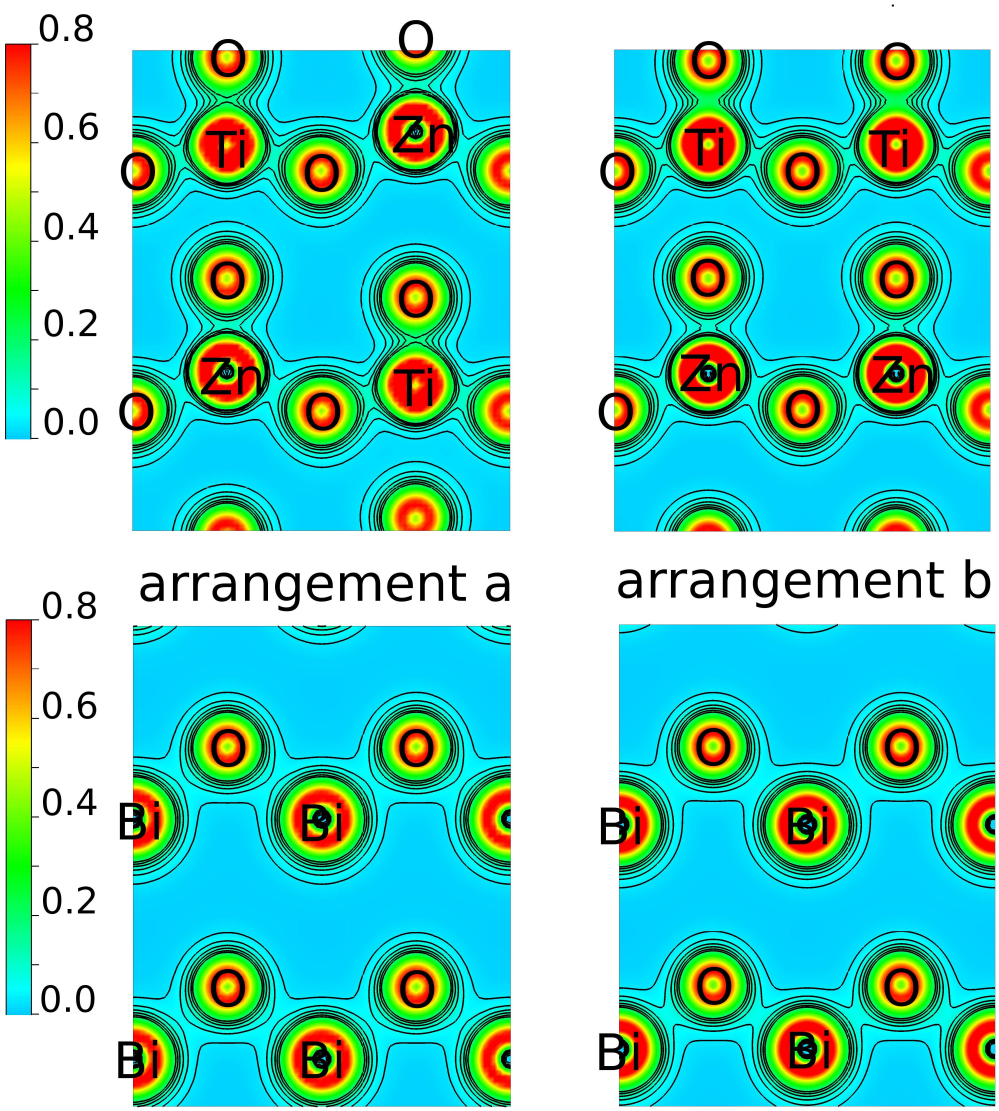
0.8
0.6
0.4
0.2
0.0
O
Ti
Zn
arrangement a
arrangement b
Bi

The O atoms in an all-Zn xy plane layer are underbonded. In BZT, the average total valence of each O atom's B-site neighbors is six (Zn^{2+}+Ti^{4+}). This is the case for all the O atoms in arrangement a. When an O atom has two Zn neighbors, the total valence of its B-site neighbors is only four. The B-O bonding is weaker than average, and the underbonded O valence must be compensated by the creation of shorter and stronger Bi-O bonds. This can be seen by comparing the Born effective charges and Bi-O bond lengths for the O atoms in arrangements a and b. The O Z^*_{xx} element of the Born effective charge tensor is -3.2 for arrangement a but only -2.1 for the O atoms in the all-Zn plane in arrangement b. Similarly, the shortest Bi-O distance is 2.41 Å in arrangement a and 2.33 Å in arrangement b, indicating that a stronger Bi-O bond valence compensates the weaker B-O bonding in arrangement b. Comparing electron density distributions of the two arrangements, we see that there is a depletion of density from the B-site opposite the Zn atom as the Ti-O bond is replaced by the Zn-O bond, and a build up of charge density in the Bi-O bonds closer to Zn (Fig. 6.6). Such an electron density redistribution increases the repulsion between the O $2p_x$, O $2p_y$ and Zn $3d_{x^2-y^2}$ orbitals. It destabilizes the Zn $3d_{x^2-y^2}$ even more, raises its energy to the valence band maximum, and decreases E_g, as observed in BZT arrangement b.

6.3.2 strain effect

To explore the connection between the extreme tetragonality and the unusual cation-arrangement sensitivity of E_g, we calculated the E_g values for the tetragonal-symmetric BZT arrangements a and b at a range of lattice parameters (Table 6.2). As we will discuss later, O_6 octahedral rotation is another important local environment effect. Therefore, to isolate the effect of strain, we varied the lattice parameters without oxygen cage tilt.

We find that the c/a ratio is a good predictor of the E_g sensitivity to the cation arrangement. Decreasing c/a, either by a smaller c lattice parameter or larger a, makes the band gap difference between arrangements a and b ($\Delta E_g^{\mathrm{a-b}}$) smaller. In contrast, neither the volume nor the individual lattice constants a and c are good predictors of $\Delta E_g^{\mathrm{a-b}}$ (Table 6.2). Reducing the c lattice parameter reduces the square pyramidal crystal field splitting of the Zn d orbitals, dropping the Zn $d_{x^2-y^2}$ states below the valence band maximum and reducing $\Delta E_g^{\mathrm{a-b}}$. Increasing a decreases the electrostatic repulsion between the O $2p$ states and the filled Zn $3d$ states, and $\Delta E_g^{\mathrm{a-b}}$ is also reduced. These two effects are of approximately the same magnitude, such that a simultaneous increase of a and c leads to only slight changes in $\Delta E_g^{\mathrm{a-b}}$. Thus, a large c/a ratio is crucial for strong sensitivity of E_g to B-cation arrangement.

Table 6.2: c/a ratio, a and c lattice constants (Å), 5-atom cell volume (Å^3), E_g for B-cation arrangements a and b (eV, LDA+U), and their difference (eV) are presented for structures relaxed without O_6 rotations. The data lines with c/a=1.27 represent the equilibrium lattice parameters for material BZT.

	c/a	a	c	Vol.	E_g(a)	E_g(b)	$\Delta E_g^{\mathrm{a-b}}$
BZT	1.30	3.82	4.97	72.66	1.93	1.04	0.89
	1.27	3.82	4.86	70.92	1.88	1.09	0.79
	1.24	3.82	4.74	69.12	1.81	1.18	0.63
	1.06	3.82	4.05	59.09	1.18	1.27	-0.09
	1.30	3.74	4.86	68.12	1.97	1.11	0.86
	1.27	3.82	4.86	70.92	1.88	1.09	0.79
	1.24	3.92	4.86	74.66	1.66	1.03	0.63
	1.06	4.58	4.86	102.16	0.31	0.52	-0.21
BMT	1.27	3.82	4.86	70.92	1.76	1.42	0.34
BZZ	1.27	3.82	4.86	70.92	1.66	0.45	1.21
PGN	1.27	3.82	4.86	70.92	2.47	2.52	-0.05
PSN	1.27	3.82	4.86	70.92	2.28	2.42	-0.14
PAN	1.27	3.82	4.86	70.92	2.55	2.61	-0.06
PZM	1.27	3.82	4.86	70.92	1.61	metal	$\geq$1.61

6.3.3 cation identity effect

The energy ordering of the d orbitals is crucial for the band gap engineering mechanism; we demonstrate this by studying substitution of different A- and B-cations. To isolate the effect of the cation identity, we use the equilibrium lattice constants from constrained BZT arrangements a and b. We first replace the Zn^{2+} ions by Mg^{2+}. In $Bi(Mg_{1/2}Ti_{1/2})O_3$ (BMT), the change in Mg/Ti ordering has almost no impact on E_g, since Mg $2p$ orbitals are too far below the valence band maximum. On the other hand, for $Bi(Zn_{1/2}Zr_{1/2})O_3$ (BZZ), where Zr replaces Ti, the strong sensitivity of the E_g to the cation arrangement is preserved, as see from the data in Table 6.2. To examine the impact of the changes in cation arrangement on E_g for +3/+5 ($B/B^{'}$) $A(B_{1/2}B^{'}_{1/2})O_3$ perovskites, we substitute Pb for Bi on the A-site and Ga/Nb for Zn/Ti on the B-site. Despite the proximity of Ga to Zn in the periodic table, our calculations show small valence band level change for $Pb(Ga_{1/2}Nb_{1/2})O_3$ (PGN), because Ga $3d$ orbitals are too low to reach the valence band frontier and affect E_g. Similar results are found for $Pb(Al_{1/2}Nb_{1/2})O_3$ (PAN) and $Pb(Sc_{1/2}Nb_{1/2})O_3$ (PSN). In PAN, there are no d orbitals in the underbonded all-Al plane; in PSN, the Sc $3d$ orbitals are too high in energy and are located above the conduction band edge.

For PGN, PAN and PSN at BZT lattice constants, the extreme tetragonality has a two-fold impact on the conduction band. First, the conduction band minimum is mainly composed of Pb $6p$ orbitals, similar to the case of three Bi-based materials

we discussed earlier. Second, we find that the B-site d^0 transition metal states (Nb 4d) are shifted down by the change from B-cation arrangement a to b. Nb 4d states redistribute due to different B-cation orderings, however, it does not alter the E_g value since the conduction band minimum is set by the energy of Pb 6p orbitals. The crystal field theory framework is helpful in understanding the mechanism for Nb 4d states shift due to B-cation ordering in the conduction band. The higher than average bond order of the Nb-O bonds in the all-Nb plane leads to a decrease in Pb-O bonding for the O atoms bonded to two Nb cations. Such a charge transfer out of the Pb-O bond and into the Nb-O bond decreases the electrostatic repulsion between the electrons in the Pb-O bonds and the Nb d states. This shifts the Nb d states down in energy, especially Nb 4d_{xy}.

In order to engineer the combination of the valence and the conduction band by B-cation arrangement, we pick $Pb(Zn_{1/2}Mo_{1/2})O_3$ (PZM) to study. The higher electronegativity of Mo^{6+} (relative to Nb^{5+}) makes Mo 4d located at the conduction band minimum instead of Pb 6p, so that the change in the cation arrangement from a to b lowers the energy of the conduction band (Mo 4d) while raising the valence band level (Zn 3d). Our LDA+U calculations show that PZM arrangement a is an insulator with E_g=1.6 eV, while PZM arrangement b is metallic. We estimated $\Delta E_g^{\mathrm{a-b}}$ to be as large as 2 eV.

Figure 6.7: Band dispersion for BZW B-cation arrangement a$'$ with constrained (without O_6 rotations, top) and relaxed structures (bottom) near the fermi level.

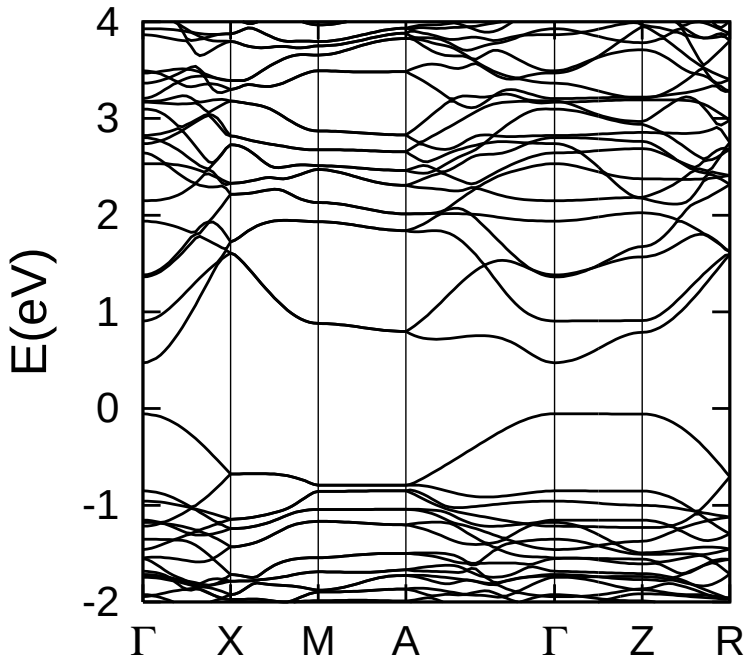
4
3
2
1
0
-1
-2
E(eV)
Γ
X
M
A
Γ
Z
R

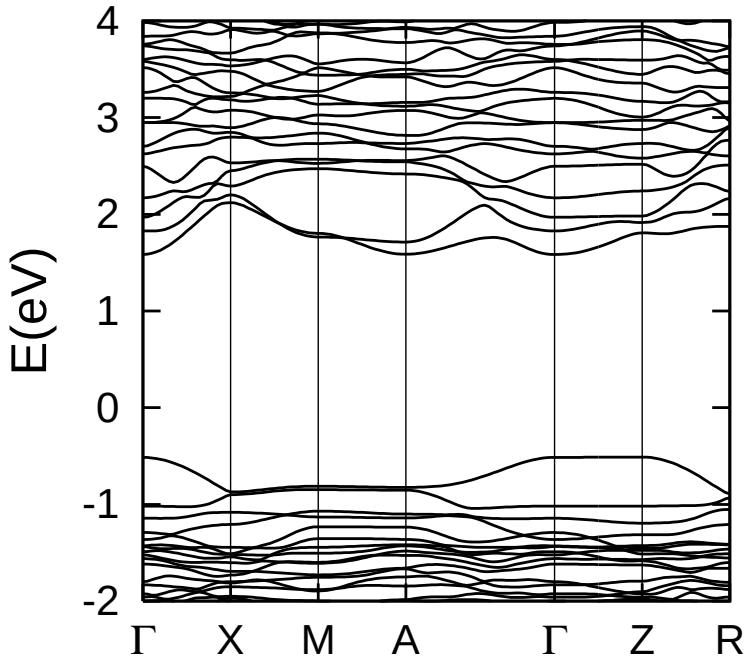
4
3
2
1
0
-1
-2
E(eV)
Γ
X
M
A
Γ
Z
R

Table 6.3: All BZW and BZM supercells relax into orthorhombic symmetry. The two short lattice vectors are within 5% difference in magnitude. We take the average of the two for caculating approximate tetragonality c/a. DFT energies (eV/5-atom cell), tetragonality, polarization (C/m^2) $\hat{z}$ component and total magnitude, E_g (eV, LDA+U), and averaged O_6 tilting angles ($^\circ$) are presented for the constrained without O_6 rotations (set I) structures and the fully relaxed (set II) structures. The subscripts i and d indicate indirect and direct E_g.

	E_{DFT}	c/a	P_z	P_{tot}	E_g	transition	O_6 tilt
BZW	(set I)						
a′	0.259	1.197	0.96	0.96	0.53_d	$\Gamma \rightarrow \Gamma$	0.0
b′	0.301	1.287	1.30	1.30	0.82_d	$\Gamma \rightarrow \Gamma$	0.0
c′	0.101	1.323	1.51	1.51	1.74_i	Γ/Z$\rightarrow \Gamma$	0.0
d′	0.107	1.248	1.28	1.28	1.77_i	Γ/X$\rightarrow \Gamma$	0.0
e′	0.309	1.211	0.97	0.97	1.33_d	$\Gamma \rightarrow \Gamma$	0.0
BZM	(set I)						
a′	0.332	1.248	1.00	1.00	0.33_d	$\Gamma \rightarrow \Gamma$	0.0
b′	0.299	1.326	1.17	1.17	0.53_d	$\Gamma \rightarrow \Gamma$	0.0
c′	0.101	1.329	1.56	1.56	1.72_i	Γ/Z$\rightarrow$M/A	0.0
d′	0.147	1.304	1.36	1.36	1.62_i	$\Gamma \rightarrow$A	0.0
e′	0.333	1.321	1.16	1.16	1.43_i	Γ/X$\rightarrow \Gamma$	0.0

	E_{DFT}	c/a	P_z	P_{tot}	E_g	transition	O_6 tilt
BZW	(set II)						
a′	0.064	1.219	0.92	0.98	2.12_i	Z→A	5.6
b′	0.066	1.203	0.88	1.01	2.25_i	Γ → Γ	5.3
c′	0.000	1.285	1.07	1.07	2.18_i	M→ Γ	5.0
d′	0.038	1.233	1.20	1.20	2.33_i	X/M→ Γ	4.7
e′	0.021	1.080	0.58	0.68	2.31_i	R→ Γ	12.8
BZM	(set II)						
a′	0.102	1.195	0.67	0.84	2.18_i	Z→Z/R	8.0
b′	0.090	1.230	0.91	1.03	2.22_d	Γ → Γ	5.3
c′	0.000	1.316	1.45	1.45	2.13_i	M→A	3.9
d′	0.038	1.283	1.27	1.34	2.11_i	X→M	3.5
e′	0.188	1.297	1.16	1.21	2.04_i	Γ →A	6.0

6.3.4 oxygen cage tilt effect

The band gap of extremely tetragonal materials is highly sensitive to the tilting of the O_6 octahedra. To determine the effect of the O_6 tilt, we compare the E_g values of fully relaxed and constrained supercells for BZT, BZW and BZM. The effect of tilting is even more pronounced for BZW and BZM than for BZT. Here, the constrained structures without O_6 rotations exhibit low E_g values ($\approx$ 0.5-1.5 eV) with extremely high c/a and P. Between the arrangements containing all-Zn xy planes and the other arrangements, the band gap difference is around 1 eV. However, the E_g values of fully relaxed BZW and BZM supercells vary around 2.2 eV (Table 6.3), with almost the same E_g values for different B-cation arrangements.

A comparison of the band structures for the constrained and the fully relaxed geometries of BZW arrangement a$'$ (Fig. 6.1 and Figure 6.7) shows that suppressing O_6 rotations increases the bandwidth for both the valence band and the conduction band, decreasing E_g. Our results suggest that the E_g can be significantly lowered by suppression of the O_6 rotations, which is in agreement with the experimental observations on alkali tantalate materials $LiTaO_3$, $NaTaO_3$ and $KTaO_3$. For these materials, distortions in the Ta-O-Ta bond angles (37°, 17° and 0°, respectively) track with the band gap (4.7 eV, 4.0 eV and 3.6 eV, respectively) [75].

6.3.5 E field tunable E_g and effective mass

In addition to the E_g engineering via local chemistry, the extremely high tetragonality in Bi-based perovskites leads to unusual carrier mobility. For example, we find a strong dispersion at the conduction band in BZT arrangements a and b. The calculated electron effective mass tensors are 0.3-0.5 m_e for all three Cartesian directions. This is comparable to the effective mass for the classic semiconductors (Si, Ge and GaAs), and much smaller than the electron effective mass usually found for the conduction band of perovskites (*e.g.*, $BaTiO_3$ longitudinal and transverse electron effective masses are 3-4 m_e and 1.1-1.3 m_0 [7]). The effective mass is an important parameter predicting charge carrier mobility, and low carrier mobility is one of the obstacles to the use of ferroelectrics for efficient solar energy conversion. A low electron effective mass along the polarization direction in BZT therefore indicates significantly improved electron mobility over the current perovskite ferroelectrics.

Unlike the electron effective mass, the hole effective mass tensor in BZT displays strong anisotropy. For arrangement a, the longitudinal hole effective mass is 25.3 m_e, and the transverse hole effective mass is 1.9 m_e. The anisotropy is even stronger in arrangement b. While its transverse hole effective mass is 0.8 m_e, the longitudinal hole effective mass is essentially infinity. The extremely large $\hat{z}$ direction hole effective masses are easily understood, since the large c lattice parameter ($\approx$ 4.5 Å, GGA) makes the structure almost 2D layered, such that all-Zn planes are isolated from their

$\hat{z}$ direction neighbors. Hence, the orbital overlap is significantly reduced. It impedes hole transfer along the polarization direction, forming a 2D hole gas (2DHG). This has previously been found for a number of interfacial semiconductor systems [133, 89]. However, to our knowledge, BZT is the first example of a 2DHG in a single-phase bulk material.

6.4 Conclusion

In summary, our first-principles calculations suggest several key factors for band structure engineering of highly tetragonal FE perovskites to make these materials suitable for visible sunlight absorption in solar energy applications. A combination of extreme tetragonality and all-Zn planes stacked perpendicular to the polar axis can significantly raise the energy of the valence band in ABO_3 perovskites, decreasing E_g compared with other B-cation arrangements. Increased valence and conduction bandwidths are favored by smaller octahedral tilting. Lower conduction band energies can be induced by incorporating B cations with higher electronegativity. Design of extremely tetragonal materials with specially layered B-cations and suppressed oxygen octahedral rotation is a promising direction for the development of new low-E_g highly polar FE semiconductors. Now, we have covered three chapters for DFT oriented calculations studying perovskite ferroelectrics. For the next Chapter 7 and Chapter 8, I am going to present more MD oriented studies on dynamics.

Chapter 7

Collective coherent control: Synchronization of polarization in ferroelectric $PbTiO_3$ by shaped THz fields

7.1 Introduction

Coherent optical control over ultrafast molecular behavior including chemical reactions has been explored in recent years [91], spurred by the application of optimal control theory and related methods [107, 80] and by the development of femtosecond pulse shaping techniques [127, 129, 20] through which complex optical waveforms have been crafted and optimized to induce specified molecular responses. Here, we propose and model theoretically the extension of coherent control to collective structural change. We show through numerical simulations that temporally shaped terahertz (THz) fields can be used to induce ferroelectric domain switching with extensive control over the collective microscopic pathway from initial to final structure, in a coherent process that is very different from the conventional stepwise switching mechanism [124].

Perovskite ferroelectric crystals have simple collective lattice vibrational modes that describe the microscopic pathways along which structural change occurs [see Fig. 7.1]. For this reason, these crystals are prototypes for the study of collective structural rearrangements, with many modelling studies interrogating both static and dynamic aspects of their phase transitions [98, 113]. A particularly important aspect is domain switching, the process of reorienting part or all of a domain so that its macroscopic polarization points in a different direction. We and others [32, 81, 92, 112, 19] have sought to illuminate how microscopic interatomic interactions affect

the rate and mechanism of ferroelectric domain switching.

Figure 7.1: (a) PTO unit cell in the tetragonal ferroelectric phase, with a +z domain orientation. The soft vibrational mode is indicated by the arrows on the ions. (b) Time-dependent lattice response to a single asymmetric THz pulse (shown in blue) with its large lobe polarized along the -z direction, i.e. "anti-parallel" to the static ferroelectric polarization. The z-component P_z (shown in green) oscillates about its static nonzero value as the Ti and other ions oscillate about their lattice positions in the +z domain. No significant responses of the other components P_x and P_y (shown in black and red respectively) about their static values of zero are induced.

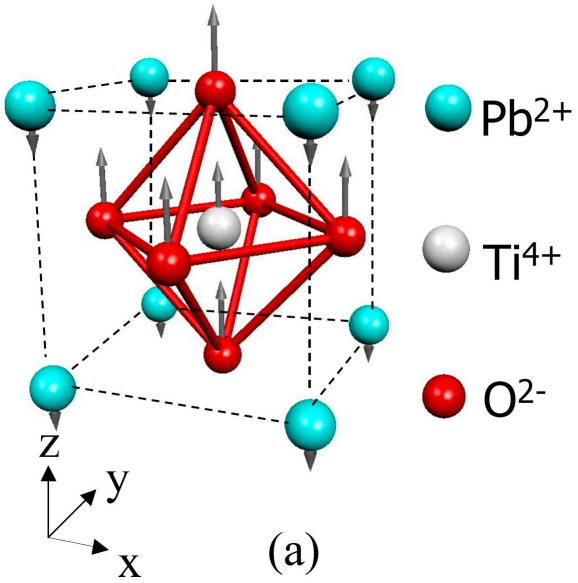
Pb2+
Ti4+
O2-
z
y
x

(a)

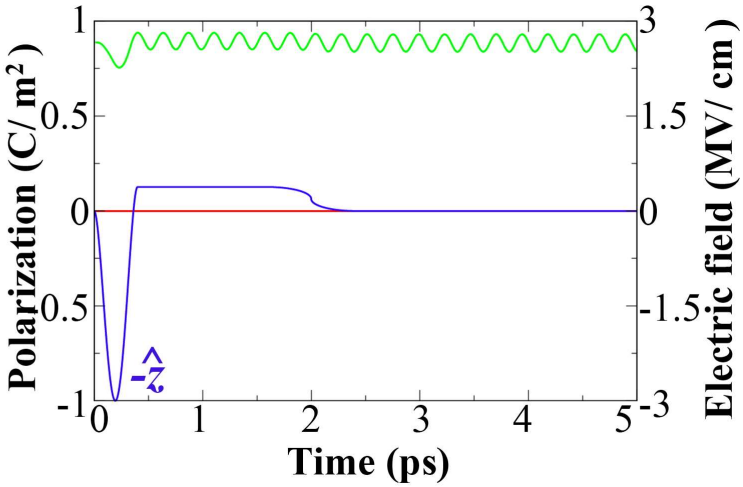
Polarization (C/ m2)
Electric field (MV/ cm)
Time (ps)
-ẑ
1
0.5
0
0.5
-1
3
1.5
0
-1.5
-3
0
1
2
3
4
5

(b)

In the tetragonal phase of lead titanate ($PbTiO_3$, PTO), the crystal has two domain orientations characterized by opposite polarization directions along the tetragonal axis with symmetrically equivalent ground states separated by an energy barrier. The polarization direction can be reversed under an electric field. This is exploited extensively in ferroelectric memory devices, so the dynamics of domain switching have been of technological as well as fundamental interest. There is great experimental interest in rapid ferroelectric polarization switching under strong electric fields, with most experimental approaches limited to the thin film regime [124, 47, 38, 82, 83]. Most studies of polarization reversal focus on domain wall properties and dynamics under the influence of an electric field that is applied through electrodes at the sample surfaces [112, 69, 123]. Earlier attempts to control crystalline soft modes and phase transitions through impulsive stimulated Raman scattering used nonresonant optical pulses without tailored pulse profiles [134, 39, 90] and were based on simple models for the impulsively driven lattice vibrations and the crystalline responses to them; so far such attempts have failed to find experimental validation because the high light intensities needed to reach sufficient vibrational amplitudes far exceed typical material damage thresholds.

In contrast, here we explore the fundamental limit of the polarization switching time of ferroelectric PTO under the coherent control of a terahertz-frequency electromagnetic driving field that permeates the sample and is resonant with its soft

mode frequency. Using a well validated atomic potential model of PTO [112, 111], we consider the coherent reorientation of a large region, without domain wall formation or movement, and we consider a terahertz-frequency driving field with tailored amplitude, phase, and polarization profiles, motivated by recent progress in the generation of large-amplitude shaped terahertz fields and in the observation of anharmonic responses of ferroelectric soft modes to them [56]. We examine the possibility of coherent control over domain reversal to "read" or "write" bulk ferroelectric data storage media on picosecond time scales.

7.2 Methodology

We carried out molecular dynamics (MD) simulations of PTO with a $6 \times 6 \times 6$ supercell using a classical potential formulated and parameterized [111] to reproduce the energies and all atomic forces encountered in Car-Parrinello simulations for a large set of thermally accessed structures. The interatomic potential consists of four parts: a term with the bond-valence [21] potential energy form (but modified numerical constants), a Coulomb potential energy term with modified charges, a r^{-12} repulsion term, and a harmonic term to reduce the angle tilts of octahedral cages. This potential [111] reproduces the ferroelectric behavior of PTO accurately without being fit to any experimental observations. MD simulations show a ferroelectric transition at 575 K with a mixed order-disorder and displacive phase transition character [113].

Important results have been achieved with this model, including identification of the nucleation and growth mechanism of the 180° domain wall of PTO under an external electric field [112] and correlations between the structure and the dielectric properties of Pb-based relaxor ferroelectrics [68].

To simulate THz experiments, we set the tetragonal lattice constants to the experimental values ($a = 3.9$ Å, $b = 4.15$ Å) and one or more electric field pulses were applied to the system. All the pulses we used had an asymmetric electric field profile with a large-amplitude lobe of short duration (a full width at half maximum of $\approx$ 150 fs, to include frequency components up to about 6.6 THz) and a lower-amplitude lobe of longer duration in the opposite polarity. The electric field integrates to zero as required for optical pulses [Fig. 7.1b]. The asymmetric field profile is well suited for driving nonlinear responses in the direction of the large-amplitude lobe. Even shorter pulses could also drive polarization oscillations similar to the pulses we chose. However, to flip polarization with the same number of shorter pulses, much higher electric field amplitude is required, which is very challenging to generate and could lead to material damage.

7.3 Results and Discussion

To switch the polarization from $+\hat{z}$ to -$\hat{z}$, the most direct way is to apply electric field pulses along -$\hat{z}$. Fig. 7.1b shows that applying a -$\hat{z}$-oriented electric field pulse

causes the z component of the polarization (P_z) to oscillate in time about its nonzero static value. The other polarization components (P_x and P_y) remain essentially zero. The oscillation period of about 240 fs, which corresponds to 4.2 THz, is independent of pulse magnitude, indicating an essentially harmonic mode (the Pb-O or so-called Last mode) at these amplitudes. The phonon frequency is in good agreement with DFT calculations and the experimental value [40] of 4.5 THz.

In order to reorient the lattice polarization, the coherent vibrational amplitude must be made large enough to overcome the potential energy barrier between the two stable polarization states. The P_z vibrational coherence could be reduced or enhanced by successive pulses depending on their timing. As shown in Fig. 7.2a, polarization reversal can be achieved within 15 ps with seven pulses of amplitude 3 MV/cm. In order to suppress coherent return of the polarization to its original direction and multiple successive domain flipping events, we applied one additional -$\hat{z}$-oriented pulse out of phase with the P_z oscillations. This guaranteed that after the system acquires sufficient energy to cross the barrier freely, we can then trap it in the desired polarization state. At 0 K, one out-of-phase pulse reliably leaves the domain completely flipped. It is also important to note that the out-of-phase pulse cools down the system substantially ($\approx$ 95 K), since much of the energy is in the coherent mode after the first six pulses. In order to avoid excessive heating of the system, such an out-of-phase pulse could be useful not only at 0 K but also at finite

temperature.

Figure 7.2: Collective coherent control over ferroelectric polarization with shaped terahertz waveforms. (a) Sequence of seven asymmetric THz pulses (in blue), all z-polarized with large lobes (3 MV/cm) along the -$\hat{z}$ direction. Each successive pulse makes the polarization (P_z in green) oscillation amplitude bigger than the previous by driving the soft mode in-phase with the oscillation already present. The time interval between pulses is an integer number of soft mode periods which gradually grow longer due to anharmonicity. (b) Lattice potential energy surface (PES) with respect to P_x and P_z, calculated using our MD model. A PES local maximum appears at the high-symmetry cubic structure with $P_x = P_z = 0$. The z-polarized THz field in (a) drives the system over this potential energy barrier. Domain switching can occur with lower energies along trajectories that pass through or near the saddle points in the PES. (c) Sequence of four THz pulses with $\hat{x}$-oriented fields followed by a final THz pulse with -$\hat{z}$-oriented field. (d) Power spectrum from Fourier transformation of P_x and P_z in (c). A strong peak stems from P_x oscillations at the 1.6 THz phonon frequency. The smaller peak shows the second harmonic frequency of oscillations in P_z.

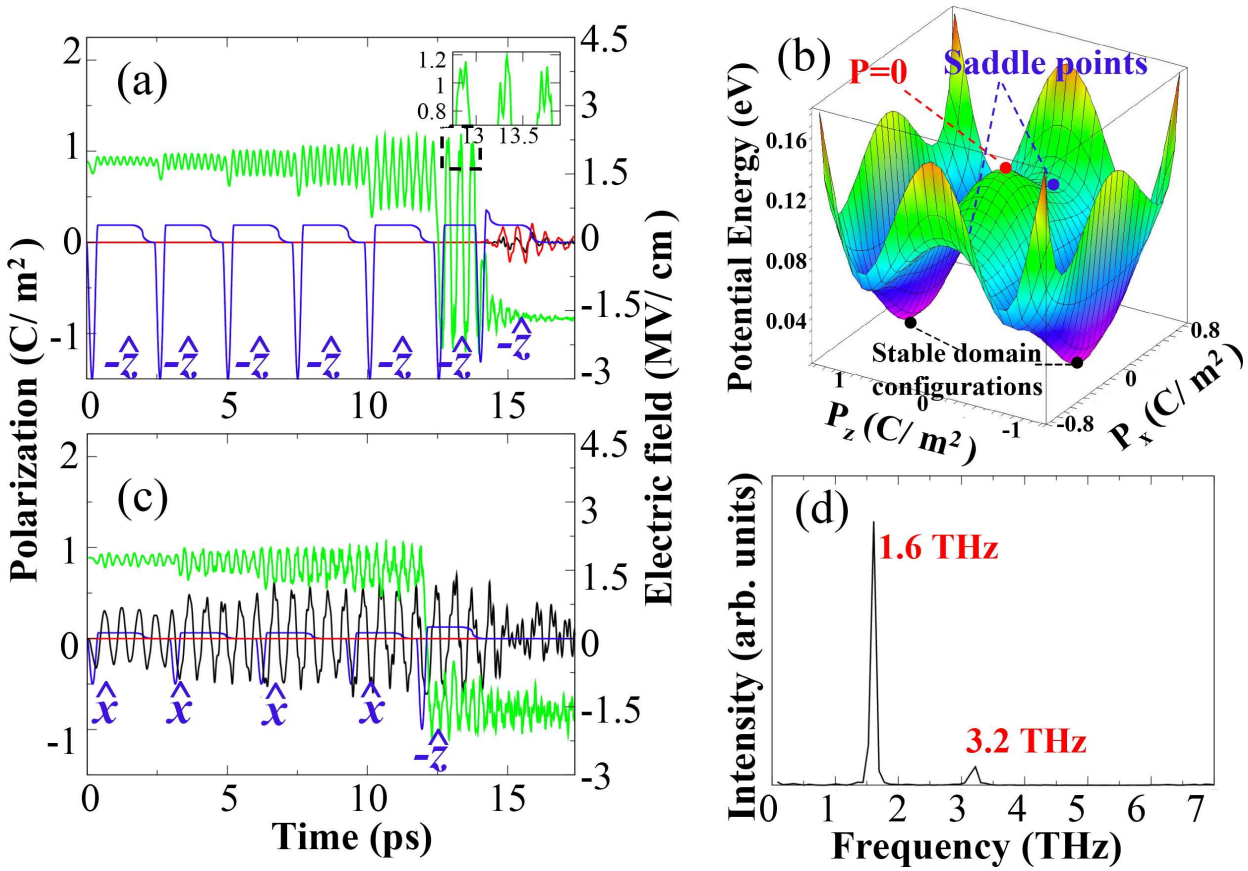
(a)
(b)
(c)
(d)
P=0
Saddle points
Stable domain configurations
1.6 THz
3.2 THz
Polarization (C/ m²)
Electric field (MV/ cm)
Time (ps)
Potential Energy (eV)
Intensity (arb. units)
Frequency (THz)
P_z (C/ m²)
P_x (C/ m²)

It is well known from the quasi-DC limit that polarization rotation offers lower-energy pathways to polarization flipping than directly surmounting the local potential energy maximum at the high-symmetry cubic lattice configuration. Atomistically, polarization rotation corresponds to a trajectory for Ti that goes around, rather than through, the unit cell center [43]. We therefore investigated prospects for maintaining soft mode vibrational coherence while undergoing trajectories of this sort. This alternative scheme involves significant ionic motions and lattice polarization components along the $\hat{x}$ and/or $\hat{y}$ directions as well as $\hat{z}$, and therefore it involves exploration of much more of the three-dimensional lattice potential energy surface (PES). Fig. 7.2b shows the lattice potential energy obtained from our MD model as a function of P_z and P_x. The energies required to reach the high-symmetry PES local maximum and a saddle point (ΔE_z and ΔE_x respectively) are compared in Table 7.1. The saddle point energy is about 20% lower, offering lower-energy switching trajectories than those that pass through the PES maximum.

Table 7.1: Comparison of potential energy local maximum ΔE_z vs. saddle point ΔE_x for polarization switching in PTO

	DFT	our MD model
ΔE_z (eV/unit cell)	0.168	0.143
ΔE_x (eV/unit cell)	0.136	0.110
$\Delta E_x/\Delta E_z$	0.81	0.77

In order to explore coherent control of domain switching with trajectories that go around the PES maximum, we conducted MD simulations with sequences of $\hat{x}$- and $\hat{z}$-polarized asymmetric terahertz pulses rather than all $\hat{z}$-polarized pulses as described earlier. Fig. 7.2c shows an example with four $\hat{x}$-polarized pulses (with large lobes of amplitude 1 MV/cm along $+\hat{x}$) followed by one $\hat{z}$-polarized pulse (with a large lobe of amplitude 2 MV/cm along -$\hat{z}$). After a single $\hat{x}$-oriented pulse, the simulation shows that both P_x and P_z oscillations were excited, corresponding to polarization rotation in the $\hat{x}\hat{z}$ plane. The power spectrum in Fig. 7.2d shows that the frequency for P_z oscillation was twice that of P_x (1.6 THz), which is a consequence of the lattice symmetry about the $x = 0$ plane. The curvature of the PES draws the z-component of the polarization toward smaller values when the x-component undergoes an excursion toward positive or (symmetry-equivalent) negative values. For example, the Ti ion moves toward the $z = 0$ plane when it is displaced in either direction from the $x = 0$ plane. Thus each half-cycle of P_x corresponds to a full cycle of P_z. The oscillation amplitude of P_z depends quadratically on that of P_x until highly anharmonic regimes are reached, and the P_z response would give rise to z-polarized frequency-doubling of x-polarized incident THz radiation.

The simulation results in Fig. 7.2c show that each successive x-polarized pulse increases the lattice polarization rotation amplitude, as each time P_x reaches a maximum excursion away from zero, P_z reaches a maximum excursion away from its initial

nonzero value toward a smaller value. After the fourth $\hat{x}$-oriented pulse, P_x exceeds P_z at the extrema of oscillation, which means that the polarization is rotating more than 45° and approaching the saddle point of the PES. Finally, a -$\hat{z}$-oriented pulse is applied to push the system over the saddle point. This approach (Fig. 7.2c) switches the ferroelectric domain more efficiently than the former method (Fig. 7.2a), in terms of the number of pulses, their peak magnitudes, and their integrated energy. The result illustrates the value of shaping the polarization as well as the amplitude and phase profiles of the terahertz control field. Polarization shaping has proved valuable in some examples of molecular coherent control with visible light fields [56].

Maintaining coherence at finite temperature is more challenging than at 0 K, because the increase in random fluctuations makes the final state more difficult to predict. The increased temperature changes several key factors that affect the switching process. First, coherence is lost more rapidly due to faster energy dissipation and pure dephasing. Second, the ferroelectric well depth decreases with higher temperature, as the higher entropy of the paraelectric state makes its free energy more competitive with that of the ferroelectric state. These two effects compete, with the first inhibiting coherence and the second facilitating domain flipping.

To guide our understanding of finite temperature domain switching, we concentrate on the response of the domain to a single -$\hat{z}$-oriented pulse. For a single pulse to reorient the polarization, the pulse strength should be sufficient for the system

to visit the potential energy minimum of the opposite polarization, yet not strong enough for the polarization to flip back. Shorter dissipation times can help to remove the excess energy from the soft mode by coupling the polarization with other modes. Our findings are summarized in Fig. 7.3. Due to thermal fluctuations, the same initial conditions can yield different results, with flipping success being a probabilistic event. We chose four different initial sample temperatures (50, 100, 200 and 300 K) to analyze statistically. For each temperature, we traced 250 trajectories starting from different equilibrated states irradiated by a single -$\hat{z}$-oriented pulse. To avoid excessive heating of the material, we limited the amplitude of the short duration electric field lobe. In Fig. 7.3, the circles indicate the probability that the system climbs over the PES barrier before damping reduces the energy in the coherent mode to below the barrier height (flip), and diamonds indicate the probability that it crosses back to the original domain orientation (flipback). Hence, the difference between these two datasets is the probability of exactly one flip reversing a domain. Eq. 7.1 fits the simulation results well (the fitting parameters are presented in Table 7.2):

$$\mathcal{P}(\mathcal{E}, \mathcal{T}, \backslash) = \frac{\infty}{\in} + \frac{\infty}{\in} \tanh\left(\alpha[\frac{\mathcal{E}}{\mathcal{E}_\prime} - \infty]\right) \tag{7.1}$$

where α and E_0 depend on temperature (T) and n. The E_0 values for both "flip" ($n = 1$) and "flipback" ($n = 2$) decrease monotonically with T. $E_0(T, 1)$ closely tracks the T-dependent free energy barrier, while $E_0(T, 2)$ is higher than $E_0(T, 1)$ because

of damping within one half period. This effect nearly doubles the range of field amplitudes over which single flipping is achieved as T is raised from 50 K to 300 K. The trends from MD simulations illustrate well the competing effects introduced by temperature. We find that the required minimum magnitude of the pulse decreases as the temperature increases because of the decreasing ferroelectric double well depth. Meanwhile, the range of pulse magnitudes that achieve "flip" without "flipback" is larger at higher temperatures because of increased dissipation.

Figure 7.3: The probability of at least a single "flip" or at least two flips (denoted "flipback") of polarization in response to a single -$\hat{z}$-oriented pulse with varied peak field amplitudes at different temperatures. At higher temperatures, lower field amplitudes are sufficient to flip the domain, while stronger dissipation in the new domain suppresses flipback for a wider range of field amplitudes.

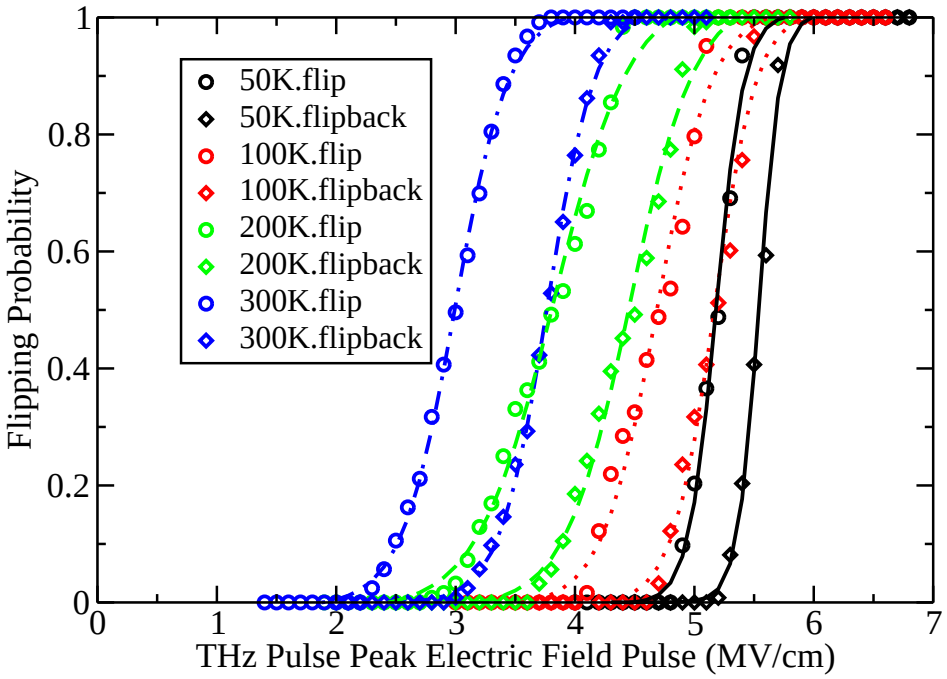
50K.flip
50K.flipback
100K.flip
100K.flipback
200K.flip
200K.flipback
300K.flip
300K.flipback
Flipping Probability
THz Pulse Peak Electric Field Pulse (MV/cm)
0
0.2
0.4
0.6
0.8
1
0
1
2
3
4
5
6
7

Table 7.2: Fitting parameters of flipping probabilities at different finite temperatures according to Eq. 7.1. Temperature is in Kelvin, α is unitless, and field E_0 is in MV/cm.

Temp.	$\alpha(T,1)$	$\alpha(T,2)$	$E_0(T,1)$	$E_0(T,2)$	$E_0(T,2) - E_0(T,1)$
50	22.43	30.75	5.18	5.54	0.36
100	11.25	16.03	4.68	5.16	0.48
200	8.32	11.39	3.78	4.43	0.65
300	6.64	9.51	2.99	3.76	0.77

7.4 Conclusion

Through MD simulations, we have demonstrated that collective coherent control over ferroelectric domain orientation should be possible through the use of shaped THz pulse sequences. Our results show that shaping of all aspects of the THz fields – the amplitude, phase, and polarization profiles – can contribute substantially to coherent control over collective material dynamics and structure.

Chapter 8

Molecular dynamics study of ferroelectric 90° domain wall properties and mechanism in $PbTiO_3$

8.1 Introduction

Ferroelectric materials exhibit domains over which the atom displacements lead to a net dipole polarization in one direction alternating with domains with the polarization in another direction. For those materials in tetragonal phase, the polarization could be switched by 180° or 90° applying external electrical field or mechanical stress. It leads to broad applications such as non-volatile ferroelectric random access memories (NFERAMs), actuators, sensors and transducers. Although ferroelectrics have been studied quite intensively, microscopic explanation of how the walls form and move is poor and even domain wall width is still puzzling especially for the case of 90° domain walls.

A phenomenological level of description has been used in many previous theoretical works, such as phase-field model [136, 5, 27], finite element model [62] and Ginzburg-Landau-Devonshire theory based model [58]. They provide alternatives for significantly larger systems. The model parameters required to describe individual systems are crucial. The shortcoming is that it depends largely on how accurate the experimental observations are. First-principles calculation is also a powerful approach on the other hand. Many predictions have been made and confirmed. 90° $PbTiO_3$ domain walls width was predicted to be on the order of one or two lattice constants [86, 99, 92], matching the state of the art atomic force microscopy results [108]. Moreover, *ab initio* studies on sheer stress-induced 90° domain switching [109] reveals

that the Pb-O bond reconstruction associating with the domain migration. However, the *ab initio* calculations' heavy computational load is well known. Hence, effective Hamiltonian model, shell model [77, 78, 110], bond-valence model [111, 112] and others derived from DFT extend the applicable range of atomic-level simulations.

Recent X-ray diffraction experiment performed by Vlooswijk *et al.* revealed the narrowest (6-7 nm) possible a domain as well as the shortest $c|a|c$ domain periodicity (27-31 nm). The small periodicity makes it potentially promising for ferroelectric memories. Inspired by their work, we set our goal to providing unprecedented detailed atomistic features of the 90° domain wall forming dynamics induced by external mechanical stress in bulk $PbTiO_3$, focusing on studying the microscopic pictures of the creation of new domain wall pairs and their separation giving rise to a new domain. It provides us with a better understanding about macroscopic control of the spontaneous polarization and the piezoelectric responses, which are closely related to the domain wall kinetics.

Figure 8.1: A stable zigzag domain pattern forms under strain at 0 K. Pb, Ti and O are color coded. Big arrows indicate the domain polarization directions. Dashed lines indicate the domain wall location.

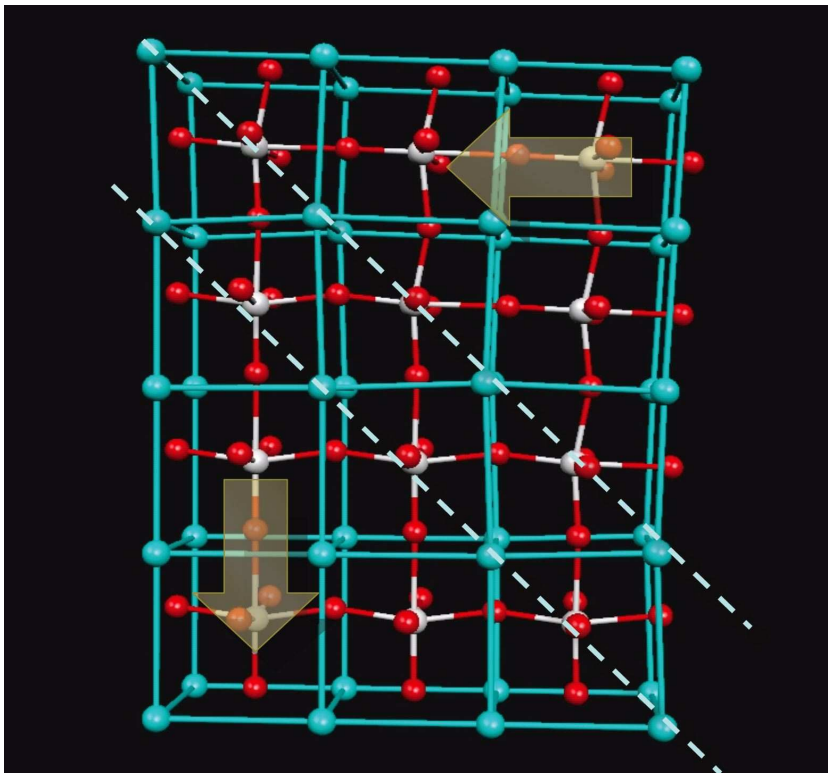

8.2 Methodology

We carried out molecular dynamics (MD) simulations of PTO with a classical potential formulated and parameterized [111] to reproduce the energies and all atomic forces encountered in Car-Parrinello simulations for a large set of thermally accessed structures. The inter-atomic potential consists of four parts: a term with the bond-valence [21] potential energy form (but modified numerical constants), a Coulomb potential energy term with modified charges, a r^{-12} repulsion term, and a harmonic term to reduce the angle tilts of octahedral cages. This potential [111] reproduces the ferroelectric behavior of PTO accurately without being fit to any experimental observations. MD simulations show a ferroelectric transition at 575 K with a mixed order-disorder and displacive phase transition character [113]. Important results have been achieved with this model, including identification of the nucleation and growth mechanism of the 180° domain wall of PTO under an external electric field [112] and correlations between the structure and the dielectric properties of Pb-based relaxor ferroelectrics [68]. The contribution of each atom to the spontaneous polarization is computed as the product of the Born effective charge [71] tensors Z^* and the atomic displacement vector. The local polarization in each cell, $\vec{P}_l$, is defined as the average of the atomic polarization of one Ti atom, its eight nearest-neighbor Pb atoms and its six nearest-neighbor O atoms.

$$\vec{P}_l = \frac{1}{V_u}\left(\frac{1}{8}Z^*_{Pb}\sum_{i=1}^{8}\vec{r}_{Pb,i} + Z^*_{Ti}\vec{r}_{Ti,i} + \frac{1}{2}Z^*_{O}\sum_{i=1}^{6}\vec{r}_{O,i}\right) \tag{8.1}$$

Figure 8.2: We compare our result (in black) and the calculated domain wall angle from ref. [86] (in red). α is the angle between two polarization vectors in adjacent domains which are far away from the domain walls.

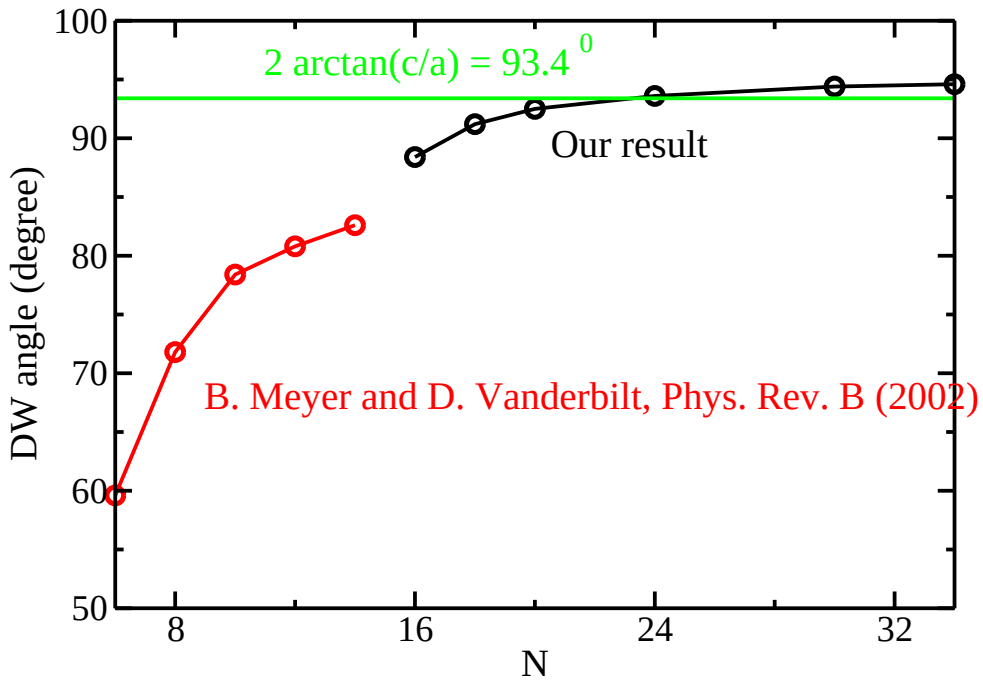
100
90
80
70
60
50
8
16
24
32
N
DW angle (degree)
2 arctan(c/a) = 93.4 0
Our result
B. Meyer and D. Vanderbilt, Phys. Rev. B (2002)

8.3 Results and Discussion

8.3.1 Static Properties

To guide our understanding of strain induced 90° domain wall evolution, we begin with *aca* supercells with all polarizations aligned in y. We simplified a 3D problem to a pseudo-2D one ($N \times N \times 2$). The volume as well as the z lattice constant are kept the same before and after the strain. Here, the unitless strain s is defined as the percentage of average c lattice constant change. When a compressive strain (larger than nucleation strain) is applied along y, lattices in x expand accordingly, some of the local polarizations rotate towards x forming 90° domain walls (denoted as $a|a$ wall), while the z component of polarizations of each unit cell is almost zero. Since the energy of the 90° domain wall is calculated to be about a factor of 4 lower than the energy of its 180° counterpart [86], we naturally only expect 90° domain patterns (Fig. 8.1).

Figure 8.3: Lattice constants across a 90° domain wall, calculated with a supercell of $30 \times 30 \times 2$ perovskite unit cells.

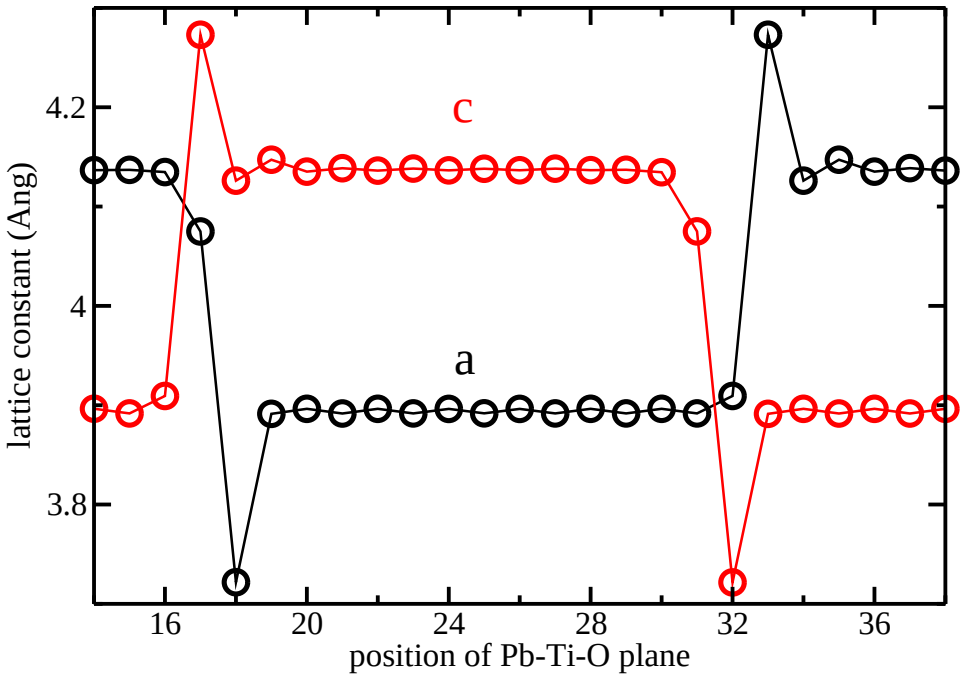
4.2
4
3.8
lattice constant (Ang)
c
a
16
20
24
28
32
36
position of Pb-Ti-O plane

Figure 8.4: Polarization profile across a 90° domain wall calculated within a supercell of 30 × 30 × 2 perovskite unit cells. $P_{\perp}$ and $P_{\parallel}$ represent the local polarizations perpendicular and parallel to the domain wall, calculated with a supercell of 30 × 30 × 2 perovskite unit cells.

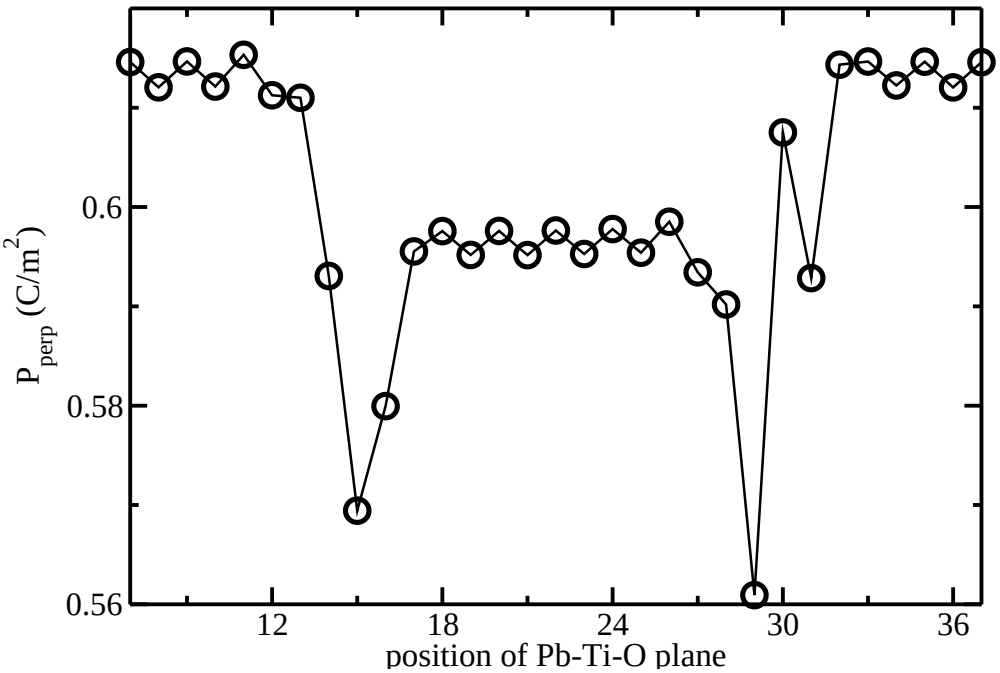
0.6
0.58
0.56
P_{perp} (C/m^2)
12
18
24
30
36
position of Pb-Ti-O plane

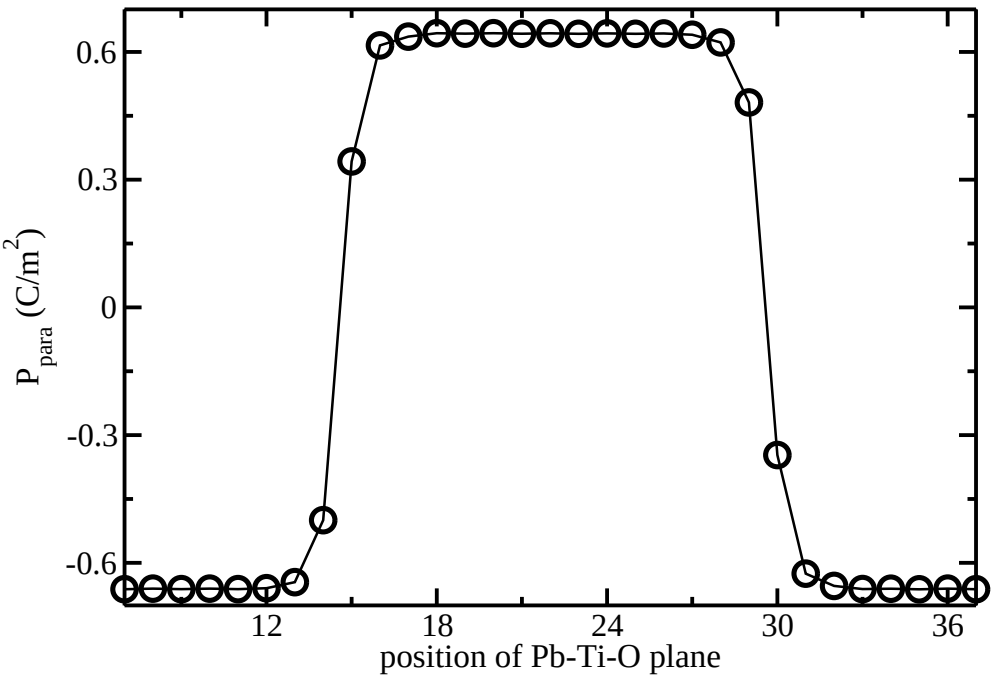
0.6
0.3
0
-0.3
-0.6
P_{para} (C/m^2)
12
18
24
30
36
position of Pb-Ti-O plane

Models based on continuum Landau-Ginzburg theory describe the domain wall as a soliton, predicting domain wall to be gradual rather than sudden. The domain wall energy can then be extracted from the order parameter across the wall. And the lattice constants across the wall are assumed to be symmetric [116]. However, we found both the unit cells' lattice constants and the local polarization vectors are asymmetric across the wall. The asymmetric polarization profile owing to the overshooting and undershooting of the lattice parameters was previously reported [137]. Although their PQEq force field method predicted a much wider domain wall width (21 nm), the qualitative lattice constant profile is the same as ours (Fig. 8.3). Instead of a geometrically interface with an angle of π-2arctan$(a/c) = 93.4°$, we found the crystal forms a slightly larger angle θ (Fig. 8.2). The angle mismatch was explained by Meyer and Vanderbilt [86] by the artificial electric field effects introduced by interacting dipole layers at the wall. However, as we increase the supercell size, there is an angle mismatch between our converged $\theta = 94.5°$ and continuum Landau-Ginzburg theory suggested $\theta = 93.4°$. We consider this as an indication of breaking domain wall's mirror symmetry. Rigorously, 90° domain wall is not a twin wall. As N approaches 30, θ converges. It also means that the interaction between two adjacent domain walls almost vanishes as their separation is larger than 85 Å.

In Fig. 8.4, the polarization component which is perpendicular to the wall ($P_\perp$) shrinks at the wall. It makes the domain wall effectively a dipole layer, or we can

think of a non-zero electric potential slope across the wall. Given the symmetry reduction at the wall, we predict that two driving force with the same magnitude but along antiparallel directions should move domain wall towards one and the other side differently. The effect is insignificantly small and might be difficult to observe, but it exists. Also, $P_{\perp}$ shows different magnitude in different domains, one is bigger than the other by 2.8 %. It is also interesting to note that $P_{\perp}$ is very sensitive to the unit cell location relative to the walls. The kinky curve especially at the unit cells close to the walls is a signature of asymmetric domain wall. The polarization component that is parallel to the wall ($P_{\parallel}$) shows the domain wall position approximately centered on O-O plane (Fig. 8.4). There're two layers of rapid polarization change at the domain wall and one layer of slow transition. The domain wall width is around 15 Å.

Figure 8.5: Snapshots of the polarization from a molecular dynamics simulation show a stepwise nucleation mechanism. The local polarization vectors are indicated by arrows, where the red colored arrows represent a larger polarization magnitude than the ones in green color.

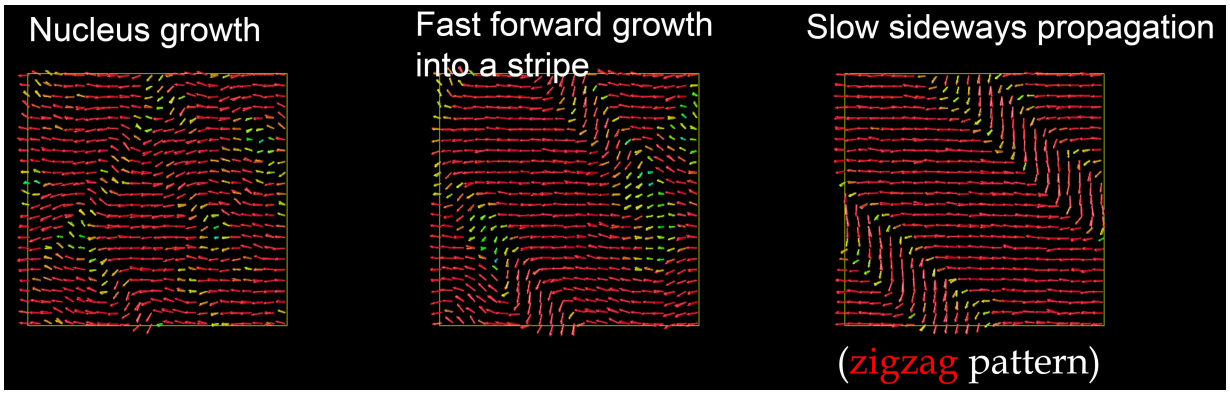
Nucleus growth
Fast forward growth into a stripe
Slow sideways propagation
(zigzag pattern)

8.3.2 Nucleation Dynamics

The domain growth mechanism is stepwise at finite temperature (Fig. 8.5). Some football-shape nuclei start to appear along (110), (-1-10), (1-10) and (-110) diagonal directions. However, the thermal fluctuation overcomes the nuclei that are too small sized. Only the big nuclei are able to survive. We characterize the critical nucleus size d by its 50 % surviving probability. We tested for temperatures within 25 K and 150 K, and found d is as small as around 3-5 unit cells per layer. Next, One or more nucleation sites grow rapidly along diagonal directions into continuous stripes. The stripes are sometimes parallel to each other and sometimes perpendicular so that they cross. They are equally probable, and the latter is obviously less energetically favorable than the former situation. Moreover, once such crosses are formed, thermal fluctuation is usually not strong enough to evolve the crosses into the other more energetically favorable periodically alternating zigzag pattern. The local polarization vectors in center of the cross region have a non-zero divergence, instead of a vortex like polarization vector distribution. Finally, the stripes grow sidewise wider forming stable domains separated by walls.

Figure 8.6: The probabilities of not emerging critical nucleus, four unit cells, at different final s train states of a $N \times N \times 2$ supercell starting from zero strain at 50 K.

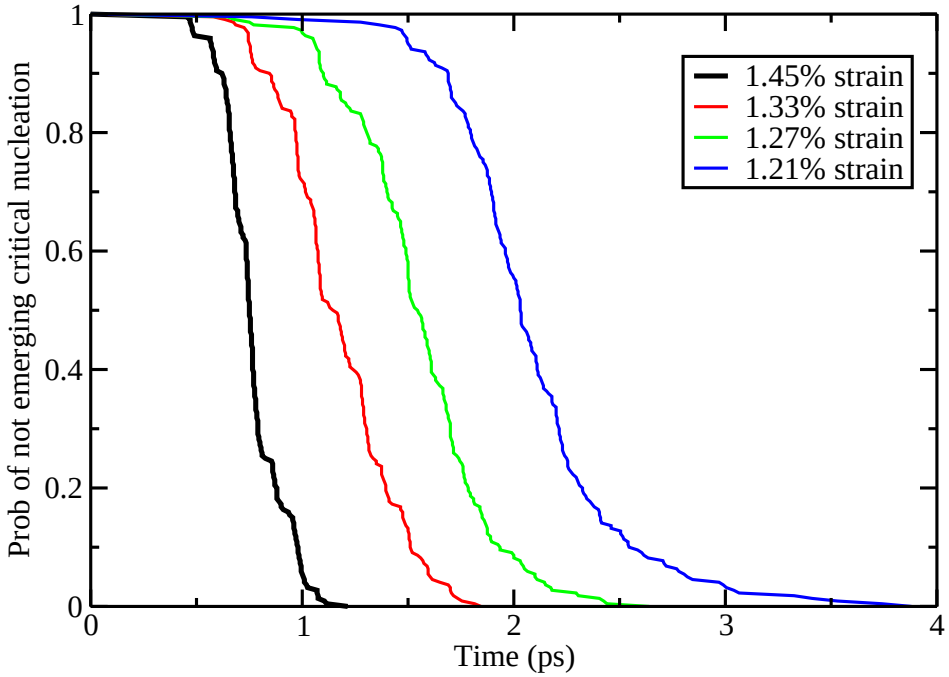
Prob of not emerging critical nucleation
Time (ps)
1.45% strain
1.33% strain
1.27% strain
1.21% strain
0
0.2
0.4
0.6
0.8
1
0
1
2
3
4

When a shock strain is applied, there is a certain time period before the system starts to respond. The stress is gradually relieved during the domain formation. Since the nucleation size is much smaller compared with the whole supercell size, we roughly count the stress driving force almost a constant during the nucleation process. To extract the nucleation rate J from the molecular dynamics data, we plot fraction of the simulation trajectories exhibiting no critical nucleation by time t versus time t (Fig. 8.6). The curve starts with a plateau followed by hypertangent decay. The nucleation rate J is calculated by taking the reciprocal of the probability curves' half decay time:

$$J(s,T) = \frac{1}{t_{half-decay}} \tag{8.2}$$

Figure 8.7: The nucleation rate J as a function of temperature and strain. J is in the unit of ps^{-1} per unit cell.

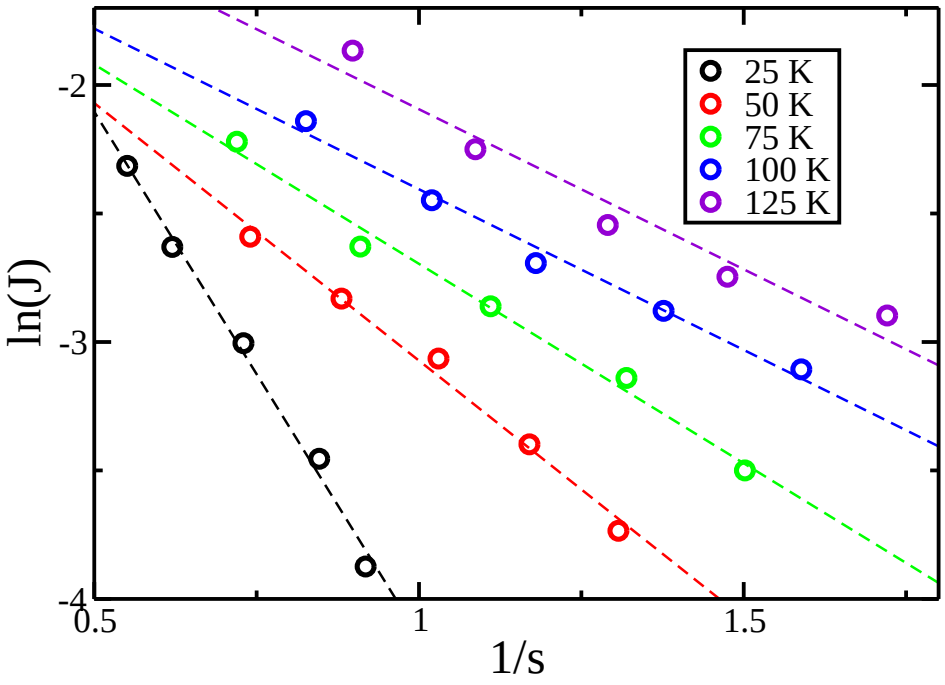
25 K
50 K
75 K
100 K
125 K
ln(J)
-2
-3
-4
0.5
1
1.5
1/s

At lower temperature, J converges quickly as size N reaches 30. The domain separation is large enough for domain-domain interactions to vanish. At higher temperature, the domain wall becomes more diffuse. As a result, larger N values is required for getting converged J values. For instance, N has to reach 38 for temperature 150 K. By calculating J under different strains and temperatures, we found a good linear relationship between $ln(J)$ and $1/s$. The dynamics seems to match the Merz's law:

$$ln(J) = -\frac{\sigma_{a,T}}{\sigma} = -\frac{\sigma_{a,T}}{Ks} \tag{8.3}$$

where $\sigma_{a,T}$, σ and s are activation stress, applied external stress and applied external strain respectively. K is the elastic force constant. Provided with J and s, we are able to get the activation stress $\sigma_{a,T}$. As N is sufficiently large, we observe a monotonically decreasing trend of $\sigma_{a,T}$ with respect to T, which implies an easier formation of 90° domain wall nucleus under a higher temperature.

However, the activation stress doesn't seem to converge with respect to N. The reason is as following. As we track a number of different trajectories starting from equilibrated configurations, sometimes there are more than one nucleation sites. The bigger the supercell is, the more the nucleation sites will appear. If we only track the first appearance of all the nucleation sites, we only count the fastest nucleation site. However, the Merz's law describes J as number of nucleation cells per second. The bigger N gets, the more the nucleation rate J is overestimated, which leads to an

underestimation of the activation stress. Therefore, we correct our results by counting the averaged appearance time of all nucleation sites instead.

Figure 8.8: The activation stress as a function of temperature.

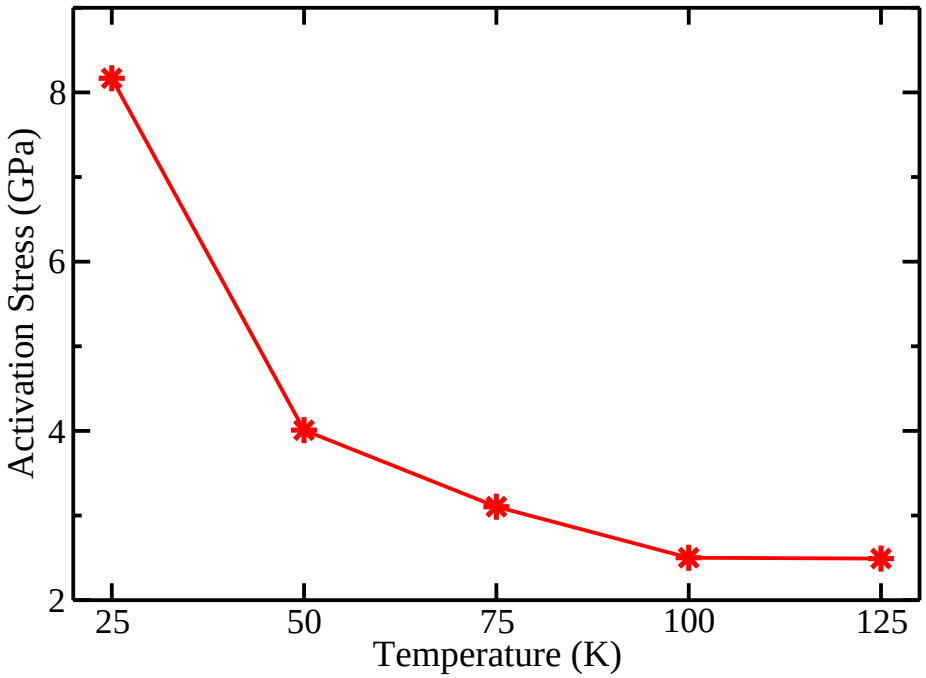
Activation Stress (GPa)
8
6
4
2
25
50
75
100
125
Temperature (K)

However, we did observe a slight decrease of the activation stress as we increase the value of N. It is possible that the activation stress already reaches convergence, the slight change in activation stress is due to the numerical fluctuation. In the meanwhile, it is also possible that the decrease of activation stress with respect to supercell size is physically meaningful. At the moment, there are some disadvantages of the bond-valence model which limit us to simulate supercell size with $N¿42$, since the supercell would fall apart. Therefore, we could not exclude the false possibility yet. Now we are currently working on developing new generation of bond-valence model, possibly including some of the good quality from the shell-model and with good NPT quality.

8.4 Conclusion

In summary, we found the 90° domain wall width is of several lattice constants, consistent with other DFT studies, HRTEM and AFM experiments. The Merz's law seems to be able to describe the nucleation dynamics well, however, the larger simulation cell is necessary but missing for further validation of Merz's law. We hope that our prediction on nucleation rate and asymmetric domain wall structure can provide a better knowledge of 90° domain wall. In the near future, we would be able to perform a better and complete investigation with improved parameter sets for bond-valence model.

Chapter 9

Summary and Future Directions

The first three chapters of this thesis illustrate how we use the first-principles DFT calculations to investigate the properties of bulk perovskite ferroelectric materials. Since the chemical bonding fundamentally determines both the geometry and the properties of a material, we approach our problems by understanding the chemical bonding first.

In Chapter 4, we saw chemical bonding as a combination of different interactions. And what we found is that the Coulomb force becomes less important when it comes to extremely tetragonal polar systems. We have found the total energy is contributed from electrostatic interactions, strain-polarization coupling, short-range repulsion and maybe bond-valence energy. It would be neat to derive the contribution quantitatively, and see whether this energy model is transferable to other similar highly tetragonal polar oxides.

In Chapter 5, large coupling between strain and polarization leads to large coupling energy difference between structures with different cation orderings, making the structure energetics sensitive to the cation arrangement. By identifying a strong correlation between strain and the B-cation displacement for a large number of Pb-based and Bi-based tetragonal solid solutions, we derive guidelines for searching solid solution end-members with high-T_c morphotropic phase boundary. For the moment, this knowledge has not been expanded covering solid solutions with magnetic ions. The strong magnetic and electric coupling would add complexity. However, it would

be interesting and necessary to develop a similar roadmap for the multiferroic solid solutions.

In Chapter 6, we analyzed the atomic orbital components of the electronic band structure for highly polar perovskite oxides, we are able to engineer the band gap and carrier mobilities. The effective mass is one of the most important parameters in photovoltaic applications. It's determined by the curvature of valence band maximum and conduction band minimum. The bigger curvature of the electronic bands, the easier charge carrier transport. However, so far it places challenges for the experimentalists to grow crystals for a particular cation arrangement, even layer by layer B-cations. The conventional annealing method will lead to a complex compounds with all possible cation arrangements, since the energy difference from one cation ordering to the other is very small. For the future directions, searching for a material that automatically solves the above problems would make it one step closer to the actual photovoltaic application. Plus, we found the possibility of building a multijunction solar cell using single-component material. The polarization direction can be switched by 90° via external electrical field, accompanied with structural relaxation. We have proved that for layered B-cation arrangement of BZT, the band gap can be tuned by as significant as 0.6 eV in this way. However, it has not been demonstrated in a dynamic process. This topic can be very interesting and promising as a future research direction.

The last two chapters of this thesis are related to the molecular dynamics study using an accurate and transferrable classical interatomic potential— the bond-valence model. This model relates the strength of a bond between two ions to the distance between them, which enables us to perform much larger scale of atomistic simulations for perovskite materials with a high level of accuracy that is comparable to DFT calculations.

In Chapter 7, by applying an external electric field on $PbTiO_3$, we track the atomic scale response which depends on temperature, E field pulse shape, magnitude and pulse-pulse time separation. We learned how to achieve the ferroelectric domain flipping coherently in an optimal way. This idea has interested many research groups, among which Lindenberg group from Stanford University have shown special interests and have been actively working on this matter. The future plan is to closely work with experimental group and help them to realize this dynamic process in the lab. Recently, they have found that they were able to use optical pulses to make the polarization fluctuate. As the charge carriers are generated by materials absorb optical pulses, the electrons and holes flow in the opposite directions to the surfaces. It changes the depolarization field, further changes the bulk polarization magnitude. We should be able to contribute to this aspect by using DFT. First, we should be able to model how the change of surface charge affects the bulk polarization. And then, we might be able to incorporate some of the DFT insights into MD simulation and model the

dynamics. Plus, time scale of carrier transport process can be figured out based on the calculation of intrinsic mobility.

In Chapter 8, by applying an external mechanical stress, we examine not only the static properties of the 90° domain wall but also whether the nucleation dynamics obeys the Merz's law. Although lead titanite is so far our major target to study, developing BV model for other ferroelectric perovskite materials are also feasible. The most interesting other prototypical materials for the future studies are: $BaTiO_3$, $SrTiO_3$ and $BiFeO_3$. Each of them possesses different interesting structures, ferroelectric and dielectric properties. $BaTiO_3$ might present some level of challenge for BV parameter development, because it has three different ferroelectric phases plus one paraelectric phase. Although they have been widely studied experimentally and theoretically, there are still many unsolved puzzles. Furthermore, once the robust BV model parameter sets are derived for both end-members for solid solutions, we will be able to simulate and characterize solid solutions that show properties unachievable in single-component materials. For future directions, $BiFeO_3$ is of particular interests, which is famous for its multiferroic properties.

Bibliography

[1] http://opium.sourceforge.net.

[2] M. T. Anderson and K. R. Poeppelmeier. La_2cusno_6 - a new perovskite-related compound with an unusual arrangement of b-cations. *Chem. Mater.*, 3:476–82, 1991.

[3] V. I. Anisimov, F. Aryasetiawan, and A. I. Lichtenstein. First-principles calculations of the electronic structure and spectra of strongly correlated systems: The lda+u method. *J. of Phys. Conds. Matt.*, 9:767–808, 1997.

[4] Vladimir I. Anisimov. *Strong coulomb correlations in electronic structure calculations*. Gordon and Breach Science Publishers, 2000.

[5] A. Artemev, J. Slutsker, and A. L. Roytburd. Phase field modeling of domain structures in ferroelectric thin films. *IEEE transactions of ultrasonics, ferroelectrics, and frequency control*, 5:963–70, 2008.

[6] P. Baettig, C. F. Schelle, R. LeSar, U. V. Waghmare, and A. Spaldin. Theoret-

ical prediction of new high-performance lead-free piezoelectrics. *Chem. Mater.*, 17:1376–1380, 2005.

[7] D. Bagayoko, G. L. Zhao, J. D. Fan, and J. T. Wang. ab initio calculations of the electronic structure and optical properties of ferroelectric tetragonal batio$_3$. *J. Phys.: Condens. Matter*, 10:5645–55, 1998.

[8] A. A. Belik, S. Iikibo, K. Kodama, N. Igawa, S. Shamoto, S. Niitaka, M. Azuma, Y. Shimakawa, M. Takano, F. Izumi, and E. Takayama-Muromachi. Neutron powder diffraction study on the crystal and magnetic structures of bicoo$_3$. *Chem. Mater.*, 18:798–803, 2006.

[9] A. A. Belik, S. Y. Stefanovich, B. I. Lazoryak, and E. Takayama-Muromachi. Biino$_3$: A polar oxide with gdfeo$_3$-type perovsikte structure. *Chem. Mater.*, 18:1964–8, 2006.

[10] A. A. Belik, T. Wuernisha, T. Kamiyama, K. Mori, M. Maie, T. Nagai, Y. Matsui, and E. Takayama-Muromachi. High-pressure synthesis, crystal structures, and properties of perovskite-like bialo$_3$ and pyroxene-like bigao$_3$. *Chem. Mater.*, 18:133–9, 2006.

[11] L. Bellaiche, A. Garcia, and D. Vanderbilt. Finite-temperature properties of pb(zr$_{1-x}$ti$_x$)o$_3$ alloys from first principles. *Phys. Rev. Lett.*, 84:5427–30, 2000.

[12] L. Bellaiche and D. Vanderbilt. Electrostatic model of atomic ordering in complex perovskite alloys. *Phys. Rev. Lett.*, 81:1318–21, 1998.

[13] J. Bennett, I. Grinberg, and A. M Rappe. Effect of substituting of s for o: The sulfide perovskite $bazrs_3$ investigated with density fuctional theory. *Phys. Rev. B*, 79:235115–1–6, 2009.

[14] J. W. Bennett, I. Grinberg, and A. M. Rappe. New highly polar semiconductor ferroelectrics through d cation-o vacancy substitution into $pbtio_3$: A theoretical study. *J. Amer. Chem. Soc.*, 130:17409–12, 2008.

[15] D. I. Bilc, R. Orlando, R. Shaltaf, G.-M. Rignanese, J. I niguez, and P. Ghosez. Hybrid exchange-correlation functional for accurate prediction of the electronic and structural properties of ferroelectric oxides. *Phys. Rev. B*, 77:165107–1–13, 2008.

[16] D. I. Bilc and D. J. Singh. Frustration of tilts and a-site driven ferroelectricity in $knbo_3$-$linbo_3$ alloys. *Phys. Rev. Lett.*, 96:147602–1–4, 2006.

[17] F. Bloch. *Z. Physik*, 52:555, 1928.

[18] M. Born and J. R. Oppenheimer. Quantum theory of molecules. *Ann. Phys.*, 84(4):457–484, 1927.

[19] A. M. Bratkovsky and A. P. Levanyuk. Abrupt appearance of the domain

pattern and fatigue of thin ferroelectric films. *Phys. Rev. Lett.*, 84:3177–80, 2000.

[20] T. Brixner and G. Gerber. Femtosecond polarization pulse shaping. *Opt. Lett.*, 26:557–9, 2001.

[21] I. D. Brown. The bond-valence method. In M. O'Keeffe and A. Navrotsky, editors, *Structure and Bonding in Crystals II*, pages 1–30, New York, New York, 1981. Academic Press.

[22] I. D. Brown. Recent developments in the methods and applications of the bond valence model. *Chem. Rev.*, 109:6858–6919, 2009.

[23] F. Bruneval, N. Vast, and L. Reining. Effect of self-consistency on quasiparticles in solids. *Phys. Rev. B*, 74:045102–1–15, 2006.

[24] B. P. Burton and E. Cockayne. Why pb(b,b')o_3 perovskites disorder at lower temperatures than ba(b,b')o_3 perovskites. *Phys. Rev. B Rapid Comm.*, 60:12542–5, 1999.

[25] D. M. Ceperley and B. J. Alder. Ground state of the electron gas by a stochastic method. *Phys. Rev. Lett.*, 45:566–569, 1980.

[26] J. Chen, X.R. Xing, C. Sun, P.G. Hu, R.B. Yu, X.W. Wang, and L.H. Li. Zero

thermal expansion in pbtio$_3$-based perovskites. *J. Am. Chem. Soc.*, 130:1144, 2008.

[27] L. Q. Chen. Phase-field method of phase transitions/domain structures in ferroelectric thin films: A review. *J. Am. Ceram. Soc.*, 91:1835–44, 2008.

[28] S. M. Choi, C. J. Stringer, T. R. Shrout, and C. A. Randall. Structure and property investigation of a bi-based perovskite solid solution: (1-x)bi(ni$_{1/2}$ti$_{1/2}$)o$_3$-xpbtio$_3$. *J. Appl. Phys.*, 98:034108–1–4, 2005.

[29] T. Choi, S. Lee, Y. J. Choi, V. Kiryukhin, and S. W. Cheong. Switchable ferroelectric diode and photovoltaic effect in bifeo3. *Science*, 324:63–6, 2009.

[30] M. Cococcioni and S. de Gironcoli. Linear response approach to the calculation of the effective interaction parameters in the lda+u method. *Phys. Rev. B*, 71:035105, 2005.

[31] R. E. Cohen. Origin of ferroelectricity in perovskite oxides. *Nature*, 358:136–138, 1992.

[32] D. Damjanovic. Ferroelectric, dielectric and piezoelectric properties of ferroelectric thin films and ceramics. *Rep. Prog. Phys.*, 61:1267–1324, 1998.

[33] A. F. Devonshire. Theory of barium titanate .1. *Philosoph. Mag.*, 40:1040–63, 1949.

[34] S. L. Dudarev, G. A. Botton, S. Y. Savrasov, Z. Szotek, W. M. Temmerman, and A. P. Sutton. Electronic structure and elastic properties of strongly correlated metal oxides from first principles: Lsda+u, sic-lsda and eels study of uo2 and nio. *Phys. Status Solidi*, 166:429–43, 1998.

[35] R. E. Eitel, C. A. Randall, T. R. Shrout, P. W. Rehrig, W. Hackenberger, and S.-E. Park. New high temperature morphotropic phase boundary piezoelectrics based on bi(me)o_3-pbtio$_3$ ceramics. *Jpn. J. Appl. Phys.*, 40(10):5999–6002, 2001.

[36] R. E. Eitel, S. J. Zhang, T. R. Shrout, C. A. Randall, and I. Levin. Phase diagram of the perovskite system (1–x)bisco$_3$-xpbtio$_3$. *J. Appl. Phys.*, 96:2828–2831, 2004.

[37] H. W. Eng, P. W. Barnes, B. M. Auer, and P. M. Woodward. Investigation of the electronic structure of d^0 transition metal oxides belonging to the perovskite family. *Journal of Solid State Chemistry*, 175:94–109, 2003.

[38] L. M. Eng. Nanoscale domain engineering and characterization of ferroelectric domains. *Nanotechnology*, 10:405–11, 1999.

[39] S. Fahy and R. Merlin. Reversal of ferroelectric domains by ultrashort optical pulses. *Phys. Rev. Lett.*, 22:1122–25, 1994.

[40] C. M. Foster, Z. Li, M. Grimsditch, S.-K. Chan, and D. J. Lam. Anharmonicity of the lowest-frequency a_1(to) phonon in $pbtio_3$. *Phys. Rev. B*, 48:10160–7, 1993.

[41] D. Frenkel and B. Smit. Understanding molecular simulation. pages 1–148, London, UK, 1996. Academic Press.

[42] V. M. Fridkin. Bulk photovoltaic effect in noncentrosymmetric crystals. *Crystallog. Rep.*, 46:654–8, 2001.

[43] S. Fukao, J. P. McClure, A. Ito, T. Sato, I. Kimura, T. Tsuda, and S. Kato. 1st vhf radar observation of midlatitude f-region field-aligned irregularities. *Geophys. Res. Lett.*, 15:768–71, 1988.

[44] Y. Gai, J. Li, S.-S. Li, J.-B. Xia, and S.-H. Wei. Design of narrow-gap tio_2: A passivated codoping approach for enhanced photoelectrochemical activity. *Phys. Rev. Lett.*, 102:036402–1–4, 2009.

[45] V. M. Goldschmidt. Die gesetzte der krystallochemie. *Die Naturwissenschaften*, 21:477–85, 1926.

[46] X. Gonze, J.-M. Beuken, R. Caracas, F. Detraux, M. Fuchs, G.-M. Rignanese, L. Sindic, M. Verstraete, G. Zerah, F. Jollet, M. Torrent, A. Roy, M. Mikami, Ph. Ghosez., J.-Y. Raty, and D.C. Allan. First-principles computation of ma-

terial properties: the abinit software project. *Comp. Mater. Sci.*, 25:478–92, 2002.

[47] A. Grigoriev, D. H. Do, D. M. Kim, C. B. Eom, B. Adams, E. M. Dufresne, and P. G. Evans. Nanosecond domain wall dynamics in ferroelectric pb(zr,ti)o_3 thin films. *PHYSICAL REVIEW LETTERS*, 96(18):187601, 2006.

[48] I. Grinberg, V. R. Cooper, and A. M. Rappe. Relationship between local structure and phase transitions of a disordered solid solution. *Nature*, 419:909–11, 2002.

[49] I. Grinberg, V. R. Cooper, and A. M. Rappe. Oxide chemistry and local structure of pbzr$_x$ti$_{1-x}o_3$ studied by density-functional theory supercell calculations. *Phys. Rev. B*, 69:144118–1–17, 2004.

[50] I. Grinberg and A. M. Rappe. Local structure and macroscopic properties in pbmg$_{1/3}$nb$_{2/3}o_3$–pbtio$_3$ and pbzn$_{1/3}$nb$_{2/3}o_3$–pbtio$_3$ solid solutions. *Phys. Rev. B*, 70(22):220101–1–4, 2004.

[51] I. Grinberg and A. M. Rappe. Nonmonotonic t_c trends in bi-based ferroelectric perovskite solid solutions. *Phys. Rev. Lett.*, 98:037603–1–4, 2007.

[52] I. Grinberg, M. R. Suchomel, P. K. Davies, and A. M. Rappe. Predicting morphotropic phase boundary locations and transition temperatures in pb- and bi-

based perovskite solid solutions from crystal chemical data and first-principles calculations. *J. Appl. Phys.*, 98:094111–1–10, 2005.

[53] I. Grinberg, M. R. Suchomel, W. Dmowski, S. E. Mason, H. Wu, P. K. Davies, and A. M. Rappe. Structure and polarization in the high t_c ferroelectric bi (zn, ti) o_3-pbtio_3 solid solutions. *Phys. Rev. Lett.*, 98:107601–1–4, 2007.

[54] S. V. Halilov, M. Fornari, and D. J. Singh. Lattice instabilities in (pb,cd)tio_3 alloys. *Appl. Phys. Lett.*, 81:3443–5, 2002.

[55] D. R. Hamann, M. Schlüter, and C. Chiang. Norm-conserving pseudopotentials. *Phys. Rev. Lett.*, 43:1494–7, 1979.

[56] J. Hebling, K.-L. Yeh, K. A. Nelson, and M. C. Hoffmann. High power thz generation, thz nonlinear optics, and thz nonlinear spectroscopy. In *IEEE J. Selected Topics in Quantum Electronics*, pages 345–53, 2008.

[57] J. Hlinka. Mobility of ferroelastic domain walls in barium titanate. *Ferroelectrics*, 349:49–54, 2007.

[58] J. Hlinka and P. Marton. Phenomenological model of 90° domain wall in $batio_3$-type ferroelectrics. *Phys. Rev. B*, 74:104104–1–12, 2006.

[59] P. Hohenberg and W. Kohn. Inhomogeneous electron gas. *Phys. Rev.*, 136:B864–71, 1964.

[60] P.H. Hu, J. Chen, J.X. Deng, and X.R. Xing. Thermal expansion, ferroelectric and magnetic properties in (1-x)pbtio$_3$-$x$bi(ni$_{1/2}$ti$_{1/2}$)o$_3$. *J. Am. Chem. Soc.*, 132:1925–8, 2010.

[61] H. Hughes, M. M. B. Allix, C. A. Bridges, J. B. Claridge, X. Kuang, H. Niu, S. Taylor, W. Song, and M. J. Rosseinsky. A polar oxide with a large magnetization synthesized at ambient pressure. *J. Am. Chem. Soc.*, 127:13790–1, 2005.

[62] S.C. Hwang and G. Arlt. Switching in ferroelectric polycrystals. *J. Appl. Phys.*, 87:869–75, 2000.

[63] M. S. Hybertsen and Steven G. Louie. First-principles theory of quasiparticles: calculation of band gaps in semiconductors and insulators. *Phys. Rev. Lett.*, 55:1418–1421, 1985.

[64] Y. Inoue, K. Sato, K. Sato, and H. Miyama. Photoassisted water decomposition by ferroelectric lead zirconate titanate ceramics with anomalous photovoltaic effects. *J. Phys. Chem.*, 90:2809–10, 1986.

[65] S. Ishiwata, M. Azuma, M. Takano, E. Nishibori, M. Takata, M. Sakata, and K. Kato. High pressure synthesis, crystal structure and physical properties of a new ni(ii) provskite binio$_3$. *J. Mater. Chem.*, 12:3733–7, 2002.

[66] S. G. Johnson and J. D. Joannopoulos. Block-iterative frequency-domain methods for maxwell's equations in a planewave basis. *Optics Express*, 8:173–190, 2001.

[67] S. Ju and G. Y. Guo. First-principle study of crystal structure, electronic structure, and second-harmonic generation in a polar double perovskite bi_2zntio_6. *J. Chem. Phys.*, 129:194704–1–9, 2008.

[68] P. Juhás, I. Grinberg, A. M. Rappe, W. Dmowski, T. Egami, and P. K. Davies. Correlations between the structure and dielectric properties of $pb(sc_{2/3}w_{1/3})o_3$–$pb(ti/zr)o_3$ relaxors. *Phys. Rev. B*, 69:214101–1–13, 2004.

[69] S. V. Kalinin, C. Y. Johnson, and D. A. Bonnell. Domain polarity and temperature induced potential inversion on the $batio_3$ (100) surface. *J. Appl. Phys.*, 91:3816–23, 2002.

[70] Dmitry D. Khalyavin, Andrei N. Salak, Nikolai P. Vyshatko, Augusto B. Lopes, Nikolai M. Olekhnovich, Anatoly V. Pushkarev, Ivan I. Maroz, and Yury V. Radyush. Crystal structure of metastable perovskite $bi(mg_{1/2}ti_{1/2})o_3$: Bi-based structural analogue of antiferroelectric $pbzro_3$. *Chem. Mater.*, 18:5104–10, 2006.

[71] R. D. King-Smith and D. Vanderbilt. Theory of polarization of crystalline solids. *Phys. Rev. B*, 47:1651–4, 1993.

[72] L. Kleinman and D. M. Bylander. Efficacious form for model pseudopotentials. *Phys. Rev. Lett.*, 48:1425–8, 1982.

[73] W. Kohn and L. J. Sham. Self-consistent equations including exchange and correlation effects. *Phys. Rev.*, 140:A1133–8, 1965.

[74] Alexie M. Kolpak, Dongbo Li, Rui Shao, Andrew M. Rappe, and Dawn A. Bonnell. Evolution of the structure and thermodynamic stability of the batio$_3$ (001) surface. *Phys. Rev. Lett.*, 101:036102–1–4, 2008.

[75] A. Kudo and Y. Miseki. Heterogeneous photocatalyst materials for water splitting. *Chem. Soc. Rev.*, 38:253–78, 2008.

[76] M. M. Kumar, V. R. Palkar, K. Srinivas, and S. V. Suryanarayana. Ferroelectricity in a pure bifeo$_3$ ceramic. *Appl. Phys. Lett.*, 76:2764–6, 2000.

[77] B. K. Lai, I. Ponomareva, I. A. Kornev, L. Bellaiche, and G. J. Salamo. Domain evolution of batio$_3$ ultrathin films under an electric field: A first-priciples study. *Phys. Rev. B*, 75:085412–1–7, 2007.

[78] B. K. Lai, I. Ponomareva, I. I. Naumov, I. A. Kornev, H. Fu, L. Bellaiche, and G. J. Salamo. Electric-field-induced domain evolution in ferroelectric ultrathin films. *Phys. Rev. Lett.*, 96:137602–1–4, 2006.

[79] S. Lebegue, B. Arnaud, B. Alouani, and P. E. Bloechl. Implemetation of an

all-electron gw approximation based on the projector augmented wave method without plasmon pole approximation: Application to si, sic, alas, inas, nah, and kh. *Phys. Rev. B*, 67:155208–155208–10, 2003.

[80] R. J. Levis and H. A. Rabitz. Closing the loop on bond selective chemistry using tailored strong field laser pulses. *J. Phys. Chem.*, 106:6427–44, 2002.

[81] J. Y. Li, R. C. Rogan, E. Ustundag, and K. Bhattacharya. Domain switching in polycrystalline ferroelectric ceramics. *Nature Materials*, 4:776–781, 2005.

[82] S. J. Lindsay. Lindsay, s j (lind-individual). In U. S. P. Office, editor, *Derwent Innovations Index*, US, 2004.

[83] M. P. McCormick and J. C. Larsen. Antarctic measurements of ozone by sage-ii in the spring of 1985, 1986, and 1987. *Feophys. Res. Lett.*, 15:907–10, 1988.

[84] D. A. McQuarrie. Statistical mechanics. pages 1–67, CA, USA, 2000. University Science Books.

[85] H. D. Megaw. Crystal structure of barium titanate. *Nature*, 155:484–5, 1945.

[86] B. Meyer and D. Vanderbilt. *Ab Initio* study of ferroelectric domain walls in $pbtio_3$. *Phys. Rev. B*, 65:104111 1–11, 2002.

[87] H. J. Monkhorst and J. D. Pack. Special points for brillouin-zone integrations. *Phys. Rev. B*, 13:5188–5192, 1976.

[88] A. Moure, M. Algueró, L. Pardo, E. Ringgaard, and A. Pedersen. Microstructure and temperature dependence of properties of morphotropic phase boundary bi($mg_{1/2}ti_{1/2}$)o_3-pbtio$_3$ piezoceramics processed by conventional routes. *J. Eur. Ceram. Soc.*, 27:237–45, 1997.

[89] A. M. Nazmul, S. Sugahara, and M. Tanaka. Ferromagnetism and high curie temperature in semiconductor heterostructures with mn delta-doped gaas and p-type selective doping. *Phys. Rev. B*, 67:241308, 2003.

[90] K. A. Nelson. *Coherent control: Optics, molecules, and materials.* Springer-Verlag, Berlin, 1995.

[91] Patrick Nuernberger, Gerhard Vogt, Tobias Brixner, and Gustav Gerber. Femtosecond quantum control of molecular dynamics in the condensed phase. *Phys. Chem. Chem. Phys.*, 9:2470–97, 2007.

[92] J. Padilla, W. Zhong, and David Vanderbilt. First-principles investigation of 180° domain walls in batio$_3$. *Phys. Rev. B*, 53:R5969–73, 1996.

[93] M. C. Payne, M. P. Teter, D. C. Allan, T. A. Arias, and J. D. Joannopoulos. Iterative minimization techniques for *ab initio* total-energy calculations: Molecular dynamics and conjugate gradients. *Rev. Mod. Phys.*, 64:1045–97, 1992.

[94] J. P. Perdew, K. Burke, and M. Ernzerhof. Generalized gradient approximation made simple. *Phys. Rev. Lett.*, 77:3865–8, 1996.

[95] J. P. Perdew and Y. Wang. Accurate and simple analytic representation of the electron-gas correlation energy. *Phys. Rev. B*, 45:13244–9, 1992.

[96] J. P. Perdew and A. Zunger. Self-interaction correction to density-functional approximations for many-electron systems. *Phys. Rev. B*, 23:5048–79, 1981.

[97] M. Peressi, N. Binggeli, and A. Baldereschi. Band engineering at interfaces: theory and numerical experiments. *J. Phys. D - Appl. Phys.*, 31:1273–99, 1998.

[98] S. R. Phillpot and V. Gopalan. Coupled displacive and order-disorder dynamics in linbo$_3$ by molecular-dynamics simulation. *Appl. Phys. Lett.*, 84:1916–8, 2004.

[99] S. Pöykkö and D. J. Chadi. *Ab initio* study of 180° domain wall energy and structure in pbtio$_3$. $Chem.Phys.Lett., 75 : 2830 - -2, 1999.$

[100] T. Qi, I. Grinberg, and A. M. Rappe. First-principles investigation of a highly tetragonal ferroelectric material: Bi(zn$_{1/2}$ti$_{1/2}$)o$_3$. *Phys. Rev. B*, 79:094114–1–5, 2009.

[101] T. Qi, I. Grinberg, and A. M. Rappe. Correlations between tetragonality, polarization, and ionic displacement in pbtio$_3$-derived ferroelectric perovskite solid solutions. *Phys. Rev. B*, 82:134113–1–5, 2010.

[102] T. Qi, Y. H. Shin, K. L. Yeh, K. A. Nelson, and A. M. Rappe. Collective coherent control: Synchronization of polarization in ferroelectric pbtio$_3$ by shaped thz fields. *Phys. Rev. Lett.*, 102:247603 1–4, 2009.

[103] N. J. Ramer and A. M. Rappe. Designed nonlocal pseudopotentials for enhanced transferability. *Phys. Rev. B*, 59:12471–8, 1999.

[104] C. A. Randall, R. Eitel, B. Jones, T. R. Shrout, D. I. Woodward, and I. M. Reaney. Investigation of a high T_c piezoelectric system: (1-$x$bi(mg$_{1/2}$ti$_{1/2}$)o$_3$–(x)pbtio$_3$. *J. Appl. Phys.*, 95:3633–9, 2004.

[105] A. M. Rappe, K. M. Rabe, E. Kaxiras, and J. D. Joannopoulos. Optimized pseudopotentials. *Phys. Rev. B Rapid Comm.*, 41:1227–30, 1990.

[106] Y. Saito, H. Takao, T. Tani, T. Nonoyama, K. Takatori, T. Homma, T. Nagaya, and M. Nakamura. Lead-free piezoceramics. *Nature*, 432:84–7, 2004.

[107] S. Shi and H. Rabitz. Selective excitation in harmonic molecular-systems by optimally designed fields. *Chem. Phys.*, 139:185–99, 1989.

[108] D. Shilo, G. Ravichandran, and K. Bhattacharya. Investigation of twin-wall structure at the nanometre scale using atomic force microscopy. *Nature Materials*, 3:453–7, 2004.

[109] T. Shimada, Y. Umeno, and T. Kitamura. Ab initio study of stress-induced domain switching in pbtio$_3$. *Phys. Rev. B*, 77:094105–1–7, 2008.

[110] T. Shimada, K. Wakahara, Y. Umeno, and T. Kitamura. Shell model potential for pbtio$_3$ and its applicability to surfaces and domain walls. *J. Phys. Cond. Matt.*, 20:325225–1–10, 2008.

[111] Y.-H. Shin, V. R. Cooper, I. Grinberg, and A. M. Rappe. Development of a bond-valence molecular-dynamics model for complex oxides. *Phys. Rev. B*, 71(5):054104–1–4, 2005.

[112] Y.-H. Shin, I. Grinberg, I.-W. Chen, and A. M. Rappe. Nucleation and growth mechanism of ferroelectric domain-wall motion. *Nature*, 449:881–884, 2007.

[113] Y.-H. Shin, J.-Y. Son, B.-J Lee, I. Grinberg, and A. M. Rappe. Order-disorder character of pbtio3. *Condens. Matter*, 20:015224–1–5, 2008.

[114] D. J. Singh. Structure and energetics of antiferroelectric pbzro$_3$. *Phys. Rev. B*, 52:12559–63, 1995.

[115] D. M. Stein, M. R. Suchomel, and P. K. Davies. Enhanced tetragonality in (x)pbtio$_3$-(1-x)bi(b'b")o$_3$ systems: Bi(zn$_{3/4}$w$_{1/4}$)o$_3$. *Appl. Phys. Lett.*, 89:132907–1–3, 2006.

[116] S. Stemmer, S. K. Streiffer, and M. Rühle. Atomistic structure of 90^0 domain walls in ferroelectric pbtio$_3$ thin films. *Philosophical Magazine A*, 71:713–24, 1995.

[117] M. R. Suchomel and P. K. Davies. Predicting the position of the morphotropic phase boundary in high temperature pbtio3-bi((bb')-b-')o-3 based dielectric ceramics. *J. Appl. Phys.*, 96:4405–4410, 2004.

[118] M. R. Suchomel and P. K. Davies. Enhanced tetragonality in (x)pbtio3-(1-x)bi(zn1/2ti1/2)o-3 and related solid solution systems. *Appl. Phys. Lett.*, 86:262905, 2005.

[119] M. R. Suchomel, A. M. Fogg, M. Allix, H. Niu, J. B. Claridge, and M. J. Rosseinsky. Additions and corrections to "bi_2zntio_6: A lead-free close-shell polar perovskite with a calculated ionic polarization of 150μc cm^{-2}". *Chem. Matter.*, 18:5810, 2006.

[120] M. R. Suchomel, A. M. Fogg, M. Allix, H. Niu, J. B. Claridge, and M. J. Rosseinsky. Bi_2zntio_6: A lead-free close-shell polar perovskite with a calculated ionic polarization of 150μc cm^{-2}. *Chem. Matter.*, 18:4987, 2006.

[121] P. V. Sushko, A. L. Shluger, and C. R. A. Catlow. Relative energies of surface and defect states: ab initio calculations for the mgo(001) surface. *Surf. Sci.*, 450:153–70, 2000.

[122] S. Tinte, K. M. Rabe, and D. Vanderbilt. Anomalous enhancement of tetragonality in $pbtio_3$ induced by negative pressure. *Phys. Rev. B*, 68:144105–1–9, 2003.

[123] T. Tybell, C. H. Ahn, and J.-M. Triscone. Ferroelectricity in thin perovskite films. *Appl. Phys. Lett.*, 75:856–8, 1999.

[124] T. Tybell, P. Paruch, T. Giamarchi, and J.-M. Triscone. Domain wall creep in epitaxial ferroelectric pb(zr_0.2ti_0.8)o_3 thin films. *Phys. Rev. Lett.*, 89:097601–1–4, 2002.

[125] K. K. Uprety, L. E. Ocola, and O. Auciello. Growth and characterization of transparent pb(zi,ti)o-3 capacitor on glass substrate. *J. Appl. Phys.*, 102:084107, 2007.

[126] D. Vanderbilt and R. D. King-Smith. Electric polarization as a bulk quantity and its relation to surface charge. *Phys. Rev. B*, 48:4442, 1993.

[127] M. M. Wefers and K. A. Nelson. Generation of high-fidelity programmable ultrafast optical wave-forms. *Opt. Lett.*, 20:1047–9, 1995.

[128] S.H. Wei and A. Zunger. Calculated natural band offsets of all ii-vi and ill-v semiconductors: Chemical trends and the role of cation d orbitals. *Appl. Phys. Lett.*, 72:2011–3, 1998.

[129] A. M. Weiner. Femtosecond pulse shaping using spatial light modulators. *Rev. Sci. Instrum.*, 71:1929–60, 2000.

[130] M. H. Whangbo and R. Hoffmann. The band structure of the tetracyanoplatinate chain. *J. Amer. Chem. Soc.*, 100:6093–8, 1978.

[131] Z. Wu, R. E. Cohen, and D. J. Singh. Comparing the weighted density approximation with the lda and gga for ground-state properties of ferroelectric perovskites. *Phys. Rev. B*, 70:104112–7, 2004.

[132] Z. G. Wu and H. Krakauer. Charge-transfer electrostatic model of compositional order in perovskite alloys. *Phys. Rev. B*, 63:184113 1–8, 2001.

[133] Y.H. Xie, E. A. Fitzgerald, P. J. Silverman, F. A. Thiel, and G. P. Watson. Very high-mobility 2-dimensional hole gas in si/ge$_x$si$_{1-x}$/ge structures grown by molecular-beam epitaxy. *Appl. Phys. Lett.*, 63:2263–4, 1993.

[134] Y. X. Yan, E. B. Gamble, and K. A. Nelson. Impulsive stimulated scattering - general importance in femtosecond laser-pulse interactions with matter, and spectroscopic applications. *J. Chem. Phys.*, 83:5391–9, 1985.

[135] S. Y. Yang, J. Seidel, S. J. Byrnes, P. Shafer, C. H. Yang, M. D. Rossell, P. Yu, Y. H. Chu, J. F. Scott, J. W. Ager, L. W. Martin, and R. Ramesh. Above-bandgap voltages from ferroelectric photovoltaic devices. *Nature Nonotechnology*, 5:143–7, 20110.

[136] J. X. Zhang, R. Wu, S. Choudhury, Y. L. Li, S. Y. Hu, and L. Q. Chen. Three-dimensional phase-field simulation of domain structures in ferroelectric islands. *Appl. phys. Lett.*, 92:122906–1–3, 2008.

[137] Q. Zhang and W. A. Goddard III. Charge and polarization distribution at the 90^0 domain wall in barium titanate ferroelectric. *Appl. Phys. Lett.*, 89:182903–1–3, 2006.

[138] S. J. Zhang, C. J. Stringer, R. Xia, S. M. Choi, C. A. Randall, and T. R. Shrout. Investigation of bismuth-based perovskite system: (1-x)bi(ni$_{1/2}$nb$_{1/2}$)o$_3$-xpbtio$_3$. *J. Appl. Phys.*, 98:034103–1–5, 2005.

[139] W. Zhong, D. Vanderbilt, and K. M. Rabe. First-principles theory of ferreoelectric phase transitions for perovskites: The case of batio$_3$. $Phys.Rev.B, 52 : 6301 - -12, 1995.$